博士論文

Numerical Study of the Dephasing Effect on a Perfectly Conducting Channel in Graphene Nanoribbons with Zigzag Edges

ジグザグ端グラフェン・ナノリボンの
完全伝導チャネルに対する
位相緩和効果に関する数値的研究

下 村 祐 司

広島大学大学院先端物質科学研究科

2016 年 3 月

目次

１．主論文

　　　Numerical Study of the Dephasing Effect on a Perfectly Conducting Channel in Graphene Nanoribbons with Zigzag Edges
　　　（ジグザグ端グラフェン・ナノリボンの完全伝導チャネルに対する位相緩和効果に関する数値的研究）
　　　　　下村　祐司

２．公表論文

３．参考論文

主論文

Numerical Study of the Dephasing Effect on a Perfectly Conducting Channel in Graphene Nanoribbons with Zigzag Edges

ジグザグ端グラフェン・ナノリボンの完全伝導チャネルに対する位相緩和効果に関する数値的研究

下村　祐司

Contents

Chapter 1

Introduction

1.1 From Graphene to Graphene Nanoribbon

From the discovery of fullerene (1985),[1] carbon nanotube (1991),[2] and graphene (2004),[3] many researchers have extensively studied the physical properties of such nanocarbon materials and revealed their interesting characters. Fullerenes are a large class of carbon molecules having a hollow closed structure. A well-known example is Buckminsterfulerene C_{60}, named after Richard Buckminster Fuller. Its structure resembles a soccer ball consisting of twenty hexagons and twelve pentagons. Cylindrical fullerenes are called carbon nanotubes (CNTs). A single-walled CNT is equivalent to a honeycomb lattice of carbon atoms rolled up into a cylinder. Carbon atoms arranged into a planar honeycomb lattice is called graphene, which is just equivalent to a monolayer of graphite with only one atom thick. It had been believed that the structure of this ultrathin material is unstable in a free standing state because of its ideal thickness. In 2004, Novoselov and Geim, however, succeeded to separate monolayer graphene in an ideal manner from highly-oriented pyrolytic graphite (HOPG). Their achievement leads to rapid advances in fundamental physics and practical applications of graphene with a dramatic impact on nanomaterials research. They were awarded Nobel prize in physics in 2010. This marvelous achievement was performed in an astonishingly simple way.[3,4] They separated graphite flakes from HOPG using a scotch tape, and put them onto the surface of a SiO_2 wafer. They carefully observed the wafer using an atomic force microscope, and found a monolayer graphene among a variety of multilayer graphenes. That is, graphene can be exfoliated from graphite. No one notices this simple fact before the pioneering work of Novoselov and Geim. It is just equivalent to what happens when we draw with a pencil on paper.

The discovery of monolayer graphene stimulated extensive studies on its unusual electronic properties arising from the two-dimensional honeycomb structure of carbon atoms.[5] A typical example is the half-integer quantum Hall effect.[3,6] Since the unit cell of the honeycomb lattice contains two nonequivalent sites, A and B, forming A and B sublattices (see Fig. 1.1), an effective mass equation for electrons in graphene becomes a 2×2 matrix form, which is equivalent to the massless Dirac equation.[5] Thus, electrons in graphene are called massless Dirac fermions. The band structure of massless Dirac fermions has a unique character since they have linear energy dispersion in the vicinity of two nonequivalent symmetry points, called K_+ and K_- points, in the Brillouin zone, where the conduction and valence bands

conically touch. This structure is called Dirac cone (see Fig. 1.1). We hereafter set the electron energy at the band touching point as $E = 0$. Because the density of states vanishes at $E = 0$, graphene is often called a zero-gap semiconductor although it is metallic even near the band touching point.
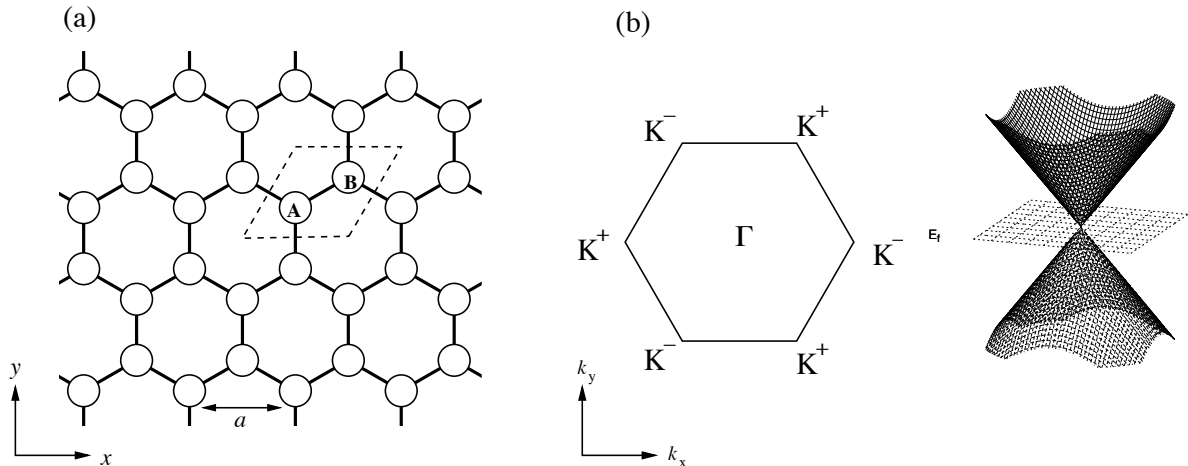

Figure 1.1: (a)The structure of graphene, where a rhombus indicates the unit cell containing nonequivalent A and B sites. (b)The first Brillouin zone (left figure) and the band structure (right figure) of graphene. K_- and K_+ indicate the symmetry points, at which the conduction and valence bands conically touch.

The presence of edges gives an strong impact on Dirac fermions in graphene near the Fermi energy. As stressed by Fujita and co-workers,[7] the electronic states in graphene strongly depends on its edge structure. Typical straight edges of graphene are classified into two structures: one is zigzag edge and the other is armchair edge (see Fig. 1.2). Fujita and co-workers analyzed electronic states in graphene with an infinitely long straight edge using a nearest-neighbor tight-binding model, and showed that highly degenerate edge localized states appear at $E = 0$ along a zigzag edge. These states at $E = 0$ result in a sharp zero-energy peak structure in the local density of states near a straight zigzag edge. No such localized states appear along an armchair edge. The presence of edge localized states along a zigzag edge has been confirmed by scanning tunneling microscopy and scanning tunneling spectroscopy observations.[8,9]

Edge localized states should affect various physical properties of a monolayer graphene with zigzag edges owing to a sharp zero-energy peak structure. We naturally expect that such an effect becomes notable with decreasing the system size. A prototypical system to observe the effect of edge localized states is a ribbon shaped nano wire of graphene with zigzag edges (see Fig. 1.3), which is referred to as a zigzag nanoribbon hereafter. It has been demonstrated that the orbital diamagnetism in a zigzag nanoribbon shows an anomalous behavior reflecting a zero-energy peak structure.[10] Electron transport in a zigzag nanoribbon also shows an anomalous behavior owing to the presence of edge localized states.[11,12]
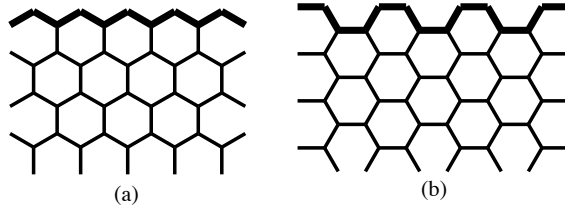
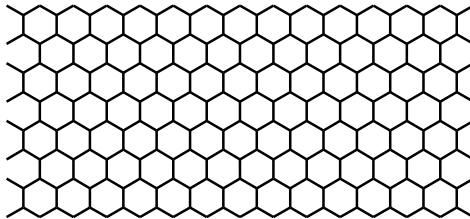Figure 1.2: Typical straight edges of graphene: (a) zigzag edge and (b) armchair edge.

Figure 1.3: Illustration of a zigzag nanoribbon.

1.2 Perfectly Conducting Channel

As is mentioned below, disordered zigzag nanoribbons accommodate a perfectly conducting channel (PCC) reflecting the unique band structure with partially flat subbands related to the edge localized states. This thesis focuses on a PCC in zigzag nanoribbons. The PCC designates a conducting channel that perfectly transmits an electron from one end to the other in spite of the presence of disorder, and crucially affects electron transport in the system. The most well-known example is a one-dimensional (1D) chiral edge channel of two-dimensional (2D) quantum Hall insulators.[13] This 1D edge channel needs a strong magnetic field for its stabilization. So far, PCCs have been shown to appear in various carbon nanostructures and topological insulators under no external field.

Ando and co-workers[14–18] showed that a PCC appears in disordered CNTs with a gapless spectrum in the absence of intervalley scattering. The requirement of no intervalley scattering is explained as follows. A CNT possesses two energy valleys in the reciprocal space, and the effective Hamiltonian describing each valley is invariant under a time-reversal operation $\mathcal{T}$ that satisfies $\mathcal{T}^2 = -1$; the subsystems corresponding to each valley have the symplectic symmetry. Furthermore, the number of conducting channels in each valley is always odd regardless of the Fermi level. The existence of a PCC is guaranteed by the symplectic symmetry combined with an odd number of conducting channels. If intervalley scattering occurs and the two valleys are coupled as its consequence, these two conditions break down and hence the PCC destabilized. In CNTs, an impurity potential with a range larger than the lattice constant induces only very weak intervalley scattering since the two energy valleys are well separated in the reciprocal space. Thus, we expect that the above two conditions are approximately satisfied if a CNT contains only such long-range impurities (LRIs), leading to the appearance of a PCC. Clearly, there is no PCC in the presence of short-range impurities (SRIs). In actual situations, charged impurities are regarded as the LRI, while lattice defects

play the role of the SRI.

A 1D helical edge channel of 2D quantum spin-Hall insulators[19–24] can be regarded as a typical example of a PCC in topological insulators. Its protection mechanism against disorder is essentially equivalent to that of a PCC in CNTs. However, as quantum spin-Hall insulators typically possess only a single valley, the disturbance due to intervalley scattering is irrelevant in this case. A similar PCC is stabilized in three-dimensional (3D) weak topological insulators in various situations.[25–29] In 3D strong topological insulators, a PCC can appear only when a π magnetic flux penetrates the bulk of a sample without touching surface states.[30–32]

Wakabayashi and co-workers[33–35] showed that disordered graphene nanoribbons with zigzag edges accommodate a PCC, on which our interest is focused in this thesis. As in the case of CNTs, zigzag nanoribbons possess two energy valleys in the reciprocal space. The important feature of zigzag nanoribbons is that conducting channels are imbalanced between the two propagating directions in each valley. That is, the number of conducting channels going in one direction is one greater or smaller than that going in the other direction, regardless of the Fermi level. This directly results in the stabilization of a PCC[36–38] if intervalley scattering is ignorable. Thus, we expect the appearance of a PCC in zigzag nanoribbons containing only LRIs. In contrast to the case of CNTs, the symmetry of the system plays no role in this case. It has been shown that disordered graphene nanoribbons with armchair edges also accommodate a similar PCC.[39,40]

If a PCC stably exists, the dimensionless conductance g of the system decreases to the quantized value of $g = 1$ with increasing system length L. In CNTs and graphene nanoribbons, we expect the appearance of a PCC only when the disorder of the system is long-range, as noted above. Indeed, if the spatial range of disorder is sufficiently large, the strength of intervalley scattering becomes very weak. However, in actual situations, it is impossible to completely suppress intervalley scattering. The effect of residual intervalley scattering gradually manifests itself with increasing L and eventually destabilizes a PCC. In this case, the behavior of g may not be distinguishable from that in an ordinary system with no PCC.

The effect of inelastic scattering may be another important obstacle for the observation of a PCC. Inelastic scattering caused by electron–electron and/or electron–phonon interactions affects low-energy electrons mainly through energy relaxation and dephasing. At low temperatures, pure dephasing most significantly influences the transport properties. Indeed, dephasing directly destabilizes a PCC in CNTs as well as topological insulators since it weakens the underlying symplectic symmetry of the system, except for the case with only a single channel, where it becomes a PCC and is relatively robust against dephasing.[17,18] Contrastingly, a PCC in zigzag nanoribbons relies on no symmetry of the system, so dephasing does not necessarily disturb it. Previous studies[41,42] based on the Boltzmann transport equation indicate that a PCC remains even in the incoherent limit. However, it is not clear how the behavior of a PCC changes with the reduction of phase coherence.

1.3   The Orgnization of This Thesis

The purpose of this thesis is to clarify how dephasing affects a PCC in zigzag nanoribbons. In order to do this, we numerically calculate the average dimensionless conductance at zero temperature taking the dephasing effect into account. We show that dephasing does not

disturb a PCC in zigzag nanoribbons but rather relaxes its destabilization due to weak intervalley scattering.[43] This result should encourage experimental attempt to detect a PCC in zigzag nanoribbons.[44] The organization of the thesis is presented here.

In chapter 2, we present the tight-binding model for a zigzag nanoribbon. We assume that every impurity potential distributed over the system is described by a Gaussian form of spatial range d. This corresponds to an LRI (SRI) when d is larger (smaller) than the lattice constant a. We present a formulation to compute the scattering matrix for this system. Once the scattering matrix is given, the dimensionless conductance is determined by using the Landauer formula. The model for describing the pure dephasing is also introduced. In chapter 3, the numerical results of the average dimensionless conductance are presented for the case with LRIs and that with SRIs. We observe that the destabilization of the PCC can be relaxed by the dephasing in the former case. The numerical results are compared with an analytical expression for the dimensionless conductance derived from the Boltzmann transport equation.[41] We see that the numerical result in the case with strong dephasing is accurately fitted by the analytical result, implying that our model appropriately describes the effect of dephasing. The last chapter is devoted to conclusion of this thesis.

Chapter 2

Model and Formulation

2.1 Model for a Zigzag Nanoribbon

We consider a zigzag nanoribbon consisting of M zigzag lines placed along the x-axis (see Fig. 2.1). Its band structure is shown in Fig. 2.2 in the case of M = 30. One can see that in the left (right) valley, the number of right-going (left-going) channels is one greater than that of left-going (right-going) channels regardless of the location of the Fermi level. This indicates that a right-going PCC appears in the left valley while a left-going PCC appears in the right valley.[33] The details of the stabilization mechanism of a PCC is described in Appendix A.

disordered region

L
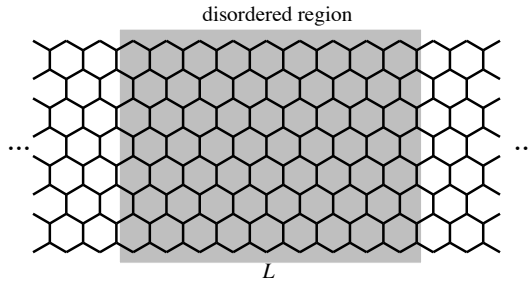
Figure 2.1: Illustration of a zigzag nanoribbon. The gray area of length L represents the disordered region with randomly distributed impurities. The left and right regions without disorder are regarded as perfect leads.

We describe π electrons in zigzag nanoribbons by using the nearest-neighbor tight-binding model

$$H = -t \sum_{n.n.} |i\rangle\langle j| + \sum_i V(\boldsymbol{r}_i)|i\rangle\langle i|, \tag{2.1}$$

where t is the hopping integral between neighboring sites, $|i\rangle$ is the π orbital on site i, and $V(\boldsymbol{r}_i)$ is the impurity potential with $\boldsymbol{r}_i$ being the position of site i. We randomly distribute impurities in a region of length L (see Fig. 2.1). We assume that each site is occupied by an impurity with probability P and the potential of each impurity is characterized by a Gaussian

Figure 2.2: Band structure of a zigzag nanoribbon with M = 30. The inset represents the magnification of subbands in the left valley.
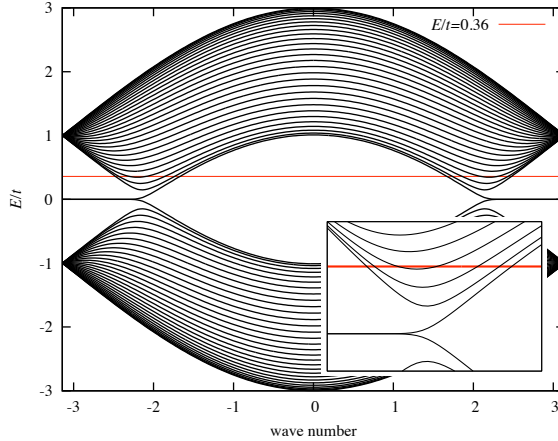
form of spatial range d. Hence, $V(\boldsymbol{r}_i)$ is represented as

$$V(\boldsymbol{r}_i) = \sum_j u(\boldsymbol{r}_j)\exp\left(-\frac{|\boldsymbol{r}_i - \boldsymbol{r}_j|^2}{d^2}\right), \tag{2.2}$$

where $u(\boldsymbol{r}_j)$ is the strength of an impurity at site j. We assume that $u(\boldsymbol{r}_j)$ is uniformly distributed within $|u| < u_{\max}/2$. Note that the degree of disorder is determined by d, P, and $u_{\max}$.

The electron transport property of a zigzag nanoribbon is determined by the scattering matrix consisting of transmission matrices $\boldsymbol{t}$ and $\boldsymbol{t}'$ and reflection matrices $\boldsymbol{r}$ and $\boldsymbol{r}'$, where $\boldsymbol{t}$ and $\boldsymbol{r}$ ($\boldsymbol{t}'$ and $\boldsymbol{r}'$) describe the scattering of an electron incoming from the left (right) as shown in Fig. 2.3. Let N_c be the number of conducting channels for a given value of the Fermi energy E. The dimensions of the transmission and reflection matrices are $N_c \times N_c$. In calculating the scattering matrix, we consider that the left and right of the disordered region serve as perfect leads of semi-infinite length without disorder. The transmission and reflection matrices can be obtained by using a recursive Green's function method. In terms of $\boldsymbol{t}$ at the Fermi level, the conductance of the system at zero temperature is given by the Landauer formula,[45]

$$G = \frac{e^2}{\pi\hbar}\text{Tr}(\boldsymbol{t}^\dagger\boldsymbol{t}). \tag{2.3}$$

We mainly consider the dimensionless conductance defined by

$$g = \text{Tr}(\boldsymbol{t}^\dagger\boldsymbol{t}), \tag{2.4}$$

instead of G. Since our attention is focused on the behavior of g at zero temperature, we hereafter treat only the scattering matrix for an electron at the Fermi level.
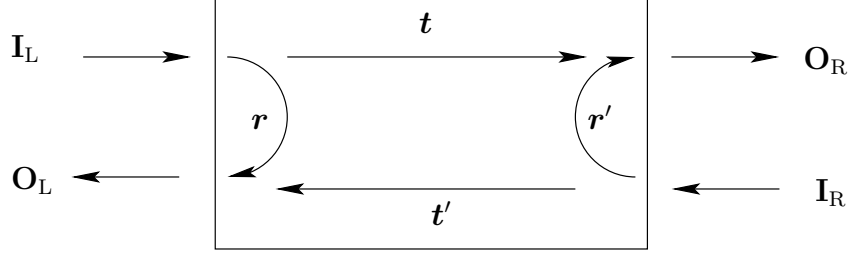
Figure 2.3: Schematic representation of the transmission and reflection matrices, where $\mathbf{I}_L$ ($\mathbf{I}_R$) denotes the amplitude of an electron incoming from the left (right) lead, and $\mathbf{O}_L$ ($\mathbf{O}_R$) denotes the amplitude of an electron outgoing to the left (right) lead.

2.2 Formulation to Compute the Scattering Matrix

In this section, we describe a formulation to compute $\boldsymbol{t}$, $\boldsymbol{t}'$, $\boldsymbol{r}$, and $\boldsymbol{r}'$ by using a recursive Green's function method.[11,12]

2.2.1 Derivation of basis functions

Let us consider a zigzag nanoribbon of width M. We take the unit cell of the zigzag nanoribbon as shown in Fig. 2.4. Each unit cell has 2M sites. The jth unit cell contains two sites of each zigzag line. We refer to a set of the left (right) sites as α (β) column. We define

$$\mathbf{C}_j^\alpha \equiv \begin{pmatrix} C_{j,1}^\alpha \\ C_{j,2}^\alpha \\ C_{j,3}^\alpha \\ \vdots \\ C_{j,M}^\alpha \end{pmatrix} \tag{2.5}$$

and

$$\mathbf{C}_j^\beta \equiv \begin{pmatrix} C_{j,1}^\beta \\ C_{j,2}^\beta \\ C_{j,3}^\beta \\ \vdots \\ C_{j,M}^\beta \end{pmatrix} \tag{2.6}$$

as the column vectors, where $C_{j,1}^\alpha$, $C_{j,2}^\alpha$, ... and $C_{j,1}^\beta$, $C_{j,2}^\beta$, ... are the amplitudes of a wave function at the corresponding sites in the jth unit cell. These column vectors obey the equations of motion:

$$\begin{aligned}
(E\mathbf{I} - \mathbf{H}^\alpha)\mathbf{C}_j^\alpha - \mathbf{V}\mathbf{C}_{j-1}^\beta - \mathbf{V}\mathbf{C}_j^\beta &= \mathbf{0}, \\
(E\mathbf{I} - \mathbf{H}^\beta)\mathbf{C}_j^\beta - \mathbf{V}\mathbf{C}_j^\alpha - \mathbf{V}\mathbf{C}_{j+1}^\alpha &= \mathbf{0},
\end{aligned} \tag{2.7}$$

where $\mathbf{H}^\alpha$ and $\mathbf{H}^\beta$ respectively represent the Hamiltonians for the α and β columns, and $\mathbf{V}$ represents the Hamiltonian of inter-column transfer between nearest neighbor α and β columns. Eliminating the column vectors for β sites (i.e., $\mathbf{C}_j^\beta$ and $\mathbf{C}_{j-1}^\beta$) from (2.7), we obtain

$$\mathbf{C}_{j+1}^\alpha + \mathbf{v}\mathbf{C}_j^\alpha + \mathbf{C}_{j-1}^\alpha = \mathbf{0}, \tag{2.8}$$

where

$$\mathbf{v} \equiv \{(2\mathbf{I} - \mathbf{V}^{-1}(E\mathbf{I} - \mathbf{H}^\beta)\mathbf{V}^{-1}(E\mathbf{I} - \mathbf{H}^\alpha)\}. \tag{2.9}$$

Substituting Bloch's theorem

$$\mathbf{C}_{j+1}^\alpha = \lambda\mathbf{C}_j^\alpha \tag{2.10}$$

to (2.8), we obtain

$$\lambda\mathbf{C}_j^\alpha + \mathbf{v}\mathbf{C}_j^\alpha + \mathbf{C}_{j-1}^\alpha = \mathbf{0}. \tag{2.11}$$

From (2.10) and (2.11), the following eigenvalue equation

$$\lambda \begin{pmatrix} \mathbf{C}_j^\alpha \\ \mathbf{C}_{j-1}^\alpha \end{pmatrix} = \begin{pmatrix} -\mathbf{v} & -\mathbf{I} \\ \mathbf{I} & 0 \end{pmatrix} \begin{pmatrix} \mathbf{C}_j^\alpha \\ \mathbf{C}_{j-1}^\alpha \end{pmatrix} \tag{2.12}$$

is derived. This equation has 2M eigenvalues and 2M eigenvectors, which can be classified into M right-going solutions and M left-going solutions. They consist of traveling modes and evanescent modes. We represent the eigenvalues and eigenvectors corresponding to the right-going modes as $\lambda_1(+)$, ..., $\lambda_M(+)$ and $\mathbf{u}_1(+)$, ..., $\mathbf{u}_M(+)$, and those corresponding to the left-going modes as $\lambda_1(-)$, ..., $\lambda_M(-)$ and $\mathbf{u}_1(-)$, ..., $\mathbf{u}_M(-)$. We then define M $\times$ M matrices $\mathbf{\Lambda}(\pm)$ and $\mathbf{U}(\pm)$ as

$$\mathbf{\Lambda}(\pm) \equiv \begin{pmatrix} \lambda_1(\pm) & & \\ & \ddots & \\ & & \lambda_M(\pm) \end{pmatrix} \tag{2.13}$$

and

$$\mathbf{U}(\pm) \equiv (\mathbf{u}_1(\pm), \ldots, \mathbf{u}_M(\pm)). \tag{2.14}$$

At $j = 0$, any right-going and left-going waves are expressed by a superposition of the corresponding eigenmodes as

$$\mathbf{C}_0^\alpha(\pm) = \mathbf{U}(\pm)\mathbf{C}_\alpha(\pm), \tag{2.15}$$

where $\mathbf{C}_\alpha(\pm)$ is an appropriate vector consisting of expansion coefficients. At arbitrary j, they are expressed as

$$\begin{aligned}
\mathbf{C}_j^\alpha(\pm) &= \mathbf{U}(\pm)\mathbf{\Lambda}(\pm)^j\mathbf{C}_\alpha(\pm) \\
&= \mathbf{U}(\pm)\mathbf{\Lambda}(\pm)\mathbf{U}(\pm)^{-1}\mathbf{U}(\pm)\mathbf{\Lambda}(\pm)\mathbf{U}(\pm)^{-1}\cdots\mathbf{\Lambda}(\pm)\mathbf{C}_\alpha(\pm) \\
&= (\mathbf{U}(\pm)\mathbf{\Lambda}(\pm)\mathbf{U}(\pm)^{-1})^{j-j'}\mathbf{U}(\pm)\mathbf{\Lambda}(\pm)^{j'}\mathbf{C}_\alpha(\pm) \\
&= \mathbf{F}(\pm)^{j-j'}\mathbf{C}_{j'}^\alpha(\pm),
\end{aligned} \tag{2.16}$$

where

$$\mathbf{F}(\pm) \equiv \mathbf{U}(\pm)\mathbf{\Lambda}(\pm)\mathbf{U}(\pm)^{-1}. \tag{2.17}$$
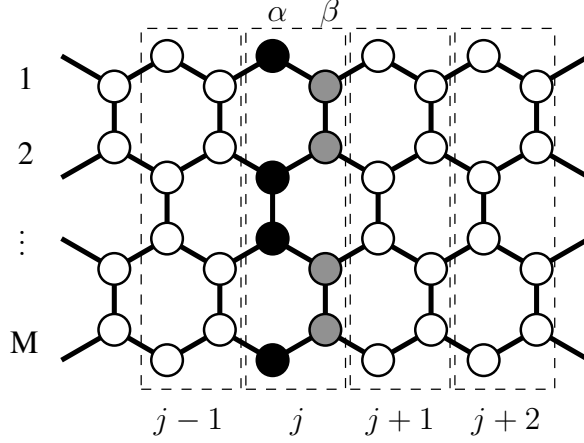
Figure 2.4: The illustration of a zigzag nanoribbon of width M. Rectangles with dashed line indicate unit cells. Black and gray circles in the jth unit cell indicate sites belong to the α and β columns, respectively.

2.2.2 Scattering problem

Let us consider the scattering problem in a disordered zigzag nanoribbon to obtain the transmission and reflection matrices, from which we can determine the conductance of the system. We assume that the scatterers are distributed over sites in unit cells of $j = 1, 2, \ldots$, $N - 1$, N. The length L of the disordered region is simply given by $L = Na$ with a being the lattice constant. The 0th cell corresponds to the end of the left lead, and the N + 1th cell corresponds to the end of the right lead. In the 0th unit cell, the column vectors satisfy

$$(E\mathbf{I} - \mathbf{H}^\alpha)\mathbf{C}_0^\alpha - \mathbf{V}\mathbf{C}_{-1}^\beta - \mathbf{V}\mathbf{C}_0^\beta = \mathbf{0}, \tag{2.18}$$

$$(E\mathbf{I} - \mathbf{H}^\beta)\mathbf{C}_{-1}^\beta - \mathbf{V}\mathbf{C}_{-1}^\alpha - \mathbf{V}\mathbf{C}_0^\alpha = \mathbf{0}. \tag{2.19}$$

Eliminating $\mathbf{C}_{-1}^\beta$, we obtain

$$\left[E\mathbf{I} - \left\{ \mathbf{H}^\alpha + \mathbf{V}(E\mathbf{I} - \mathbf{H}^\beta)^{-1}\mathbf{V} \right\} \right] \mathbf{C}_0^\alpha - \mathbf{V}\mathbf{C}_0^\beta - \mathbf{V}(E\mathbf{I} - \mathbf{H}^\beta)^{-1}\mathbf{V}\mathbf{C}_{-1}^\alpha = \mathbf{0}. \tag{2.20}$$

In terms of $\mathbf{H}_{\mathrm{L}}$, $\mathbf{U}_{\mathrm{L}}$, and $\mathbf{V}_{\mathrm{L}}$ defined by

$$\mathbf{H}_{\mathrm{L}} \equiv \mathbf{H}^\alpha + \mathbf{V}(E\mathbf{I} - \mathbf{H}^\beta)^{-1}\mathbf{V}, \tag{2.21}$$

$$\mathbf{U}_{\mathrm{L}} \equiv \mathbf{V}(E\mathbf{I} - \mathbf{H}^\beta)^{-1}\mathbf{V}, \tag{2.22}$$

$$\mathbf{V}_{\mathrm{L}} \equiv \mathbf{V}, \tag{2.23}$$

we rewrite (2.20) as

$$[E\mathbf{I} - \mathbf{H}_{\mathrm{L}}] \mathbf{C}_0^\alpha - \mathbf{V}_{\mathrm{L}}\mathbf{C}_0^\beta - \mathbf{U}_{\mathrm{L}}\mathbf{C}_{-1}^\alpha = \mathbf{0}. \tag{2.24}$$

The column vectors can be expressed by a superposition of right-going and left-going waves. For example, the column vector at $j = 0$ is given by

$$\mathbf{C}_0^\alpha = \mathbf{C}_0^\alpha(+) + \mathbf{C}_0^\alpha(-). \tag{2.25}$$

11

The column vector at $j = -1$ is also given by

$$
\begin{aligned}
\mathbf{C}^\alpha_{-1} &= \mathbf{C}^\alpha_{-1}(+) + \mathbf{C}^\alpha_{-1}(-) \\
&= \mathbf{F}(+)^{-1}\mathbf{C}^\alpha_0(+)\mathbf{F}(-)^{-1}\mathbf{C}^\alpha_0(-) \\
&= \mathbf{F}(-)^{-1}\mathbf{C}^\alpha_0 + \{\mathbf{F}(+)^{-1} - \mathbf{F}(-)^{-1}\}\mathbf{C}^\alpha_0(+),
\end{aligned}
\tag{2.26}
$$

where (2.16) is used. Substituting (2.26) to (2.24), we obtain

$$
\left[E\mathbf{I} - \tilde{\mathbf{H}}_\mathrm{L}\right]\mathbf{C}^\alpha_0 - \mathbf{V}_\mathrm{L}\mathbf{C}^\beta_0 = \mathbf{U}_\mathrm{L}(\mathbf{F}(+)^{-1} - \mathbf{F}(-)^{-1})\mathbf{C}^\alpha_0(+),
\tag{2.27}
$$

where

$$
\tilde{\mathbf{H}}_\mathrm{L} \equiv \mathbf{H}_\mathrm{L} + \mathbf{U}_\mathrm{L}\mathbf{F}(-)^{-1}.
\tag{2.28}
$$

In the $N + 1$th unit cell, the column vectors satisfy the following equations:

$$
(E\mathbf{I} - \mathbf{H}^\alpha)\mathbf{C}^\alpha_{N+1} - \mathbf{V}\mathbf{C}^\beta_{N+1} - \mathbf{V}\mathbf{C}^\beta_N = \mathbf{0},
\tag{2.29}
$$

$$
(E\mathbf{I} - \mathbf{H}^\beta)\mathbf{C}^\beta_{N+1} - \mathbf{V}\mathbf{C}^\alpha_{N+2} - \mathbf{V}\mathbf{C}^\alpha_{N+1} = \mathbf{0}.
\tag{2.30}
$$

Eliminating $\mathbf{C}^\beta_{N+1}$ from (2.29) and (2.30), we obtain

$$
\left[E\mathbf{I} - \left\{\mathbf{H}^\alpha + \mathbf{V}(E\mathbf{I} - \mathbf{H}^\beta)^{-1}\mathbf{V}\right\}\right]\mathbf{C}^\alpha_{N+1} - \mathbf{V}\mathbf{C}^\beta_N - \mathbf{V}(E\mathbf{I} - \mathbf{H}^\beta)^{-1}\mathbf{V}\mathbf{C}^\alpha_{N+2} = \mathbf{0}.
\tag{2.31}
$$

In terms of $\mathbf{H}_\mathrm{R}$, $\mathbf{V}_\mathrm{R}$, and $\mathbf{U}_\mathrm{R}$ defined by

$$
\mathbf{H}_\mathrm{R} \equiv \mathbf{H}^\alpha + \mathbf{V}(E\mathbf{I} - \mathbf{H}^\beta)^{-1}\mathbf{V},
\tag{2.32}
$$

$$
\mathbf{V}_\mathrm{R} \equiv \mathbf{V}(E\mathbf{I} - \mathbf{H}^\beta)^{-1}\mathbf{V},
\tag{2.33}
$$

$$
\mathbf{U}_\mathrm{R} \equiv \mathbf{V},
\tag{2.34}
$$

we rewrite (2.31) as

$$
[E\mathbf{I} - \mathbf{H}_\mathrm{R}]\mathbf{C}^\alpha_{N+1} - \mathbf{U}_\mathrm{R}\mathbf{C}^\beta_N - \mathbf{V}_\mathrm{R}\mathbf{C}^\alpha_{N+2} = \mathbf{0}.
\tag{2.35}
$$

In the $N + 1$th unit cell, only the right-going wave is present as

$$
\mathbf{C}^\alpha_{N+2} = \mathbf{F}(+)\mathbf{C}^\alpha_{N+1}.
\tag{2.36}
$$

Thus, we can modify (2.35) as

$$
\left[E\mathbf{I} - \tilde{\mathbf{H}}_\mathrm{R}\right]\mathbf{C}^\alpha_{N+1} - \mathbf{U}_\mathrm{R}\mathbf{C}^\beta_N = \mathbf{0},
\tag{2.37}
$$

where

$$
\tilde{\mathbf{H}}_\mathrm{R} \equiv \mathbf{H}_\mathrm{R} + \mathbf{V}_\mathrm{R}\mathbf{F}(+).
\tag{2.38}
$$

The above argument allows us to express the Schrödinger equation in the following form:

$$
(E\mathbf{I} - \tilde{\mathbf{H}})\mathbf{C} = \mathbf{D},
\tag{2.39}
$$

where

$$\mathbf{C} = \begin{pmatrix} \mathbf{C}_0^\alpha \\ \mathbf{C}_1^\alpha \\ \mathbf{C}_1^\beta \\ \mathbf{C}_2^\alpha \\ \mathbf{C}_2^\beta \\ \vdots \\ \mathbf{C}_N^\alpha \\ \mathbf{C}_N^\beta \\ \mathbf{C}_{N+1}^\alpha \end{pmatrix}, \tag{2.40}$$

$$\mathbf{D} = \begin{pmatrix} \mathbf{V}_L^\dagger (\mathbf{F}(+)^{-1} - \mathbf{F}(-)^{-1})\mathbf{C}_0^\alpha(+) \\ \vdots \\ \vdots \\ \mathbf{0} \end{pmatrix}, \tag{2.41}$$

and

$$\tilde{\mathbf{H}} = \begin{pmatrix} \tilde{\mathbf{H}}_L & \mathbf{V}_L & & & & \\ \mathbf{V} & \tilde{\mathbf{H}}_1 & \mathbf{V} & & & \\ & \mathbf{V} & \tilde{\mathbf{H}}_2 & \mathbf{V} & & \\ & & \ddots & \ddots & \ddots & \\ & & & \mathbf{V} & \tilde{\mathbf{H}}_N & \mathbf{V} \\ & & & & \mathbf{V}_R & \tilde{\mathbf{H}}_L \end{pmatrix}. \tag{2.42}$$

We define the Green's function as

$$\mathbf{G} \equiv (E\mathbf{I} - \tilde{\mathbf{H}})^{-1}. \tag{2.43}$$

With (2.39), $\mathbf{C}$ is expressed as

$$\mathbf{C} = (E\mathbf{I} - \tilde{\mathbf{H}})^{-1}\mathbf{D} = \mathbf{G}\mathbf{D}. \tag{2.44}$$

We immediately find

$$\mathbf{C}_{N+1}^\alpha(+) = \langle N+1|\mathbf{G}|0\rangle \mathbf{U}_L(\mathbf{F}(+)^{-1} - \mathbf{F}(-)^{-1})\mathbf{C}_0^\alpha(+) \tag{2.45}$$

and

$$\mathbf{C}_0^\alpha(-) = [\langle 0|\mathbf{G}|0\rangle \mathbf{U}_L(\mathbf{F}(+)^{-1} - \mathbf{F}(-)^{-1}) - 1]\mathbf{C}_0^\alpha(+). \tag{2.46}$$

From these equations, the transmission and reflection coefficients for an electron incoming from the left lead are expressed as

$$t_{\mu\nu} = \sqrt{\frac{v_\mu}{v_\nu}} \{ \mathbf{U}(+)^{-1} \langle N+1|\mathbf{G}|0\rangle \mathbf{U}_L(\mathbf{F}(+)^{-1} - \mathbf{F}(-)^{-1})\mathbf{U}(+) \}_{\mu\nu}, \tag{2.47}$$

$$r_{\mu\nu} = \sqrt{\frac{v_\mu}{v_\nu}} \{ \mathbf{U}(-)^{-1}[\langle 0|\mathbf{G}|0\rangle \mathbf{U}_L(\mathbf{F}(+)^{-1} - \mathbf{F}(-)^{-1}) - 1]\mathbf{U}(+) \}_{\mu\nu}, \tag{2.48}$$

where μ and ν respectively represent incoming and outgoing channels, and v_μ is the velocity of the μth channel. The details of the derivation of (2.47) and (2.48) is described in Appendix B. An expression of v_μ is given in Appendix C. In a manner similar to this, the transmission and reflection coefficients for an electron incoming from the right lead are expressed as

$$t'_{\mu\nu} = \sqrt{\frac{v_\mu}{v_\nu}} \{\mathbf{U}(-)^{-1}\langle 0|\mathbf{G}|\mathrm{N}+1\rangle\mathbf{V}_\mathrm{R}(\mathbf{F}(-)-\mathbf{F}(+))\mathbf{U}(-)\}_{\mu\nu}, \tag{2.49}$$

$$r'_{\mu\nu} = \sqrt{\frac{v_\mu}{v_\nu}} \{\mathbf{U}(+)^{-1}[\langle \mathrm{N}+1|\mathbf{G}|\mathrm{N}+1\rangle\mathbf{V}_\mathrm{L}(\mathbf{F}(-)-\mathbf{F}(+)) - 1]\mathbf{U}(-)\}_{\mu\nu}. \tag{2.50}$$

2.2.3 Recursive Green's function method

We use a recursive Green's function method to calculate the Green's functions in (2.47), (2.48), (2.49), and (2.50).[46] Let us define the following functions,

$$\langle j|\mathbf{G}|j\rangle = \langle j|(E\mathbf{I} - \mathbf{H}^{(j)})^{-1}|j\rangle, \tag{2.51}$$

$$\langle j|\mathbf{G}|0\rangle = \langle j|(E\mathbf{I} - \mathbf{H}^{(j)})^{-1}|0\rangle, \tag{2.52}$$

$$\langle 0|\mathbf{G}|j\rangle = \langle 0|(E\mathbf{I} - \mathbf{H}^{(j)})^{-1}|j\rangle, \tag{2.53}$$

$$\langle 0|\mathbf{G}|0\rangle = \langle 0|(E\mathbf{I} - \mathbf{H}^{(j)})^{-1}|0\rangle. \tag{2.54}$$

Here, $\mathbf{H}^{(j)}$ is the total Hamiltonian for the strip comprising the 0th to jth cells excluding the inter-cell Hamiltonians $\tilde{\mathbf{H}}_{j,j+1}$ and $\tilde{\mathbf{H}}_{j+1,j}$. Accordingly, the matrix form of $\mathbf{H}^{(j+1)}$ is represented as

$$\mathbf{H}^{(j+1)} = \begin{pmatrix} & & & & 0 \\ & & & & \vdots \\ & \mathbf{H}^{(j)} & & & \vdots \\ & & & & 0 \\ & & & & \tilde{\mathbf{H}}_{j,j+1} \\ \hline \mathbf{0} & \cdots & \cdots & \mathbf{0} & \tilde{\mathbf{H}}_{j+1,j} & \tilde{\mathbf{H}}_{j+1} \end{pmatrix}. \tag{2.55}$$

Then, the Green's function for a strip of any length can be obtained by using a set of recursive formulas,

$$\langle j+1|\mathbf{G}^{(j+1)}|j+1\rangle^{-1} = E\mathbf{I} - \tilde{\mathbf{H}}_{j+1} - \tilde{\mathbf{H}}_{j+1,j}\langle j|\mathbf{G}^{(j)}|j\rangle\tilde{\mathbf{H}}_{j,j+1}, \tag{2.56}$$

$$\langle j+1|\mathbf{G}^{(j+1)}|0\rangle = \langle j+1|\mathbf{G}^{(j+1)}|j+1\rangle\tilde{\mathbf{H}}_{j+1,j}\langle j|\mathbf{G}^{(j)}|0\rangle, \tag{2.57}$$

$$\langle 0|\mathbf{G}^{(j+1)}|j+1\rangle = \langle 0|\mathbf{G}^{(j)}|j\rangle\tilde{\mathbf{H}}_{j,j+1}\langle j+1|\mathbf{G}^{(j+1)}|j+1\rangle, \tag{2.58}$$

$$\langle 0|\mathbf{G}^{(j+1)}|0\rangle = \langle 0|\mathbf{G}^{(j)}|0\rangle + \langle 0|\mathbf{G}^{(j)}|j\rangle\tilde{\mathbf{H}}_{j,j+1}\langle j+1|\mathbf{G}^{(j+1)}|0\rangle. \tag{2.59}$$

In our case, these formulas are rewritten as

$$\langle j+1|\mathbf{G}^{(j+1)}|j+1\rangle^{-1} = E\mathbf{I} - \tilde{\mathbf{H}}_{j+1} - \mathbf{V}\langle j|\mathbf{G}^{(j)}|j\rangle\mathbf{V}, \tag{2.60}$$

$$\langle j+1|\mathbf{G}^{(j+1)}|0\rangle = \langle j+1|\mathbf{G}^{(j+1)}|j+1\rangle\mathbf{V}\langle j|\mathbf{G}^{(j)}|0\rangle, \tag{2.61}$$

$$\langle 0|\mathbf{G}^{(j+1)}|j+1\rangle = \langle 0|\mathbf{G}^{(j)}|j\rangle\mathbf{V}\langle j+1|\mathbf{G}^{(j+1)}|j+1\rangle, \tag{2.62}$$

$$\langle 0|\mathbf{G}^{(j+1)}|0\rangle = \langle 0|\mathbf{G}^{(j)}|0\rangle + \langle 0|\mathbf{G}^{(j)}|j\rangle\mathbf{V}\langle j+1|\mathbf{G}^{(j+1)}|0\rangle. \tag{2.63}$$

14

In actual application of this recursive method, we use the Green's function defined by

$$\langle 0|\mathbf{G}^{(0)}|0\rangle = (E\mathbf{I} - \tilde{\mathbf{H}}_{\mathrm{L}})^{-1} \tag{2.64}$$

as an initial condition.

2.3 Model of Dephasing

Generally speaking, dephasing suppresses quantum effects, particularly quantum interference effects, and tends to reveal classical behaviors of electrons in some cases. In order to incorporate this effect into our model, we hypothetically decompose the disordered region into N_{s} segments of equal length L_ϕ, as shown in Fig. 2.5, and assume that the phase coherence of electrons is lost across adjacent segments while in each segment the phase coherence is completely preserved.[17] Hence, L_ϕ can be regarded as the phase coherence length. We require the continuity of charge current, instead of the continuity of a wave function, in each channel between adjacent segments. With this procedure, the phase coherence of electrons completely breaks across adjacent segments.

Let us express the transmission and reflection matrices for the nth segment as $\boldsymbol{t}_n$, $\boldsymbol{r}_n$, $\boldsymbol{t}'_n$, and $\boldsymbol{r}'_n$. In terms of them, the transmission probability matrix $\mathcal{T}_n$ ($\mathcal{T}_{\overline{n}}$) and the reflection probability matrix $\mathcal{R}_n$ ($\mathcal{R}_{\overline{n}}$) for an electron incoming from the left (right) are defined as

$$\begin{aligned}
[\mathcal{T}_n]_{\alpha\beta} &= |[\boldsymbol{t}_n]_{\alpha\beta}|^2, \\
[\mathcal{R}_n]_{\alpha\beta} &= |[\boldsymbol{r}_n]_{\alpha\beta}|^2, \\
[\mathcal{T}_{\overline{n}}]_{\alpha\beta} &= |[\boldsymbol{t}'_n]_{\alpha\beta}|^2, \\
[\mathcal{R}_{\overline{n}}]_{\alpha\beta} &= |[\boldsymbol{r}'_n]_{\alpha\beta}|^2.
\end{aligned} \tag{2.65}$$

Let $\boldsymbol{i}_n$ be the right-going current from the nth segment to the $n+1$th segment and $\boldsymbol{i}_{\overline{n}}$ be the left-going current from the $n+1$th segment to the nth segment. They satisfy

$$\boldsymbol{i}_n = \mathcal{T}_n \boldsymbol{i}_{n-1} + \mathcal{R}_{\overline{n}} \boldsymbol{i}_{\overline{n}}, \tag{2.66}$$

$$\boldsymbol{i}_{\overline{n}} = \mathcal{T}_{\overline{n+1}} \boldsymbol{i}_{\overline{n+1}} + \mathcal{R}_{n+1} \boldsymbol{i}_n. \tag{2.67}$$

At the left end, we have

$$\boldsymbol{i}_0 = \boldsymbol{i}_{\mathrm{ext}}, \tag{2.68}$$

$$\boldsymbol{i}_{\overline{0}} = \mathcal{R}_1 \boldsymbol{i}_0 + \mathcal{T}_{\overline{1}} \boldsymbol{i}_{\overline{1}}, \tag{2.69}$$

where $\boldsymbol{i}_{\mathrm{ext}}$ denotes the current supplied from the left lead. At the right end, the current between the N_sth segment and the right lead can be represented as

$$\boldsymbol{i}_{N_s} = \mathcal{T}_{N_s} \boldsymbol{i}_{N_s-1}, \tag{2.70}$$

$$\boldsymbol{i}_{\overline{N}_s} = 0. \tag{2.71}$$

For the system constituted by combining the first, second, ..., nth segments in series, we define $\tilde{\mathcal{T}}_n$ ($\tilde{\mathcal{T}}_{\overline{n}}$) and $\tilde{\mathcal{R}}_n$ ($\tilde{\mathcal{R}}_{\overline{n}}$) as the transmission and reflection probability matrices for

an electron incoming from the left (right), respectively. Adding the $n+1$th segment to the system consisting of n segments, we consider the combined system to derive a relation between the probability matrices for the system with n segments and those for the system with $n+1$th segments. For the combined system with $n+1$ segments, we have

$$\boldsymbol{i}_n = \tilde{\mathcal{T}}_n \boldsymbol{i}_0 + \tilde{\mathcal{R}}_{\bar{n}} \boldsymbol{i}_{\bar{n}}, \tag{2.72}$$

$$\boldsymbol{i}_{\bar{n}} = \mathcal{T}_{\overline{n+1}} \boldsymbol{i}_{\overline{n+1}} + \mathcal{R}_{n+1} \boldsymbol{i}_n, \tag{2.73}$$

and

$$\boldsymbol{i}_{\bar{0}} = \tilde{\mathcal{R}}_n \boldsymbol{i}_0 + \tilde{\mathcal{T}}_{\bar{n}} \boldsymbol{i}_{\bar{n}}, \tag{2.74}$$

$$\boldsymbol{i}_{n+1} = \mathcal{T}_{n+1} \boldsymbol{i}_n + \mathcal{R}_{\overline{n+1}} \boldsymbol{i}_{\overline{n+1}}, \tag{2.75}$$

which are respectively rewritten in a matrix form as

$$\begin{pmatrix} \boldsymbol{i}_n \\ \boldsymbol{i}_{\bar{n}} \end{pmatrix} = \begin{pmatrix} 1 & -\tilde{\mathcal{R}}_{\bar{n}} \\ -\mathcal{R}_{n+1} & 1 \end{pmatrix}^{-1} \begin{pmatrix} \tilde{\mathcal{T}}_n & 0 \\ 0 & \mathcal{T}_{\overline{n+1}} \end{pmatrix} \begin{pmatrix} \boldsymbol{i}_0 \\ \boldsymbol{i}_{\overline{n+1}} \end{pmatrix}, \tag{2.76}$$

and

$$\begin{pmatrix} \boldsymbol{i}_{\bar{0}} \\ \boldsymbol{i}_{n+1} \end{pmatrix} = \begin{pmatrix} \tilde{\mathcal{R}}_n & 0 \\ 0 & \mathcal{R}_{\overline{n+1}} \end{pmatrix} \begin{pmatrix} \boldsymbol{i}_0 \\ \boldsymbol{i}_{\overline{n+1}} \end{pmatrix} + \begin{pmatrix} 0 & \tilde{\mathcal{T}}_{\bar{n}} \\ \mathcal{T}_{n+1} & 0 \end{pmatrix} \begin{pmatrix} \boldsymbol{i}_n \\ \boldsymbol{i}_{\bar{n}} \end{pmatrix}. \tag{2.77}$$

Eliminating $\boldsymbol{i}_n$ and $\boldsymbol{i}_{\bar{n}}$ in (2.77) by using (2.76), we obtain

$$\begin{pmatrix} \boldsymbol{i}_{\bar{0}} \\ \boldsymbol{i}_{n+1} \end{pmatrix} = \left[\begin{pmatrix} \tilde{\mathcal{R}}_n & 0 \\ 0 & \mathcal{R}_{\overline{n+1}} \end{pmatrix} + \begin{pmatrix} 0 & \tilde{\mathcal{T}}_{\bar{n}} \\ \mathcal{T}_{n+1} & 0 \end{pmatrix} \begin{pmatrix} 1 & -\tilde{\mathcal{R}}_{\bar{n}} \\ -\mathcal{R}_{n+1} & 1 \end{pmatrix}^{-1} \begin{pmatrix} \tilde{\mathcal{T}}_n & 0 \\ 0 & \mathcal{T}_{\overline{n+1}} \end{pmatrix} \right] \begin{pmatrix} \boldsymbol{i}_0 \\ \boldsymbol{i}_{\overline{n+1}} \end{pmatrix}. \tag{2.78}$$

Comparing this with the equation that defines $\tilde{\mathcal{T}}_{n+1}$, $\tilde{\mathcal{T}}_{\overline{n+1}}$, $\tilde{\mathcal{R}}_{n+1}$, and $\tilde{\mathcal{R}}_{\overline{n+1}}$, i.e.,

$$\begin{pmatrix} \boldsymbol{i}_{\bar{0}} \\ \boldsymbol{i}_{n+1} \end{pmatrix} = \begin{pmatrix} \tilde{\mathcal{R}}_{n+1} & \tilde{\mathcal{T}}_{\overline{n+1}} \\ \tilde{\mathcal{T}}_{n+1} & \tilde{\mathcal{R}}_{\overline{n+1}} \end{pmatrix} \begin{pmatrix} \boldsymbol{i}_0 \\ \boldsymbol{i}_{\overline{n+1}} \end{pmatrix}, \tag{2.79}$$

we obtain the following recurrence relation:[17]

$$\begin{pmatrix} \tilde{\mathcal{R}}_{n+1} & \tilde{\mathcal{T}}_{\overline{n+1}} \\ \tilde{\mathcal{T}}_{n+1} & \tilde{\mathcal{R}}_{\overline{n+1}} \end{pmatrix} = \begin{pmatrix} \tilde{\mathcal{R}}_n & 0 \\ 0 & \mathcal{R}_{\overline{n+1}} \end{pmatrix} + \begin{pmatrix} 0 & \tilde{\mathcal{T}}_{\bar{n}} \\ \mathcal{T}_{n+1} & 0 \end{pmatrix} \begin{pmatrix} 1 & -\tilde{\mathcal{R}}_{\bar{n}} \\ -\mathcal{R}_{n+1} & 1 \end{pmatrix}^{-1} \begin{pmatrix} \tilde{\mathcal{T}}_n & 0 \\ 0 & \mathcal{T}_{\overline{n+1}} \end{pmatrix} \tag{2.80}$$

with $\tilde{\mathcal{T}}_1 = \mathcal{T}_1$, $\tilde{\mathcal{R}}_1 = \mathcal{R}_1$, $\tilde{\mathcal{T}}_{\bar{1}} = \mathcal{T}_{\bar{1}}$, and $\tilde{\mathcal{R}}_{\bar{1}} = \mathcal{R}_{\bar{1}}$. By using this relation recursively, we can calculate $\tilde{\mathcal{T}}_{N_s}$ once the transmission and reflection probability matrices for all segments are given. The dimensionless conductance is expressed as

$$g = \sum_{\alpha,\beta=1}^{N_c} \left[\tilde{\mathcal{T}}_{N_s} \right]_{\beta\alpha} \tag{2.81}$$
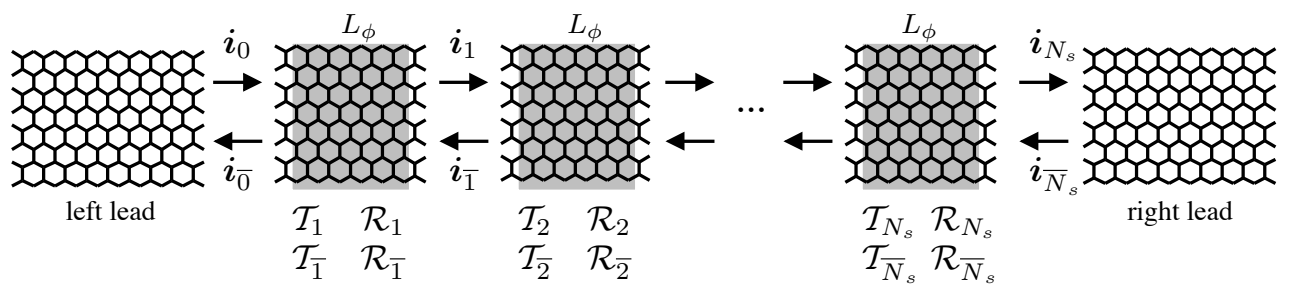
in the presence of dephasing.

Figure 2.5: Hypothetical decomposition of the disordered region of length L into N_s segments of equal length L_ϕ. We assume that the phase coherence of electrons is lost across adjacent segments.

Chapter 3

Results and Discussion

3.1   Numerical Results

We present the results of numerical calculations of the dimensionless conductance g. We separately consider the case with LRIs and that with SRIs. In the former case, we expect that a PCC appears as intervalley scattering is sufficiently weak, while strong intervalley scattering forbids its appearance in the latter case. These two cases are realized by appropriately choosing d. With $P = 0.1$, we set $d/a = 1.5$ and $u_{max}/t = 0.1$ in the LRI case, and $d/a = 0.05$ and $u_{max}/t = 1.0$ in the SRI case. We fix $M = 30$ and $E/t = 0.36$ in the following calculations. The number of conducting channels is equal to $N_c = 7$ in both the cases.

Let us consider the LRI case. We use 2000 samples with different impurity configurations to calculate the average dimensionless conductance $\langle g \rangle$. Fig. 3.1 shows $\langle g \rangle$ as a function of L/a. We observe that $\langle g \rangle$ rapidly decreases to 1 with increasing L/a and then the decrease becomes very slow once it decays below 1, indicating the presence of a PCC. In the regime of $\langle g \rangle \lesssim 1$, the decay of $\langle g \rangle$ becomes slower as L_ϕ becomes smaller. This can be explained by considering that the decay of $\langle g \rangle$ below 1 is accelerated by Anderson localization. The effect of Anderson localization is suppressed by dephasing and hence the decay of $\langle g \rangle$ is also suppressed with decreasing L_ϕ. This indicates that dephasing indirectly stabilizes a PCC, although dephasing itself does not weaken intervalley scattering. We observe the quasi-quantization of $\langle g \rangle$ (i.e., $\langle g \rangle \sim 1$) in a wide region of L/a when L_ϕ is sufficiently small. Fig. 3.2 shows a semilog plot of $\langle g \rangle - 1$. Error bars at each data point represent $(\mathrm{var}\{g\}/N_{sam})^{1/2}$, where $\mathrm{var}\{g\} = \langle g^2 \rangle - \langle g \rangle^2$ and N_{sam} is the number of samples used to calculate the average. We find that $\langle g \rangle$ decreases exponentially toward 1 in a certain region of L/a in all cases. In the case without dephasing, this is in accordance with existing random matrix theory.[47] Fig. 3.3 shows a semilog plot of $\langle g \rangle$ in the regime of $\langle g \rangle < 1$. We find that $\langle g \rangle$ decays exponentially regardless of L_ϕ. In the absence of dephasing, it is natural that $\langle g \rangle$ decays exponentially, reflecting the onset of Anderson localization. The exponential decay of $\langle g \rangle$ even in the presence of dephasing should be regarded as a characteristic feature of the system in which conducting channels are imbalanced between two propagating directions.[41]

We turn to the SRI case. We use 10000 samples with different impurity configurations to calculate the average dimensionless conductance $\langle g \rangle$. Fig. 3.4 shows $\langle g \rangle$ as a function of L/a. We observe that $\langle g \rangle$ decays to zero with increasing L/a, indicating the absence of a PCC. Fig. 3.5 shows a log-log plot of $\langle g \rangle$ in the presence of dephasing. We find that

$\langle g \rangle$ asymptotically becomes inversely proportional to L/a, manifesting that Ohm's law is satisfied upon the suppression of Anderson localization due to dephasing. This implies that the conducting channels are balanced as a consequence of the mixing of two valleys caused by strong intervalley scattering, in contrast to the LRI case. In the absence of dephasing, $\langle g \rangle$ decays exponentially with increasing L/a as shown in Fig. 3.6. We show error bars only in Fig. 3.6 as they are very small in the case with dephasing.
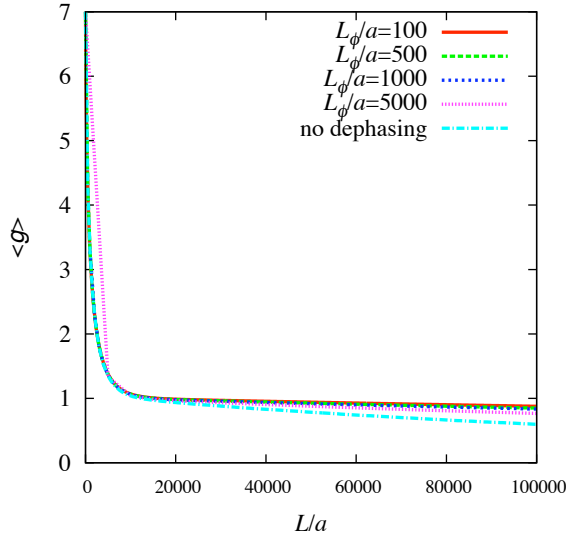
Figure 3.1: Average dimensionless conductance $\langle g \rangle$ in the LRI case for several values of L_ϕ/a.

3.2 Comparison with the Boltzmann Transport Theory

In this section, we introduce an analytical expression for the dimensionless conductance derived from the Boltzmann transport equation[41] and compare it with the numerical results given in the previous section.

The analytical expression of Ref. 41 is derived by applying the Boltzmann transport equation to a simple model for zigzag nanoribbons and hence is justified in the incoherent limit where the phase coherence of electrons is completely lost. The model possesses two energy valleys, and the number of conducting channels for right-going (left-going) electrons is $n_c + 1$ (n_c) in one valley, while in the other valley, that for right-going (left-going) electrons is n_c ($n_c + 1$). The total number of conducting channels is given by $N_c = 2n_c + 1$ including contributions from the two valleys. Disorder induces intravalley scattering between two channels in the same valley and intervalley scattering between two channels belonging to different valleys. The strength of intravalley scattering is characterized by a single parameter κ as its detailed dependence on initial and final states is ignored. In the same manner, the strength of intervalley scattering is characterized by a parameter κ'. Applying a constant electric field only in the region of length L, the Boltzmann equation is solved under the condition that incident electrons from the left and right are described by equilibrium distributions. The
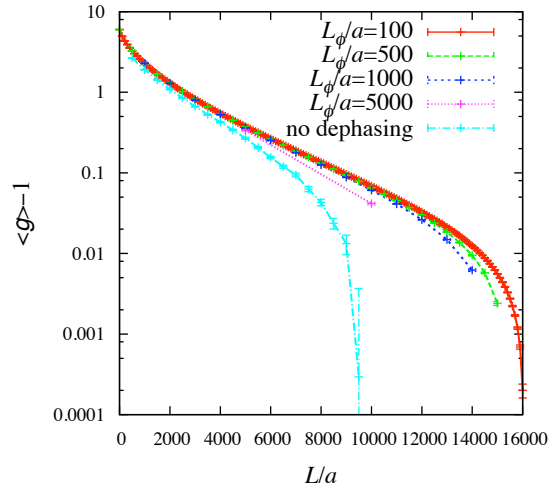
19

Figure 3.2: Semilog plot of $\langle g \rangle - 1$ in the case of LRI. In a certain region of L/a, $\langle g \rangle$ decreases exponentially toward 1 as a function of L/a.
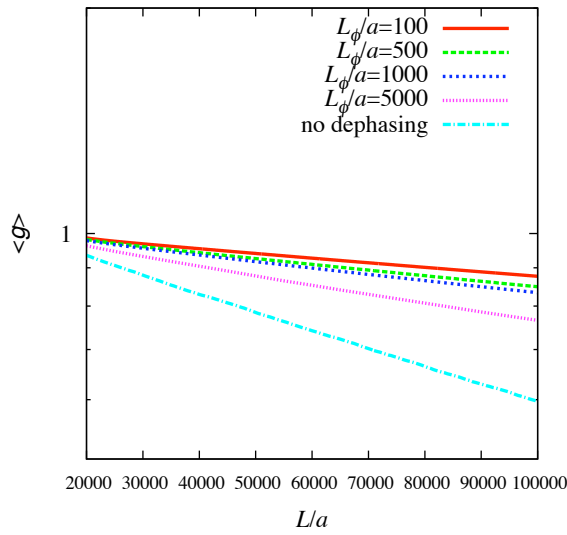

Figure 3.3: Semilog plot of $\langle g \rangle$ in the LRI case in the regime of $\langle g \rangle < 1$. $\langle g \rangle$ decays exponentially as a function of L/a even in the presence of dephasing.
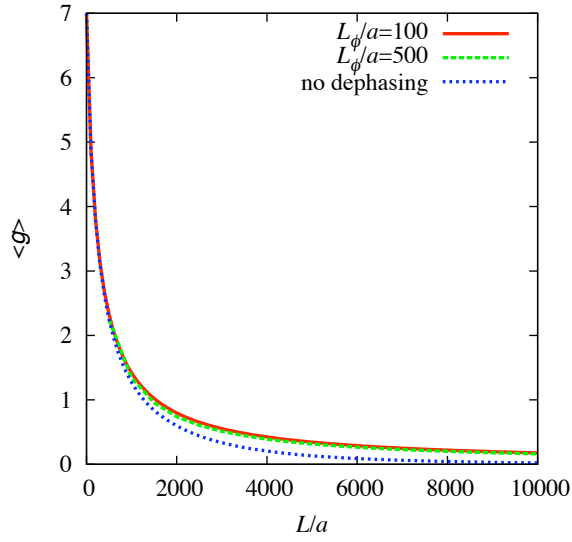
20

Figure 3.4: Average dimensionless conductance $\langle g \rangle$ in the SRI case.
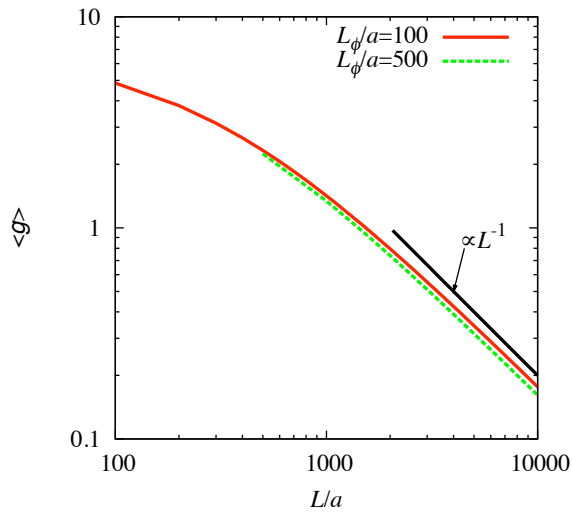

Figure 3.5: Log-log plot of $\langle g \rangle$ in the SRI case with dephasing. $\langle g \rangle$ asymptotically becomes inversely proportional to L/a.
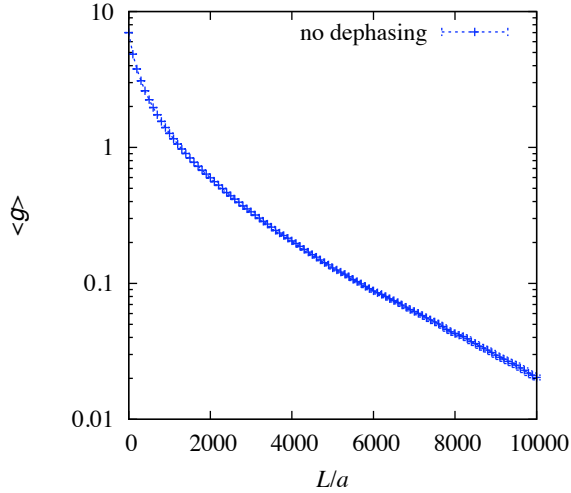
Figure 3.6: Semilog plot of $\langle g \rangle$ in the SRI case with no dephasing. $\langle g \rangle$ decays exponentially as a function of L/a.

resulting dimensionless conductance g_B is expressed as[41]

$$g_B = \frac{\left[\kappa + (8n_c^2 + 8n_c + 1)\kappa'\right] c_L}{(2n_c + 1)\kappa' \left[2 + (2n_c + 1)(\kappa + \kappa')L\right] c_L + \frac{\kappa^2 - \kappa'^2}{\sqrt{\alpha}} d_L}, \tag{3.1}$$

where $\alpha = (\kappa + \kappa')[\kappa + (8n_c^2 + 8n_c + 1)\kappa']$ and

$$c_L = \frac{(2n_c + 1)(\kappa + \kappa')}{\sqrt{\alpha}} \cosh(\sqrt{\alpha}L/2) + \sinh(\sqrt{\alpha}L/2), \tag{3.2}$$

$$d_L = \frac{(2n_c + 1)(\kappa + \kappa')}{\sqrt{\alpha}} \sinh(\sqrt{\alpha}L/2) + \cosh(\sqrt{\alpha}L/2). \tag{3.3}$$

The details of the derivation of (3.1) is described in Appendix D.

We examine whether this expression can fit our numerical results. Equation (3.1) is justified in the incoherent limit, so we focus on the numerical results in the smallest-L_ϕ case with $L_\phi/a = 100$. As $N_c = 7$ in our setting, n_c is fixed at $n_c = 3$. Only κ and κ' play the role of fitting parameters. The result of fitting is shown in Fig. 3.7 in the LRI case and Fig. 3.8 in the SRI case. We observe that the analytical expression accurately reproduces the numerical results. The best fitting is achieved for $\kappa a = 0.00031$ and $\kappa' a = 0.00000003$ in the former case, yielding $\kappa'/\kappa = 0.0000096$, and for $\kappa a = 0.00094$ and $\kappa' a = 0.00021$ in the latter case, yielding $\kappa'/\kappa = 0.223$. This result clearly indicates that intervalley scattering is significantly weaker than intravalley scattering in the LRI case while their strengths are on the same order of magnitude in the SRI case.

One may think that the effect of dephasing is oversimplified in the model used in our numerical calculations. However, the above result implies that our model captures the essential features of dephasing in spite of its simplicity.
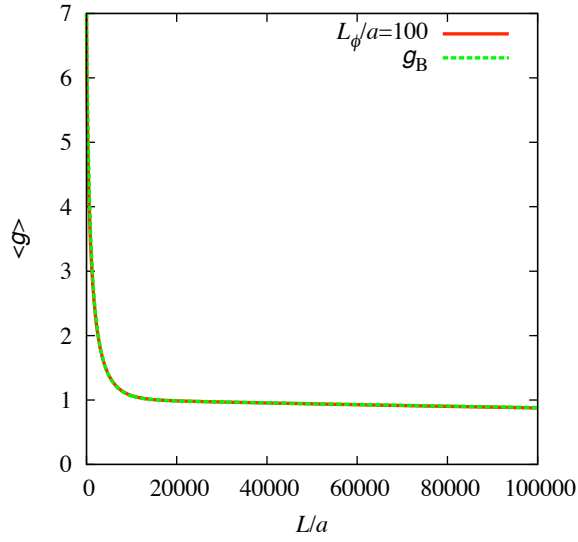
22

Figure 3.7: Fitting of $\langle g \rangle$ at $L_\phi/a = 100$ in the LRI case with the analytical expression g_{B}.
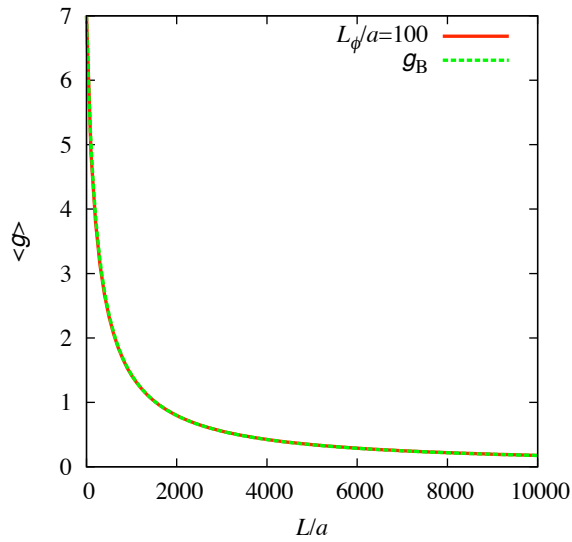

Figure 3.8: Fitting of $\langle g \rangle$ at $L_\phi/a = 100$ in the SRI case with the analytical expression g_{B}.

Chapter 4

Conclusion

We have studied the effect of dephasing on a perfectly conducting channel (PCC) in disordered graphene nanoribbons with zigzag edges by numerically calculating the average dimensionless conductance $\langle g \rangle$ as a function of system length L. We separately consider the case with long-range impurities (LRIs) and that with short-range impurities (SRIs). In the former case, intervalley scattering is very weak and the appearance of a PCC is expected. Contrastingly, a PCC cannot appear owing to strong intervalley scattering in the latter case. The result of the LRI case indicates that $\langle g \rangle$ as a function of L shows two-stage behavior; $\langle g \rangle$ rapidly decreases to 1 with increasing L in the first stage and then tends to decay below 1 in the second stage. The behavior in the first stage implies the presence of a PCC, and the behavior in the second stage indicates that the PCC is destabilized by weak intervalley scattering. We have clearly observed that dephasing significantly relaxes the second-stage behavior and hence effectively stabilizes the PCC. This stabilization should be attributed to the suppression of Anderson localization due to dephasing. In the SRI case, $\langle g \rangle$ decays toward zero, reflecting the absence of a PCC. We have shown that dephasing suppresses the effect of Anderson localization, revealing the behavior of $\langle g \rangle \propto L^{-1}$ in accordance with the ordinary Ohm's law.

One may think that the experimental detection of a PCC in realistic systems is not easy as various inelastic processes obstruct it. Among them, dephasing is known as the most notable factor that suppresses quantum behaviors of electrons at low temperatures. Indeed, it has been pointed out that a PCC in CNTs, as well as in topological insulators, is fragile against dephasing.[17] Contrastingly, in graphene nanoribbons, dephasing does not negatively influence a PCC but rather encourages its appearance. We conclude that graphene nanoribbons with zigzag edges are a promising platform for the experimental detection of a PCC.

Appendix A

Stabilization Mechanism of a PCC

We explain the stabilization mechanism of a PCC in zigzag nanoribbons. We start our argument by considering the scattering problem in an arbitrary disordered quantum wire with left and right leads (see Fig. A.1). Generally speaking, the scattering problem is fully described by the scattering matrix $\mathbf{S}$ consisting of reflection and transmission matrices. In terms of $\mathbf{S}$, the amplitude $\mathbf{O}$ of an electron outgoing from the system is related to the amplitude $\mathbf{I}$ of an electron incoming into the system as

$$\mathbf{O} = \mathbf{S}\mathbf{I}. \tag{A.1}$$

Here, $\mathbf{O}$ and $\mathbf{I}$ consist of the left-going and right-going components as

$$\mathbf{O} = \begin{pmatrix} \mathbf{O}_\mathrm{L} \\ \mathbf{O}_\mathrm{R} \end{pmatrix}, \tag{A.2}$$

$$\mathbf{I} = \begin{pmatrix} \mathbf{I}_\mathrm{L} \\ \mathbf{I}_\mathrm{R} \end{pmatrix}, \tag{A.3}$$

and $\mathbf{S}$ is expressed as

$$\mathbf{S} = \begin{pmatrix} \boldsymbol{r} & \boldsymbol{t}' \\ \boldsymbol{t} & \boldsymbol{r}' \end{pmatrix}, \tag{A.4}$$

where $\boldsymbol{r}$ ($\boldsymbol{r}'$) and $\boldsymbol{t}$ ($\boldsymbol{t}'$) are the reflection and transmission matrices for an electron incoming from the left (right) lead. The inner product of (A.1) with its hermitian conjugate $\mathbf{O}^\dagger = \mathbf{I}^\dagger \mathbf{S}^\dagger$ is given by

$$\mathbf{O}^\dagger \mathbf{O} = \mathbf{I}^\dagger \mathbf{S}^\dagger \mathbf{S} \mathbf{I}. \tag{A.5}$$

The flux conservation relation of

$$\mathbf{O}^\dagger \mathbf{O} = \mathbf{I}^\dagger \mathbf{I} \tag{A.6}$$

requires $\mathbf{S}^\dagger \mathbf{S} = \mathbf{S}\mathbf{S}^\dagger = \mathbf{1}$. This yields

$$\mathbf{S}^\dagger \mathbf{S} = \begin{pmatrix} \boldsymbol{r}^\dagger & \boldsymbol{t}^\dagger \\ \boldsymbol{t}'^\dagger & \boldsymbol{r}'^\dagger \end{pmatrix} \begin{pmatrix} \boldsymbol{r} & \boldsymbol{t}' \\ \boldsymbol{t} & \boldsymbol{r}' \end{pmatrix} = \begin{pmatrix} \boldsymbol{r}^\dagger \boldsymbol{r} + \boldsymbol{t}^\dagger \boldsymbol{t} & \boldsymbol{r}^\dagger \boldsymbol{t}' + \boldsymbol{t}^\dagger \boldsymbol{r}' \\ \boldsymbol{t}'^\dagger \boldsymbol{r} + \boldsymbol{r}'^\dagger \boldsymbol{t} & \boldsymbol{t}'^\dagger \boldsymbol{t}' + \boldsymbol{r}'^\dagger \boldsymbol{r}' \end{pmatrix} = \begin{pmatrix} \mathbf{1} & \mathbf{0} \\ \mathbf{0} & \mathbf{1} \end{pmatrix}, \tag{A.7}$$
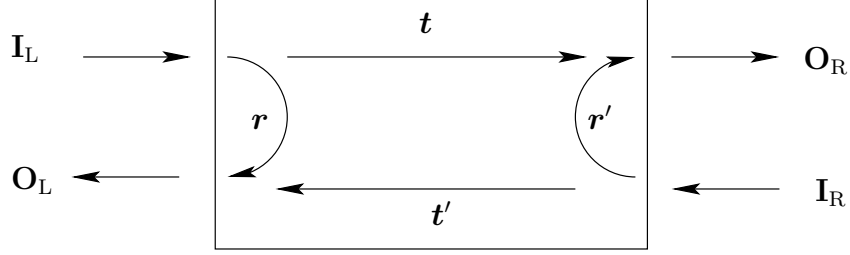
Figure A.1: Schematic figure of the scattering in a quantum wire. $\mathbf{I}_L$ ($\mathbf{I}_R$) denotes the amplitude of an electron incoming from the left (right) lead, and $\mathbf{O}_L$ ($\mathbf{O}_R$) denotes the amplitude of an electron outgoing to the left (right) lead. $\boldsymbol{r}$ ($\boldsymbol{r'}$) and $\boldsymbol{t}$ ($\boldsymbol{t'}$) are the reflection and transmission matrices for an electron incoming from the left (right) lead.

$$\mathbf{SS}^\dagger = \begin{pmatrix} \boldsymbol{r} & \boldsymbol{t'} \\ \boldsymbol{t} & \boldsymbol{r'} \end{pmatrix} \begin{pmatrix} \boldsymbol{r}^\dagger & \boldsymbol{t}^\dagger \\ \boldsymbol{t'}^\dagger & \boldsymbol{r'}^\dagger \end{pmatrix} = \begin{pmatrix} \boldsymbol{rr}^\dagger + \boldsymbol{t't'}^\dagger & \boldsymbol{rt}^\dagger + \boldsymbol{t'r'}^\dagger \\ \boldsymbol{tr}^\dagger + \boldsymbol{r't'}^\dagger & \boldsymbol{tt}^\dagger + \boldsymbol{r'r'}^\dagger \end{pmatrix} = \begin{pmatrix} \mathbf{1} & \mathbf{0} \\ \mathbf{0} & \mathbf{1} \end{pmatrix}, \tag{A.8}$$

which result in

$$\boldsymbol{r}^\dagger \boldsymbol{r} + \boldsymbol{t}^\dagger \boldsymbol{t} = \mathbf{1}, \tag{A.9}$$

$$\boldsymbol{t'}^\dagger \boldsymbol{t'} + \boldsymbol{r'}^\dagger \boldsymbol{r'} = \mathbf{1}, \tag{A.10}$$

$$\boldsymbol{rr}^\dagger + \boldsymbol{t't'}^\dagger = \mathbf{1}, \tag{A.11}$$

$$\boldsymbol{tt}^\dagger + \boldsymbol{r'r'}^\dagger = \mathbf{1}. \tag{A.12}$$

Now, using the general scattering argument given above, we show why a PCC is stabilized in zigzag nanoribbons in the absence of intervalley scattering. As shown in Fig. A.2, the band structure of a zigzag nanoribbon has two valleys, K_- and K_+, and one excess right-going (left-going) channel always exists in the K_- (K_+) valley. That is, although the numbers of right-going and left-going channels are balanced as a whole system, there is always one excess channel in one direction if we focus on one of the two valleys. In the absence of intervalley scattering, each valley independently contributes electron transport, so we can separately consider the two valleys in considering a PCC. Let us focus on the K_- valley, in which an excess right-going channel is present. In this case, the numbers of right-going and left-going channels are respectively denoted as $n_c + 1$ and n_c. Hence, the dimensions of $\mathbf{I}_L$ and $\mathbf{O}_R$ are n_c+1, and those of $\mathbf{I}_R$ and $\mathbf{O}_L$ are n_c. Therefore, the dimensions of $\boldsymbol{r}$ are $n_c \times (n_c+1)$ and those of $\boldsymbol{r'}$ are $(n_c+1) \times n_c$. Thus, we find that $\boldsymbol{r}^\dagger \boldsymbol{r}$ and $\boldsymbol{r'r'}^\dagger$ with dimensions $(n_c+1) \times (n_c+1)$ have a single zero eigenvalue since $\mathrm{rank}(\boldsymbol{r}) = \mathrm{rank}(\boldsymbol{r'}) = n_c$. Let us express the sets of eigenvalues of $\boldsymbol{r}^\dagger \boldsymbol{r}$ and $\boldsymbol{r'r'}^\dagger$ as $\{R_1, R_2, \ldots, R_{n_c}, R_{n_c+1}\}$ and $\{R'_1, R'_2, \ldots, R'_{n_c}, R'_{n_c+1}\}$, respectively, and identify the $n_c + 1$th eigenvalues with zero (i.e., $R_{n_c+1} = R'_{n_c+1} = 0$). The set of eigenvalues of $\boldsymbol{tt}^\dagger$ is also expressed as $\{T_1, T_2, \ldots, T_{n_c}, T_{n_c+1}\}$. From (A.9) and (A.12), we obtain the following relations:

$$R_a + T_a = 1, \tag{A.13}$$

$$R'_a + T_a = 1, \tag{A.14}$$

26

where $a = 1, \ldots, n_c + 1$. As $R_{n_c+1} = R'_{n_c+1} = 0$, we conclude that the $n_c + 1$th transmission eigenvalue is equal to unity:

$$T_{n_c+1} = 1. \tag{A.15}$$

This indicates the presence of a right-going PCC that perfectly transmits an electron from the left lead to the right lead without backscattering even in the presence of disorder. In a manner similar to this, we can also show the presence of a left-going PCC in the K_+ valley in the absence of intervalleey scattering.

Since the numbers of right-going and left-going channels are imbalanced, the contribution to the dimensionless conductance g from the $K_\pm$ valley is anisotropic with respect to the transport direction. Let $g_R^\pm$ ($g_L^\pm$) be the contribution to g for the right-going (left-going) direction arising from the $K_\pm$ valley. Using the Landauer formula, g_R^- and g_L^- are expressed as

$$g_R^- = \mathrm{Tr}(\boldsymbol{t}\boldsymbol{t}^\dagger), \tag{A.16}$$

$$g_L^- = \mathrm{Tr}(\boldsymbol{t}'\boldsymbol{t}'^\dagger). \tag{A.17}$$

They can be rewritten as the summation over transmission eigenvalues as

$$g_R^- = \sum_{i=1}^{n_c+1} T_i = 1 + \sum_{i=1}^{n_c} T_i, \tag{A.18}$$

$$g_L^- = \sum_{i=1}^{n_c} T_i. \tag{A.19}$$

Due to the presence of the time-reversal symmetry, which relates the K_- and K_+ valleys, we can also show

$$g_R^+ = \sum_{i=1}^{n_c} T_i, \tag{A.20}$$

$$g_L^+ = \sum_{i=1}^{n_c+1} T_i = 1 + \sum_{i=1}^{n_c} T_i. \tag{A.21}$$

Combining the contributions from the two valleys, we find that the dimensionless conductance defined by $g \equiv g_R^+ + g_R^- = g_L^+ + g_L^-$ is expressed as

$$g = 1 + 2 \sum_{i=1}^{n_c} T_i. \tag{A.22}$$
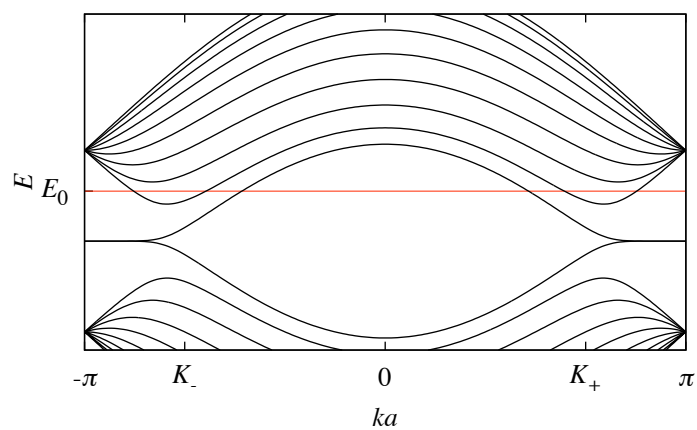
This clearly indicates that g is always greater than 1.

Figure A.2: The band structure of zigzag nanoribbon with M=10. There are two energy valleys at $ka = \pm 2\pi/3$. We refer to the valley at $ka = \pm 2\pi/3$ as $K_\pm$ valley. One excess right-going (left-going) channel exists in the K_- (K_+) valley.

Appendix B

Derivation of (2.47) and (2.48)

In this Appendix, we explain the derivation of (2.47),

$$t_{\mu\nu} = \sqrt{\frac{v_\mu}{v_\nu}} \{ \mathbf{U}(+)^{-1} \langle \mathrm{N}+1 | \mathbf{G} | 0 \rangle \mathbf{U}_{\mathrm{L}} (\mathbf{F}(+)^{-1} - \mathbf{F}(-)^{-1}) \mathbf{U}(+) \}_{\mu\nu}, \tag{B.1}$$

and that of (2.48),

$$r_{\mu\nu} = \sqrt{\frac{v_\mu}{v_\nu}} \{ \mathbf{U}(-)^{-1} [\langle 0 | \mathbf{G} | 0 \rangle \mathbf{U}_{\mathrm{L}} (\mathbf{F}(+)^{-1} - \mathbf{F}(-)^{-1}) - 1] \mathbf{U}(+) \}_{\mu\nu}. \tag{B.2}$$

First, we derive the transmission coefficient $t_{\mu\nu}$ from (2.45),

$$\mathbf{C}_{\mathrm{N}+1}^{\alpha}(+) = \langle \mathrm{N}+1 | \mathbf{G} | 0 \rangle \mathbf{U}_{\mathrm{L}} (\mathbf{F}(+)^{-1} - \mathbf{F}(-)^{-1}) \mathbf{C}_0^{\alpha}(+). \tag{B.3}$$

We expand $\mathbf{C}_{\mathrm{N}+1}^{\alpha}(+)$ and $\mathbf{C}_0^{\alpha}(+)$ as

$$\mathbf{C}_{\mathrm{N}+1}^{\alpha}(+) = \mathbf{U}(+)\mathbf{C}_{\alpha}'(+), \tag{B.4}$$

$$\mathbf{C}_0^{\alpha}(+) = \mathbf{U}(+)\mathbf{C}_{\alpha}(+), \tag{B.5}$$

where $\mathbf{C}_{\alpha}(+)$ and $\mathbf{C}_{\alpha}'(+)$ are arbitrary coefficients vectors, and substitute them to (B.3). Multiplying $\mathbf{U}(+)^{-1}$ from the left, we obtain

$$\mathbf{C}_{\alpha}'(+) = \mathbf{U}(+)^{-1} \langle \mathrm{N}+1 | \mathbf{G} | 0 \rangle \mathbf{U}_{\mathrm{L}} (\mathbf{F}(+)^{-1} - \mathbf{F}(-)^{-1}) \mathbf{U}(+) \mathbf{C}_{\alpha}(+). \tag{B.6}$$

The μth component of $\mathbf{C}_{\alpha}'(+)$ is written as

$$[\mathbf{C}_{\alpha}'(+)]_{\mu} = \sum_{\nu} [\mathbf{U}(+)^{-1} \langle \mathrm{N}+1 | \mathbf{G} | 0 \rangle \mathbf{U}_{\mathrm{L}} (\mathbf{F}(+)^{-1} - \mathbf{F}(-)^{-1}) \mathbf{U}(+)]_{\mu\nu} \cdot [\mathbf{C}_{\alpha}(+)]_{\nu}. \tag{B.7}$$

Noting that the current carried by $[\mathbf{C}_{\alpha}'(+)]_{\mu}$ is proportional to v_μ and that by $[\mathbf{C}_{\alpha}(+)]_{\nu}$ is proportional to v_ν, we can express the transmission coefficient from the incoming channel ν to the outgoing channel μ as

$$t_{\mu\nu} = \sqrt{\frac{v_\mu}{v_\nu}} \{ \mathbf{U}(+)^{-1} \langle \mathrm{N}+1 | \mathbf{G} | 0 \rangle \mathbf{U}_{\mathrm{L}} (\mathbf{F}(+)^{-1} - \mathbf{F}(-)^{-1}) \mathbf{U}(+) \}_{\mu\nu}. \tag{B.8}$$

Similarly, we derive the reflection coefficient $r_{\mu\nu}$ from (2.46),

$$\mathbf{C}_0^\alpha(-) = [\langle 0|\mathbf{G}|0\rangle \mathbf{U}_\mathrm{L}(\mathbf{F}(+)^{-1} - \mathbf{F}(-)^{-1}) - 1]\mathbf{C}_0^\alpha(+). \tag{B.9}$$

We expand $\mathbf{C}_0^\alpha(-)$ and $\mathbf{C}_0^\alpha(+)$ as

$$\mathbf{C}_0^\alpha(-) = \mathbf{U}(-)\mathbf{C}_\alpha(-), \tag{B.10}$$
$$\mathbf{C}_0^\alpha(+) = \mathbf{U}(+)\mathbf{C}_\alpha(+), \tag{B.11}$$

where $\mathbf{C}_\alpha(+)$ and $\mathbf{C}_\alpha(-)$ are arbitrary coefficients vectors, and substitute them to (B.9). Multiplying $\mathbf{U}(-)^{-1}$ from the left, we obtain

$$\mathbf{C}_\alpha(-) = \mathbf{U}(-)^{-1}[\langle 0|\mathbf{G}|0\rangle \mathbf{U}_\mathrm{L}(\mathbf{F}(+)^{-1} - \mathbf{F}(-)^{-1}) - 1]\mathbf{U}(+)\mathbf{C}_\alpha(+). \tag{B.12}$$

The μth component of $\mathbf{C}_\alpha(-)$ is written as

$$[\mathbf{C}_\alpha(-)]_\mu = \sum_\nu [\mathbf{U}(-)^{-1}\{\langle 0|\mathbf{G}|0\rangle \mathbf{U}_\mathrm{L}(\mathbf{F}(+)^{-1} - \mathbf{F}(-)^{-1}) - 1\}\mathbf{U}(+)]_{\mu\nu} \cdot [\mathbf{C}_\alpha(+)]_\nu. \tag{B.13}$$

The reflection coefficient from the incoming channel ν to the outgoing channel μ can be expressed as

$$r_{\mu\nu} = \sqrt{\frac{v_\mu}{v_\nu}}\{\mathbf{U}(-)^{-1}[\langle 0|\mathbf{G}|0\rangle \mathbf{U}_\mathrm{L}(\mathbf{F}(+)^{-1} - \mathbf{F}(-)^{-1}) - 1]\mathbf{U}(+)\}_{\mu\nu}. \tag{B.14}$$

Appendix C

Expression of v_μ

We derive an expression of the velocity v_μ needed to obtain the scattering matrices (2.47) and (2.48). We assume that the velocity is proportional to the expectation value of probability current in the y direction. The current operator for the jth unit cell is

$$\hat{j}_y = it \sum_{l=1}^{\mathrm{M}} \{|j,l;\beta\rangle\langle j,l;\alpha| - |j,l;\alpha\rangle\langle j,l;\beta|\}. \tag{C.1}$$

The eigenfuncion of μth channel is represented as

$$|\Psi_\mu\rangle = \sum_j \sum_l \left[\lambda_\mu(\pm)^j C_{\mu,l}^\alpha(\pm)|j,l;\alpha\rangle + \lambda_\mu(\pm)^j C_{\mu,l}^\beta(\pm)|j,l;\beta\rangle \right]. \tag{C.2}$$

The corresponding expectation value of current is

$$\langle\Psi_\mu|\hat{j}_y|\Psi_\mu\rangle = it \sum_{l=1}^{\mathrm{M}} \left[\lambda_\mu^*(\pm)^j C_{\mu,l}^{\beta*} \lambda_\mu(\pm)^j C_{\mu,l}^\alpha - \lambda_\mu^*(\pm)^j C_{\mu,l}^{\alpha*} \lambda_\mu(\pm)^j C_{\mu,l}^\beta \right] \tag{C.3}$$

$$= it|\lambda_\mu(\pm)|^{2j} \sum_{l=1}^{\mathrm{M}} \left[C_{\mu,l}^{\beta*} C_{\mu,l}^\alpha - C_{\mu,l}^{\alpha*} C_{\mu,l}^\beta \right] \tag{C.4}$$

$$= 2t|\lambda_\mu(\pm)|^{2j} \sum_{l=1}^{\mathrm{M}} \mathrm{Im}\left\{ C_{\mu,l}^{\alpha*} C_{\mu,l}^\beta \right\}. \tag{C.5}$$

Consequently, the velocity for the μth channel is given by

$$v_\mu(\pm) \propto \sum_{l=1}^{\mathrm{M}} \mathrm{Im}\left\{ C_{\mu,l}^{\alpha*} C_{\mu,l}^\beta \right\}. \tag{C.6}$$

where

$$\mathbf{C}_\mu^\beta(\pm) = (\lambda_\mu(\pm) + 1)(E\mathbf{I} - \mathbf{H}^\beta)^{-1}\mathbf{V}\mathbf{C}_\mu^\alpha(\pm). \tag{C.7}$$

Appendix D

Boltzmann Transport Theory

In this Appendix, we explain the derivation of (3.1). The analytical expression (3.1) is derived by applying the Boltzmann transport equation to a simple model for zigzag nanoribbons. We consider the case where the K_- (K_+) valley has n_c+1 right-going (left-going) channels and n_c left-going (right-going) channels. We symbolically represents the right-going and left-going channels as R and L, and the K_- and K_+ valleys as $-$ and $+$, respectively. Let $\varepsilon_{\mathrm{R}nk}^{\pm}$ ($\varepsilon_{\mathrm{L}nk}^{\pm}$) be the energy of an electron state with wave number k in the nth right-going (left-going) channel. We introduce the distribution function g_{Xnk}^{z} for electrons, where $z = +, -$, and $X = \mathrm{R}, \mathrm{L}$. The group velocity v_{Xnk}^{z} is given by $v_{Xnk}^{z} = \partial\varepsilon_{Xnk}^{z}/\partial k$. For simplicity, we set $v_{\mathrm{R}nk}^{z} \equiv v_{\mathrm{R}}$ and $v_{\mathrm{L}nk}^{z} \equiv v_{\mathrm{L}}$ with $v = v_{\mathrm{R}} = -v_{\mathrm{L}}$. Let us consider a zigzag nanoribbon placed along x direction in the presence of an electric field $E(x)$ in the negative x direction. The distribution function obeys the Boltzmann equation for steady states:

$$v_X\frac{\partial g_{Xnk}^{z}}{\partial x} + eE(x)\frac{\partial g_{Xnk}^{z}}{\partial k} = \sum_{z',X',n',k'} W_{Xnk,X'n'k'}^{z,z'}(g_{X'n'k'}^{z'} - g_{Xnk}^{z}), \tag{D.1}$$

where $W_{Xnk,X'n'k'}^{z,z'}$ represents the scattering probability between the state with $\{X'n'k'z'\}$ and that with $\{Xnkz\}$. This is expressed as

$$W_{Xnk,X'n'k'}^{z,z'} = 2\pi M_{Xnk,X'n'k'}^{z,z'}\delta(\varepsilon_{X'n'k'}^{z'} - \varepsilon_{Xnk}^{z}) \tag{D.2}$$

with

$$M_{Xnk,X'n'k'}^{z,z'} = \langle|U_{Xnk,X'n'k'}^{z,z'}|^2\rangle, \tag{D.3}$$

where $U_{Xnk,X'n'k'}^{z,z'}$ is the matrix element of impurity potential, and $\langle\cdots\rangle$ represents the ensemble average over impurity configurations. We assume that the scattering probability depends on only the valley indices z and z', and does not depend on details of initial and final states. Hence, $M_{Xnk,X'n'k'}^{\pm,\pm} = M$ and $M_{Xnk,X'n'k'}^{\pm,\mp} = M'$, where M and M' respectively denote the strength of intravalley scattering and intervalley scattering.

Suppose that electrons are accelerated by an electric field only in the finite region of $L/2 > x > -L/2$. Accordingly, we assume that $E(x) = E$ for $L/2 > x > -L/2$ and $E(x) = 0$ otherwise. We express the distribution function as

$$g_{Xnk}^{z} = f(\varepsilon_{Xnk}^{z}) - \mathrm{sign}(v_X)eE(x)l_{Xnk}^{z}(x)\frac{\partial f}{\partial \varepsilon}(\varepsilon_{Xnk}^{z}), \tag{D.4}$$

32

where $f(\varepsilon)$ is the Fermi–Dirac function and $l^z_{Xnk}(x)$ is the mean free path. The Boltzmann conductivity σ is obtained as

$$\sigma(x) = \frac{e^2}{L} \sum_{zXnk} |v_X| l^z_{Xnk}(x) \left[-\frac{\partial f}{\partial \varepsilon}(\varepsilon^z_{Xnk}) \right]$$

$$= \frac{e^2}{2\pi} \left(\sum_{n=1}^{n_c+1} l^-_{Rn}(x) + \sum_{n=1}^{n_c} l^-_{Ln}(x) + \sum_{n=1}^{n_c} l^+_{Rn}(x) + \sum_{n=1}^{n_c+1} l^+_{Ln}(x) \right), \tag{D.5}$$

where k is dropped in $l^z_{Xnk}(x)$ since we are interested in electron states near the Fermi level. According to the assumption stated above, $l^z_{Xn}(x)$ is also independent of n. Thus, (D.5) is reduced to

$$\sigma(x) = \frac{e^2}{2\pi} \left\{ (n_c + 1)l^-_R(x) + n_c l^-_L(x) + n_c l^+_R(x) + (n_c + 1)l^+_L(x) \right\}. \tag{D.6}$$

We assume that electrons incoming from the left (right) lead are described by the equilibrium distribution. Consequently, the mean free path $l^z_X(x)$ satisfies the boundary condition of

$$l^-_R(-L/2) = l^+_R(-L/2) = 0, \tag{D.7}$$
$$l^-_L(L/2) = l^+_L(L/2) = 0. \tag{D.8}$$

From the symmetry of the band structure, we can safely assume

$$l(x) \equiv l^-_R(x) = l^+_L(-x), \tag{D.9}$$
$$l'(x) \equiv l^+_R(x) = l^-_L(-x). \tag{D.10}$$

Substituting (D.4) to (D.1), we obtain a pair of equations for $l(x)$ and $l'(x)$ as

$$-\frac{\partial l(x)}{\partial x} + 1 = [n_c\kappa + (2n_c + 1)\kappa']l(x) + n_c\kappa l'(-x)$$
$$+ (n_c + 1)\kappa' l(-x) - n_c\kappa' l'(x), \tag{D.11}$$
$$-\frac{\partial l'(x)}{\partial x} + 1 = [(n_c + 1)\kappa + (2n_c + 1)\kappa']l'(x) + (n_c + 1)\kappa l(-x)$$
$$+ n_c\kappa' l'(-x) - (n_c + 1)\kappa' l(x), \tag{D.12}$$

where

$$\kappa = \frac{LM}{v^2}, \tag{D.13}$$

$$\kappa' = \frac{LM'}{v^2}. \tag{D.14}$$

Solving these equations under the boundary condition of (D.7) and (D.8), we obtain

$$l(x) = x + \frac{L}{2} + \frac{L}{\Sigma} \left\{ -(\kappa - \kappa')[c(x) - c_L] + \frac{(\kappa^2 - \kappa'^2)}{\sqrt{\alpha}}[d(x) - d_L] \right.$$
$$\left. -2(2n_c + 1)^2(\kappa + \kappa')\kappa' c_L \left(x + \frac{L}{2} \right) \right\}, \tag{D.15}$$

and

$$l'(x) = x + \frac{L}{2} + \frac{L}{\Sigma} \left\{ (\kappa - \kappa')[c(x) - c_L] + \frac{(\kappa^2 - \kappa'^2)}{\sqrt{\alpha}}[d(x) - d_L] \right.$$

$$\left. -2(2n_c + 1)^2(\kappa + \kappa')\kappa' c_L \left(x + \frac{L}{2} \right) \right\}, \tag{D.16}$$

where $\alpha = (\kappa + \kappa')[\kappa + (8N^2 + 8N + 1)\kappa']$ and

$$c(x) = \frac{(2n_c + 1)(\kappa + \kappa')}{\sqrt{\alpha}} \cosh(\sqrt{\alpha}x) - \sinh(\sqrt{\alpha}x), \tag{D.17}$$

$$d(x) = -\frac{(2n_c + 1)(\kappa + \kappa')}{\sqrt{\alpha}} \sinh(\sqrt{\alpha}x) + \cosh(\sqrt{\alpha}x). \tag{D.18}$$

The constants are defined as $c_L = c(-L/2)$, $d_L = d(L/2)$, and

$$\Sigma = 4(2n_c + 1)\kappa' \left[1 + \frac{1}{2}(2n_c + 1)(\kappa + \kappa')L \right] c_L + 2\frac{\kappa^2 - \kappa'^2}{\sqrt{\alpha}} d_L. \tag{D.19}$$

In terms of $l(x)$ and $l'(x)$, the Boltzmann conductivity is expressed as

$$\sigma(x) = \frac{e^2}{2\pi} \{ (n_c + 1)[l(x) + l(-x)] + n_c[l'(x) + l'(-x)] \}. \tag{D.20}$$

Substituting (D.15) and (D.16) to (D.20), we find that $\sigma(x)$ is independent of x and is given by

$$\sigma = \frac{e^2 L}{2\pi} \frac{2\alpha c_L}{(\kappa + \kappa')\Sigma}. \tag{D.21}$$

We finally obtain the dimensionless conductance as

$$g_{\mathrm{B}} = \frac{2\pi}{e^2} \frac{\sigma}{L} = \frac{[\kappa + (8n_c^2 + 8n_c + 1)\kappa'] c_L}{(2n_c + 1)\kappa' [2 + (2n_c + 1)(\kappa + \kappa')L] c_L + \frac{\kappa^2 - \kappa'^2}{\sqrt{\alpha}} d_L}. \tag{D.22}$$

Acknowledgment

I would like to express my deep gratitude to Professor Yositake Takane for his tremendous support. The dissertation would not have been completed without his support.

I also would like to thank the colleagues of Mesoscopic Physics Theory Group, AdSM, Hiroshima Univ.

Finally, I am grateful to my family for constant encouragement.

References

[1] H. W. Kroto, J. R. Heath, S. C. O'Brien, R. F. Curl, and R.E. Smalley, Nature **318**, 162 (1985).

[2] S. Iijima, Nature **354**, 56 (1991).

[3] K. S. Novoselov, A. K. Geim, S. V. Morozov, D. Jiang, Y. Zhang, S. V. Dubons, I. V. Grigoriva, and A. A. Firsov, Science **306**, 666 (2004).

[4] K. S. Novoselov, D. Jiang, F. Schedin, T. J. Booth, V. V. Khotokevich, S. V. Morozov, and A. K. Geim, PNAS. **102**, 10451 (2005).

[5] See, for a review, A. H. Castro Neto, F. Guinea, N. M. R. Peres, K. S. Novoselov, and A. K. Geim, Rev. Mod. Phys. **81**, 109 (2009).

[6] Y. Zhang, Y.-W. Tan, H. L. Stormer, P. Kim, Nature **438**, 201 (2005).

[7] M. Fujita, K. Wakabayashi, K. Nakada, and K. Kusakabe, J. Phys. Soc. Jpn. **65**, 1920 (1996).

[8] Y. Kobayashi, K. Fukui, T. Enoki, K. Kusakabe, and Y. Kaburagi, Phys. Rev. B **71**, 193406 (2005).

[9] Y. Niimi, T. Matsui, H. Kambara, K. Tagami, M. Tsukada, and H. Fukuyama, Phys. Rev. B **73**, 085421 (2006).

[10] K. Wakabayashi, M. Fujita, H. Ajiki, and M. Sigrist, Phys. Rev. B **59**, 8271 (1999).

[11] K. Wakabayashi and M. Sigrist, Phys. Rev. Lett. **84** 3390 (2000).

[12] K. Wakabayashi, Phys. Rev. B **64**, 125428 (2001).

[13] M. Büttiker, Phys. Rev. B **38**, 9375 (1988).

[14] T. Ando and T. Nakanishi, J. Phys. Soc. Jpn. **67**, 1704 (1998).

[15] T. Ando, T. Nakanishi, and R. Saito, J. Phys. Soc. Jpn. **67**, 2857 (1998).

[16] T. Nakanishi and T. Ando, J. Phys. Soc. Jpn. **68**, 561 (1999).

[17] T. Ando and H. Suzuura, J. Phys. Soc. Jpn. **71**, 2753 (2002).

[18] T. Ando, J. Phys. Soc. Jpn. **73**, 1273 (2004).

[19] C. L. Kane and E. J. Mele, Phys. Rev. Lett. **95**, 146802 (2005).

[20] C. L. Kane and E. J. Mele, Phys. Rev. Lett. **95**, 226801 (2005).

[21] M. Onoda and N. Nagaosa, Phys. Rev. Lett. **95**, 106601 (2005).

[22] B. A. Bernevig and S.-C. Zhang, Phys. Rev. Lett. **96**, 106802 (2006).

[23] X.-L. Qi, Y.-S. Wu, and S.-C. Zhang, Phys. Rev. B **74**, 045125 (2006).

[24] S. Murakami, Phys. Rev. Lett. **97**, 236805 (2006).

[25] Y. Ran, Y. Zhang, and A. Vishwanath, Nat. Phys. **5**, 298 (2009).

[26] K.-I. Imura, Y. Takane, and A. Tanaka, Phys. Rev. B **84**, 035443 (2011).

[27] Z. Ringel, Y. E. Kraus, and A. Stern, Phys. Rev. B **86**, 045102 (2012).

[28] Y. Yoshimura, A. Matsumoto, Y. Takane, and K.-I. Imura, Phys. Rev. B **88**, 045408 (2013).

[29] K. Kobayashi, T. Ohtsuki, and K.-I. Imura, Phys. Rev. Lett. **110**, 236803 (2013).

[30] Y. Zhang and A. Vishwanath, Phys. Rev. Lett. **105**, 206601 (2010).

[31] R. Egger, A. Zazunov, and A. Levy Yeyati, Phys. Rev. Lett. **105**, 136403 (2010).

[32] J. H. Bardarson, P. W. Brouwer, and J. E. Moore, Phys. Rev. Lett. **105**, 156803 (2010).

[33] K. Wakabayashi, Y. Takane, and M. Sigrist, Phys. Rev. Lett. **99**, 036601 (2007).

[34] K. Wakabayashi, Y. Takane, M. Yamamoto, and M. Sigrist, Carbon **47**, 124 (2009).

[35] K. Wakabayashi, Y. Takane, M. Yamamoto, and M. Sigrist, New J. Phys. **11**, 095016 (2009).

[36] C. Barnes, B. L. Johnson, and G. Kirczenow, Phys. Rev. Lett. **70**, 1159 (1993).

[37] C. Barnes, B. L. Johnson, and G. Kirczenow, Can. J. Phys. **72**, 559 (1994).

[38] K. Hirose, T. Ohtsuki, and K. Slevin, Physica E **40**, 1677 (2008).

[39] M. Yamamoto, Y. Takane, and K. Wakabayashi, Phys. Rev. B **79**, 125421 (2009).

[40] J. Wurm, M. Wimmer, and K. Richter, Phys. Rev. B **85**, 245418 (2012).

[41] Y. Takane, J. Phys. Soc. Jpn. **79**, 024711 (2010).

[42] Y. Takane, J. Phys. Soc. Jpn. **79**, 104706 (2010).

[43] Y. Shimomura, and Y. Takane, J. Phys. Soc. Jpn. **85**, 014704 (2016).

[44] J. Baringhaus, M. Ruan, F. Edler, A. Tejeda, M. Sicot, A. Taleb-Ibrahimi, A.-P. Li, Z. Jiang, E. H. Conrad, C. Berger, C. Tegenkamp, and W. A. de Heer, Nature **506**, 349 (2014).

[45] Y. Imry, *Introduction to Mesoscopic Physics* (Oxford University Press, Oxford, 1999) Chap. 5.

[46] T. Ando, Phys. Rev. B **44**, 8017 (1991).

[47] Y. Takane and K. Wakabayashi, J. Phys. Soc. Jpn. **76**, 053701 (2007).

公表論文

(1) Dephasing-Induced Stabilization of a Perfectly Conducting Channel in Disordered Graphene Nanoribbons with Zigzag Edges
Yuji Shimomura, and Yositake Takane
Journal of the Physical Society of Japan, **85**, 014704, 1-6 (2016).

Dephasing-Induced Stabilization of a Perfectly Conducting Channel in Disordered Graphene Nanoribbons with Zigzag Edges

Yuji Shimomura and Yositake Takane

Department of Quantum Matter, Graduate School of Advanced Sciences of Matter, Hiroshima University,
Higashihiroshima, Hiroshima 739-8530, Japan

Electron transport in a disordered graphene nanoribbon with zigzag edges is crucially affected by a perfectly conducting channel (PCC), which is stabilized if intervalley scattering is ignorable. In the presence of such a PCC, the dimensionless conductance g of the system decreases to the quantized value of $g = 1$ with increasing system length L. In the realistic case where intervalley scattering is weak but not ignorable, the PCC is gradually destabilized with increasing L, and g eventually decays to zero owing to the onset of Anderson localization. Here, we show that such destabilization of the PCC can be relaxed by pure dephasing. We numerically calculate g in the presence of long-range impurities, which induce weak intervalley scattering, taking the dephasing effect into account. It is demonstrated that, under sufficient dephasing, the decay of g in the regime of $g \lesssim 1$ is strongly suppressed and the quasi-quantization of g (i.e., $g \sim 1$) can be observed in a wide region of L.

1. Introduction

A perfectly conducting channel (PCC) designates a conducting channel that perfectly transmits an electron from one end to the other in spite of the presence of disorder. The most well-known example is a one-dimensional (1D) chiral edge channel of two-dimensional (2D) quantum Hall insulators.[1] This 1D edge channel needs a strong magnetic field for its stabilization. So far, PCCs have been shown to appear in various carbon nanostructures and topological insulators under no external field.

Ando and co-workers[2–6] showed that a PCC appears in disordered carbon nanotubes (CNTs) with a gapless spectrum in the absence of intervalley scattering. The requirement of no intervalley scattering is explained as follows. A CNT possesses two energy valleys in the reciprocal space, and the effective Hamiltonian describing each valley is invariant under a time-reversal operation $\mathcal{T}$ that satisfies $\mathcal{T}^2 = -1$; the subsystems corresponding to each valley have the symplectic symmetry. Furthermore, the number of conducting channels in each valley is always odd regardless of the Fermi level. The existence of a PCC is guaranteed by the symplectic symmetry combined with an odd number of conducting channels. If intervalley scattering occurs and the two valleys are coupled as its consequence, these two conditions break down and hence the PCC disappears. In CNTs, an impurity potential with a range larger than the lattice constant induces only very weak intervalley scattering since the two energy valleys are well separated in the reciprocal space. Thus, we expect that the above two conditions are approximately satisfied if a CNT contains only such long-range impurities (LRIs), leading to the appearance of a PCC. Clearly, there is no PCC in the presence of short-range impurities (SRIs).

A 1D helical edge channel of 2D quantum spin-Hall insulators[7–12] can be regarded as a typical example of a PCC in topological insulators. Its protection mechanism against disorder is essentially equivalent to that of a PCC in CNTs. However, as quantum spin-Hall insulators typically possess only a single valley, the disturbance due to intervalley scattering is irrelevant in this case. A similar PCC is stabilized in three-dimensional (3D) weak topological insulators in various situations.[13–17] In 3D strong topological insulators, a PCC can appear only when a π magnetic flux penetrates the bulk of a sample without touching surface states.[18–20]

Wakabayashi and co-workers[21–23] showed that disordered graphene nanoribbons with zigzag edges accommodate a PCC, on which our interest is focused in this paper. Hereafter, a graphene nanoribbon with zigzag edges is simply referred to as a zigzag nanoribbon. As in the case of CNTs, zigzag nanoribbons possess two energy valleys in the reciprocal space. The important feature of zigzag nanoribbons is that conducting channels are imbalanced between the two propagating directions in each valley. That is, the number of conducting channels going in one direction is one greater or smaller than that going in the other direction, regardless of the Fermi level. This directly results in the stabilization of a PCC[24–26] if intervalley scattering is ignorable. Thus, we expect the appearance of a PCC in zigzag nanoribbons containing only LRIs. In contrast to the case of CNTs, the symmetry of the system plays no role in this case. It has been shown that disordered graphene nanoribbons with armchair edges also accommodate a similar PCC.[27,28]

If a PCC stably exists, the dimensionless conductance g of the system decreases to the quantized value of $g = 1$ with increasing system length L. In CNTs and graphene nanoribbons, we expect the appearance of a PCC only when the disorder of the system is long-range, as noted above. Indeed, if the spatial range of disorder is sufficiently large, the strength of intervalley scattering becomes very weak. However, in actual situations, it is impossible to completely suppress intervalley scattering. The effect of residual intervalley scattering gradually manifests itself with increasing L and eventually destabilizes a PCC. In this case, the behavior of g may not be distinguishable from that in an ordinary system with no PCC.

The effect of inelastic scattering may be another important obstacle to the observation of a PCC. Inelastic scattering caused by electron–electron and/or electron–phonon interactions affects low-energy electrons mainly through energy relaxation and dephasing. At low temperatures, pure dephas-

ing most significantly influences the transport properties. Indeed, dephasing directly destabilizes a PCC in CNTs as well as topological insulators since it weakens the underlying symplectic symmetry of the system, except for the case with only a single channel, where it becomes a PCC and is relatively robust against dephasing.[5,6] Contrastingly, a PCC in zigzag nanoribbons relies on no symmetry of the system, so dephasing does not necessarily disturb it. Previous studies[29,30] based on the Boltzmann transport equation indicate that a PCC remains even in the incoherent limit. However, it is not clear how the behavior of a PCC changes with the reduction of phase coherence.

In this paper, the effect of pure dephasing on a PCC in zigzag nanoribbons is studied by numerical simulations of the dimensionless conductance. We show that dephasing does not disturb a PCC but rather relaxes its destabilization due to weak intervalley scattering. To clarify the dephasing effect on the PCC we numerically calculate the average dimensionless conductance $\langle g \rangle$ in zigzag nanoribbons with LRIs at zero temperature, taking account of dephasing within the model presented in Ref. 5. In the case without dephasing, we observe that $\langle g \rangle$ rapidly decreases to the quantized value of $\langle g \rangle = 1$ with increasing L, implying the presence of a PCC, and then it exponentially decays below the quantized value, reflecting the destabilization of the PCC. However, in the presence of sufficiently strong dephasing, we observe that the exponential decay of $\langle g \rangle$ in the regime of $\langle g \rangle \lesssim 1$ is significantly relaxed owing to the suppression of Anderson localization. Consequently, the quasi-quantization of $\langle g \rangle$ (i.e., $\langle g \rangle \sim 1$) can be observed in a wide region of L. This result should encourage experimental attempts to detect a PCC in zigzag nanoribbons.[31]

In the next section, we present the tight-binding model for a zigzag nanoribbon. We assume that every impurity potential distributed over the system is described by a Gaussian form of spatial range d. This corresponds to an LRI (SRI) when d is larger (smaller) than the lattice constant a. We compute the dimensionless conductance using the Landauer formula by numerically determining the scattering matrix for the system. The model for describing the pure dephasing is also introduced. In Sect. 3, the numerical results of the average dimensionless conductance are presented for the case with LRIs and that with SRIs. We observe that the destabilization of the PCC can be relaxed by the dephasing in the former case. In Sect. 4, the numerical results of the previous section are compared with an analytical expression for the dimensionless conductance derived from the Boltzmann transport equation.[29] We see that the numerical result in the case with strong dephasing is accurately fitted by the analytical result, implying that our model appropriately describes the effect of dephasing. The last section is devoted to summary and conclusion. Preliminary results of this work have been briefly reported in Ref. 32.

2. Model and Formulation

We consider a zigzag nanoribbon consisting of M zigzag lines placed along the x-axis (see Fig. 1). Its band structure is shown in Fig. 2 in the case of $M = 30$. One can see that in the left (right) valley, the number of right-going (left-going) channels is one greater than that of left-going (right-going) channels regardless of the location of the Fermi level. This
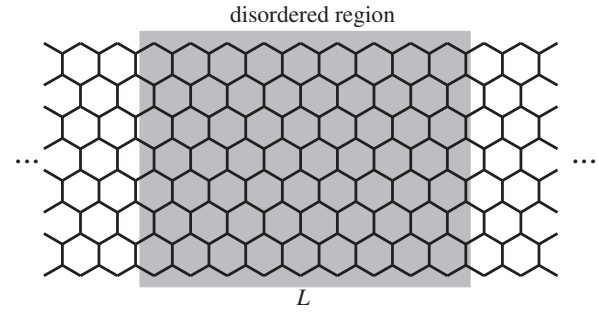

Fig. 1. Illustration of zigzag nanoribbon. The gray area of length L represents the disordered region with randomly distributed impurities. The left and right regions without disorder are regarded as perfect leads.
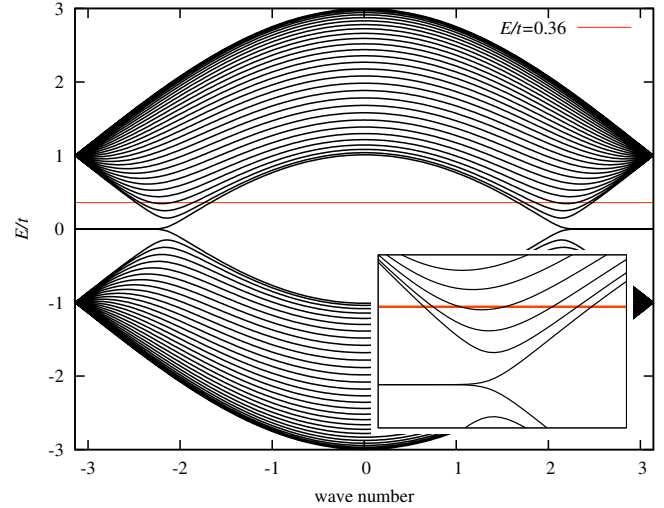

Fig. 2. (Color online) Band structure of zigzag nanoribbon with $M = 30$. The inset represents the magnification of subbands in the left valley.

indicates that a right-going PCC appears in the left valley while a left-going PCC appears in the right valley.[21]

2.1 Hamiltonian

We describe π electrons in zigzag nanoribbons by using the nearest-neighbor tight-binding model

$$H = -t \sum_{\text{n.n.}} |i\rangle\langle j| + \sum_i V(\mathbf{r}_i)|i\rangle\langle i|, \tag{1}$$

where t is the hopping integral between neighboring sites, $|i\rangle$ is the π orbital on site i, and $V(\mathbf{r}_i)$ is the impurity potential with $\mathbf{r}_i$ being the position of site i. We randomly distribute impurities in a region of length L (see Fig. 1). We assume that each site is occupied by an impurity with probability P and the potential of each impurity is characterized by a Gaussian form of spatial range d. Hence, $V(\mathbf{r}_i)$ is represented as

$$V(\mathbf{r}_i) = \sum_j u(\mathbf{r}_j) \exp\left(-\frac{|\mathbf{r}_i - \mathbf{r}_j|^2}{d^2}\right), \tag{2}$$

where $u(\mathbf{r}_j)$ is the strength of an impurity at site j. We assume that $u(\mathbf{r}_j)$ is uniformly distributed within $|u| < u_{\text{max}}/2$. Note that the degree of disorder is determined by d, P, and u_{max}.

2.2 Scattering matrix

The electron transport property of a zigzag nanoribbon

is determined by the scattering matrix, which consists of transmission matrices t and t' and reflection matrices r and r', where t and r (t' and r') describe the scattering of an electron incoming from the left (right). Let N_c be the number of conducting channels for a given value of the Fermi energy E. The dimensions of the transmission and reflection matrices are $N_c \times N_c$. In calculating the scattering matrix, we consider that the left and right of the disordered region serve as perfect leads of semi-infinite length without disorder. The transmission and reflection matrices can be obtained by using a recursive Green's function method. The dimensionless conductance at zero temperature is obtained using the Landauer formula $g(E) = \mathrm{tr}(t^\dagger t)$, where $t^\dagger$ is the Hermitian conjugate of t.

2.3 Dephasing

Generally speaking, dephasing suppresses quantum effects, particularly quantum interference effects, and tends to reveal classical behaviors of electrons in some cases.

In order to incorporate this effect into our model, we hypothetically decompose the disordered region into N_s segments of equal length L_ϕ, as shown in Fig. 3, and assume that the phase coherence of electrons is lost across adjacent segments while in each segment the phase coherence is completely preserved.[5] Hence, L_ϕ can be regarded as the phase coherence length. We require the continuity of the charge current, instead of the continuity of a wave function, in each channel between adjacent segments. With this procedure, the phase coherence of electrons completely breaks across adjacent segments. Let us express the transmission and reflection matrices for the nth segment as t_n, r_n, t'_n, and r'_n. In terms of them, the transmission probability matrix $\mathcal{T}_n$ ($\mathcal{T}_{\bar{n}}$) and the reflection probability matrix $\mathcal{R}_n$ ($\mathcal{R}_{\bar{n}}$) for an electron incoming from the left (right) are defined as

$$[\mathcal{T}_n]_{\alpha\beta} = |[t_n]_{\alpha\beta}|^2,$$

$$[\mathcal{R}_n]_{\alpha\beta} = |[r_n]_{\alpha\beta}|^2,$$

$$[\mathcal{T}_{\bar{n}}]_{\alpha\beta} = |[t'_n]_{\alpha\beta}|^2,$$

$$[\mathcal{R}_{\bar{n}}]_{\alpha\beta} = |[r'_n]_{\alpha\beta}|^2. \tag{3}$$

For the system constituted by combining the first, second,$\cdots$, nth segments in series, we define $\tilde{\mathcal{T}}_n$ ($\tilde{\mathcal{T}}_{\bar{n}}$) and $\tilde{\mathcal{R}}_n$ ($\tilde{\mathcal{R}}_{\bar{n}}$) as the transmission and reflection probability matrices for an electron incoming from the left (right), respectively. The continuity of the charge current ensures that they obey the following recursive relation.[5]

$$\begin{pmatrix} \tilde{\mathcal{R}}_{n+1} & \tilde{\mathcal{T}}_{\overline{n+1}} \\ \tilde{\mathcal{T}}_{n+1} & \tilde{\mathcal{R}}_{\overline{n+1}} \end{pmatrix} = \begin{pmatrix} \tilde{\mathcal{R}}_n & 0 \\ 0 & \mathcal{R}_{\overline{n+1}} \end{pmatrix}$$
$$+ \begin{pmatrix} 0 & \tilde{\mathcal{T}}_{\bar{n}} \\ \mathcal{T}_{n+1} & 0 \end{pmatrix} \begin{pmatrix} 1 & -\tilde{\mathcal{R}}_{\bar{n}} \\ -\mathcal{R}_{n+1} & 1 \end{pmatrix}^{-1} \begin{pmatrix} \tilde{\mathcal{T}}_n & 0 \\ 0 & \mathcal{T}_{\overline{n+1}} \end{pmatrix}, \tag{4}$$

with $\tilde{\mathcal{T}}_1 = \mathcal{T}_1$, $\tilde{\mathcal{R}}_1 = \mathcal{R}_1$, $\tilde{\mathcal{T}}_{\bar{1}} = \mathcal{T}_{\bar{1}}$, and $\tilde{\mathcal{R}}_{\bar{1}} = \mathcal{R}_{\bar{1}}$. The dimensionless conductance is given by

$$g = \sum_{\alpha,\beta=1}^{N_c} [\tilde{\mathcal{T}}_{N_s}]_{\beta\alpha} \tag{5}$$

in the presence of dephasing.

3. Numerical Results

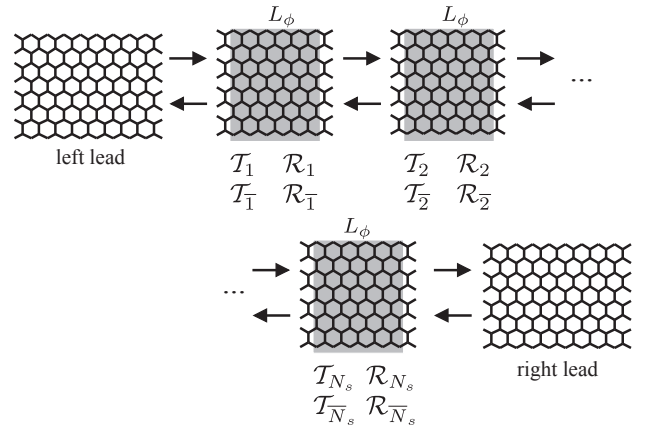We separately consider the case with LRIs and that with

Fig. 3. Hypothetical decomposition of the disordered region of length L into N_s segments of equal length L_ϕ. We assume that the phase coherence of electrons is lost across adjacent segments.
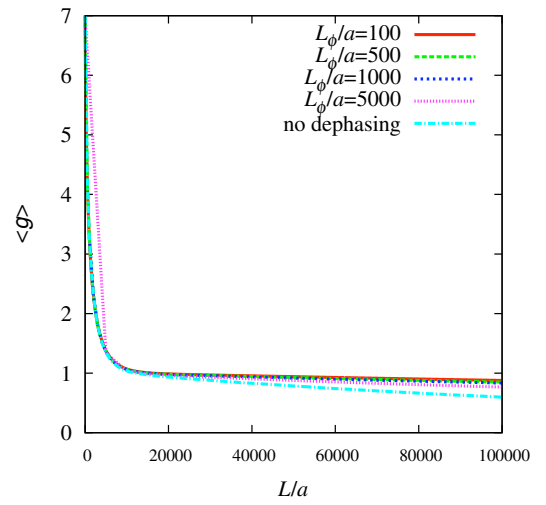

Fig. 4. (Color online) Average dimensionless conductance $\langle g \rangle$ in the LRI case for several values of L_ϕ/a.

SRIs. In the former case, we expect that a PCC appears as intervalley scattering is sufficiently weak, while strong intervalley scattering forbids its appearance in the latter case. These two cases are realized by appropriately choosing d. With $P = 0.1$, we set $d/a = 1.5$ and $u_{\max}/t = 0.1$ in the LRI case, and $d/a = 0.05$ and $u_{\max}/t = 1.0$ in the SRI case. We fix $M = 30$ and $E/t = 0.36$, resulting in $N_c = 7$, in the following calculations.

Let us consider the LRI case. We use 2000 samples with different impurity configurations to calculate the average dimensionless conductance $\langle g \rangle$. Figure 4 shows that $\langle g \rangle$ rapidly decreases to 1 with increasing L/a and then the decrease becomes very slow once it decays below 1, indicating the presence of a PCC. In the regime of $\langle g \rangle \lesssim 1$, the decay of $\langle g \rangle$ becomes slower as L_ϕ becomes smaller. This can be explained by considering that the decay of $\langle g \rangle$ below 1 is accelerated by Anderson localization. The effect of Anderson localization is suppressed by dephasing and hence the decay of $\langle g \rangle$ is also suppressed with decreasing L_ϕ. This indicates that dephasing indirectly stabilizes a PCC, although dephasing itself does not weaken intervalley scattering. We observe the quasi-quantization of $\langle g \rangle$ (i.e., $\langle g \rangle \sim 1$) in a wide
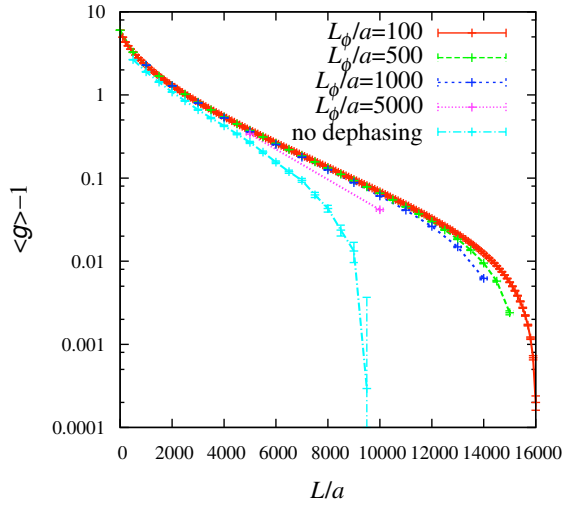
Fig. 5. (Color online) Semilog plot of $\langle g \rangle - 1$ in the case of LRI. In a certain region of L/a, $\langle g \rangle$ decreases exponentially toward 1 as a function of L/a.

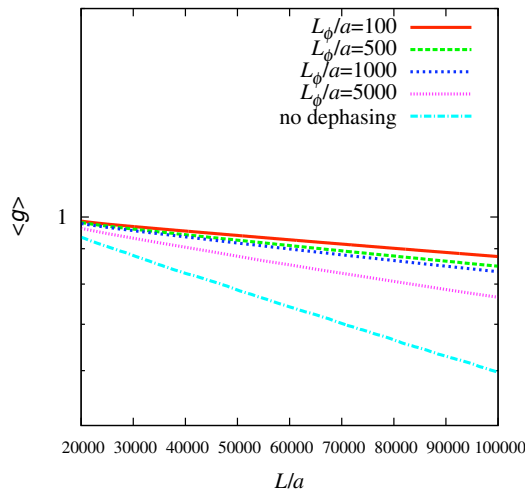**Fig. 7.** (Color online) Average dimensionless conductance $\langle g \rangle$ in the SRI case.

Fig. 6. (Color online) Semilog plot of $\langle g \rangle$ in the LRI case in the regime of $\langle g \rangle < 1$. $\langle g \rangle$ decays exponentially as a function of L/a even in the presence of dephasing.

Fig. 8. (Color online) Log–log plot of $\langle g \rangle$ in the SRI case with dephasing. $\langle g \rangle$ asymptotically becomes inversely proportional to L/a.

region of L/a when L_ϕ is sufficiently small. Figure 5 shows a semilog plot of $\langle g \rangle - 1$. Error bars at each data point represent $(\mathrm{var}\{g\}/N_{\mathrm{sam}})^{1/2}$, where $\mathrm{var}\{g\} = \langle g^2 \rangle - \langle g \rangle^2$ and N_{sam} is the number of samples used to calculate the average. We find that $\langle g \rangle$ decreases exponentially toward 1 in a certain region of L/a in all cases. In the case without dephasing, this is in accordance with existing random matrix theory.[33] Figure 6 shows a semilog plot of $\langle g \rangle$ in the regime of $\langle g \rangle < 1$. We find that $\langle g \rangle$ decays exponentially regardless of L_ϕ. In the absence of dephasing, it is natural that $\langle g \rangle$ decays exponentially, reflecting the onset of Anderson localization. The exponential decay of $\langle g \rangle$ even in the presence of dephasing should be regarded as a characteristic feature of the system in which conducting channels are imbalanced between two propagating directions.[29]

We turn to the SRI case. We use 10000 samples with different impurity configurations to calculate the average dimensionless conductance. Figure 7 shows that $\langle g \rangle$ decays to zero with increasing L/a, indicating the absence of a PCC.
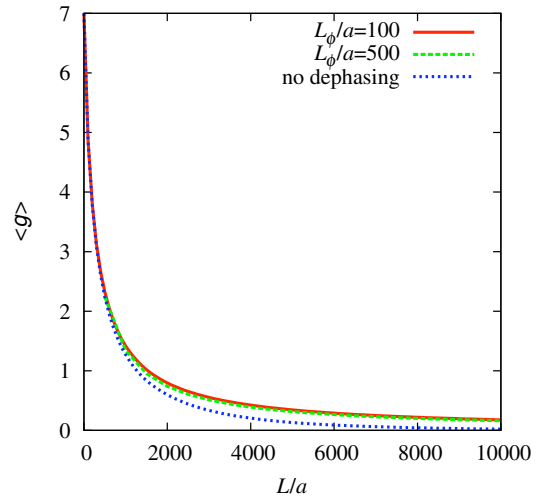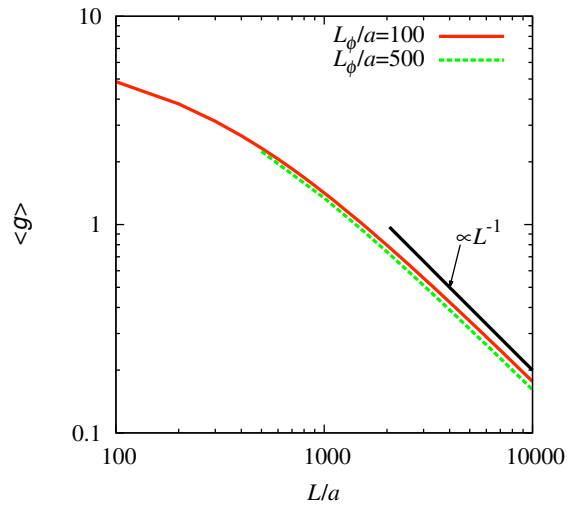
Figure 8 shows a log–log plot of $\langle g \rangle$ in the presence of dephasing. We find that $\langle g \rangle$ asymptotically becomes inversely proportional to L/a, manifesting that Ohm's law is satisfied upon the suppression of Anderson localization due to dephasing. This implies that the conducting channels are balanced as a consequence of the mixing of two valleys caused by strong intervalley scattering, in contrast to the LRI case. In the absence of dephasing, $\langle g \rangle$ decays exponentially with increasing L/a as shown in Fig. 9. We show error bars only in Fig. 9 as they are very small in the case with dephasing.

4. Comparison with the Boltzmann Transport Theory

In this section, we introduce an analytical expression for the dimensionless conductance derived from the Boltzmann transport equation[29] and compare it with the numerical results given in the previous section.

The analytical expression of Ref. 29 is derived by applying the Boltzmann transport equation to a simple model for zigzag nanoribbons and hence is justified in the incoherent limit where the phase coherence of electrons is completely
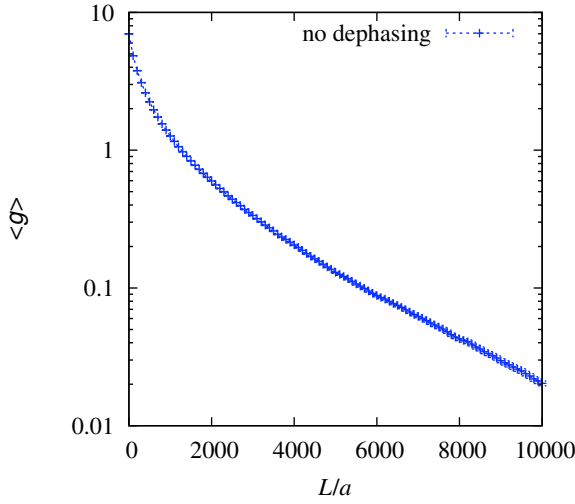
Fig. 9. (Color online) Semilog plot of $\langle g \rangle$ in the SRI case with no dephasing. $\langle g \rangle$ decays exponentially as a function of L/a.
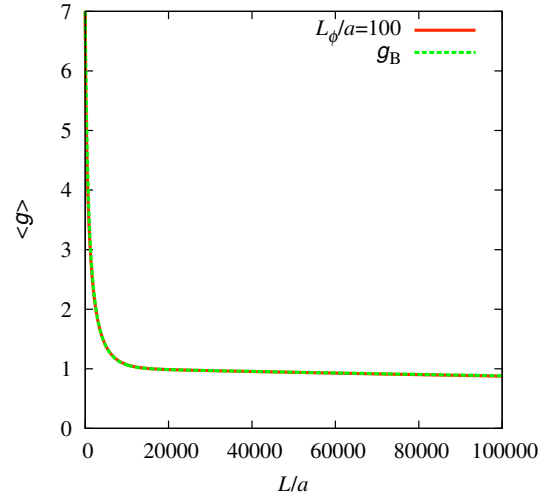

Fig. 10. (Color online) Fitting of $\langle g \rangle$ at $L_\phi/a = 100$ in the LRI case with the analytical expression g_B.

Fig. 11. (Color online) Fitting of $\langle g \rangle$ at $L_\phi/a = 100$ in the SRI case with the analytical expression g_B.

lost. The model possesses two energy valleys, and the number of conducting channels for right-going (left-going) electrons is $N + 1$ (N) in one valley, while in the other valley, that for right-going (left-going) electrons is N ($N + 1$). The total number of conducting channels is given by $N_c = 2N + 1$ including contributions from the two valleys. Disorder induces intravalley scattering between two channels in the same valley and intervalley scattering between two channels belonging to different valleys. The strength of intravalley scattering is characterized by a single parameter κ as its detailed dependence on initial and final states is ignored. In the same manner, the strength of intervalley scattering is characterized by a parameter κ'. Applying a constant electric field only in the region of length L, the Boltzmann equation is solved under the condition that incident electrons from the left and right are described by equilibrium distributions. The resulting dimensionless conductance g_B is expressed as[29]

$$g_B = \frac{[\kappa + (8N^2 + 8N + 1)\kappa']c_L}{(2N+1)\kappa'[2 + (2N+1)(\kappa + \kappa')L]c_L + \frac{\kappa^2 - \kappa'^2}{\sqrt{\alpha}}d_L}, \quad (6)$$

where $\alpha = (\kappa + \kappa')[\kappa + (8N^2 + 8N + 1)\kappa']$ and

$$c_L = \frac{(2N+1)(\kappa + \kappa')}{\sqrt{\alpha}}\cosh(\sqrt{\alpha}L/2) + \sinh(\sqrt{\alpha}L/2), \quad (7)$$

$$d_L = \frac{(2N+1)(\kappa + \kappa')}{\sqrt{\alpha}}\sinh(\sqrt{\alpha}L/2) + \cosh(\sqrt{\alpha}L/2). \quad (8)$$

We examine whether this expression can fit our numerical results. Equation (6) is justified in the incoherent limit, so we focus on the numerical results in the smallest-L_ϕ case with $L_\phi/a = 100$. As $N_c = 7$ in our setting, N is fixed at $N = 3$. Only κ and κ' play the role of fitting parameters. The result of fitting is shown in Fig. 10 in the LRI case and Fig. 11 in the SRI case. We observe that the analytical expression accurately reproduces the numerical results. The best fitting is achieved for $\kappa a = 0.00031$ and $\kappa' a = 0.00000003$ in the former case, yielding $\kappa'/\kappa = 0.0000096$, and for $\kappa a = 0.00094$ and $\kappa' a = 0.00021$ in the latter case, yielding $\kappa'/\kappa = 0.223$. This result clearly indicates that intervalley scattering is significantly weaker than intravalley scattering in
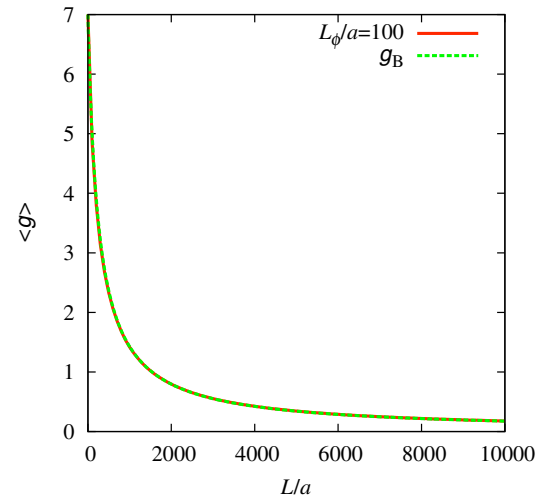
the LRI case while their strengths are on the same order of magnitude in the SRI case.

One may think that the effect of dephasing is oversimplified in the model used in our numerical calculations. However, the above result implies that our model captures the essential features of dephasing in spite of its simplicity.

5. Summary and Conclusion

We have studied the effect of dephasing on a perfectly conducting channel (PCC) in disordered graphene nanoribbons with zigzag edges by numerically calculating the average dimensionless conductance $\langle g \rangle$ as a function of system length L. We separately consider the case with long-range impurities (LRIs) and that with short-range impurities (SRIs). In the former case, intervalley scattering is very weak and the appearance of a PCC is expected. Contrastingly, a PCC cannot appear owing to strong intervalley scattering in the latter case. The result of the LRI case indicates that $\langle g \rangle$ as a function of L shows two-stage behavior; $\langle g \rangle$ rapidly decreases to 1 with increasing L in the first stage and then

tends to decay below 1 in the second stage. The behavior in the first stage implies the presence of a PCC, and the behavior in the second stage indicates that the PCC is destabilized by weak intervalley scattering. We have clearly observed that dephasing significantly relaxes the second-stage behavior and hence effectively stabilizes the PCC. This stabilization should be attributed to the suppression of Anderson localization due to dephasing. In the SRI case, $\langle g \rangle$ decays toward zero, reflecting the absence of a PCC. We have shown that dephasing suppresses the effect of Anderson localization, revealing the behavior of $\langle g \rangle \propto L^{-1}$ in accordance with the ordinary Ohm's law.

One may think that the experimental detection of a PCC in realistic systems is not easy as various inelastic processes obstruct it. Among them, dephasing is known as the most notable factor that suppresses quantum behaviors of electrons at low temperatures. Indeed, it has been pointed out that a PCC in CNTs, as well as in topological insulators, is fragile against dephasing.[5] Contrastingly, in graphene nanoribbons, dephasing does not negatively influence a PCC but rather encourages its appearance. This implies that graphene nanoribbons with zigzag edges are a promising platform for the experimental detection of a PCC.

1) M. Büttiker, Phys. Rev. B **38**, 9375 (1988).
2) T. Ando and T. Nakanishi, J. Phys. Soc. Jpn. **67**, 1704 (1998).
3) T. Ando, T. Nakanishi, and R. Saito, J. Phys. Soc. Jpn. **67**, 2857 (1998).
4) T. Nakanishi and T. Ando, J. Phys. Soc. Jpn. **68**, 561 (1999).
5) T. Ando and H. Suzuura, J. Phys. Soc. Jpn. **71**, 2753 (2002).
6) T. Ando, J. Phys. Soc. Jpn. **73**, 1273 (2004).
7) C. L. Kane and E. J. Mele, Phys. Rev. Lett. **95**, 146802 (2005).
8) C. L. Kane and E. J. Mele, Phys. Rev. Lett. **95**, 226801 (2005).
9) M. Onoda and N. Nagaosa, Phys. Rev. Lett. **95**, 106601 (2005).
10) B. A. Bernevig and S.-C. Zhang, Phys. Rev. Lett. **96**, 106802 (2006).
11) X.-L. Qi, Y.-S. Wu, and S.-C. Zhang, Phys. Rev. B **74**, 045125 (2006).
12) S. Murakami, Phys. Rev. Lett. **97**, 236805 (2006).
13) Y. Ran, Y. Zhang, and A. Vishwanath, Nat. Phys. **5**, 298 (2009).
14) K.-I. Imura, Y. Takane, and A. Tanaka, Phys. Rev. B **84**, 195406 (2011).
15) Z. Ringel, Y. E. Kraus, and A. Stern, Phys. Rev. B **86**, 045102 (2012).
16) Y. Yoshimura, A. Matsumoto, Y. Takane, and K.-I. Imura, Phys. Rev. B **88**, 045408 (2013).
17) K. Kobayashi, T. Ohtsuki, and K.-I. Imura, Phys. Rev. Lett. **110**, 236803 (2013).
18) Y. Zhang and A. Vishwanath, Phys. Rev. Lett. **105**, 206601 (2010).
19) R. Egger, A. Zazunov, and A. Levy Yeyati, Phys. Rev. Lett. **105**, 136403 (2010).
20) J. H. Bardarson, P. W. Brouwer, and J. E. Moore, Phys. Rev. Lett. **105**, 156803 (2010).
21) K. Wakabayashi, Y. Takane, and M. Sigrist, Phys. Rev. Lett. **99**, 036601 (2007).
22) K. Wakabayashi, Y. Takane, M. Yamamoto, and M. Sigrist, Carbon **47**, 124 (2009).
23) K. Wakabayashi, Y. Takane, M. Yamamoto, and M. Sigrist, New J. Phys. **11**, 095016 (2009).
24) C. Barnes, B. L. Johnson, and G. Kirczenow, Phys. Rev. Lett. **70**, 1159 (1993).
25) C. Barnes, B. L. Johnson, and G. Kirczenow, Can. J. Phys. **72**, 559 (1994).
26) K. Hirose, T. Ohtsuki, and K. Slevin, Physica E **40**, 1677 (2008).
27) M. Yamamoto, Y. Takane, and K. Wakabayashi, Phys. Rev. B **79**, 125421 (2009).
28) J. Wurm, M. Wimmer, and K. Richter, Phys. Rev. B **85**, 245418 (2012).
29) Y. Takane, J. Phys. Soc. Jpn. **79**, 024711 (2010).
30) Y. Takane, J. Phys. Soc. Jpn. **79**, 104706 (2010).
31) J. Baringhaus, M. Ruan, F. Edler, A. Tejeda, M. Sicot, A. Taleb-Ibrahimi, A.-P. Li, Z. Jiang, E. H. Conrad, C. Berger, C. Tegenkamp, and W. A. de Heer, Nature **506**, 349 (2014).
32) Y. Ashitani, K.-I. Imura, and Y. Takane, Int. J. Mod. Phys. Conf. Ser. **11**, 157 (2012).
33) Y. Takane and K. Wakabayashi, J. Phys. Soc. Jpn. **76**, 053701 (2007).

参考論文

(1) Electronic States and Local Density of Sates in Graphene with a
    Corner Edge Structure
    Yuji Shimomura, Yositake Takane, and Katsunori Wakabayashi
    Journal of the Physical Society of Japan, **80**, 054710, 1-9 (2011).

(2) Electronic States and Local Density of States near Graphene Corner
    Edge
    Yuji Shimomura, Yositake Takane, and Katsunori Wakabayashi
    International Journal of Modern Physics: Conference Series, **11**,
    151-156 (2012).

Electronic States and Local Density of States in Graphene with a Corner Edge Structure

Yuji SHIMOMURA, Yositake TAKANE, and Katsunori WAKABAYASHI[1,2]

Department of Quantum Matter, Graduate School of Advanced Sciences of Matter, Hiroshima University,
Higashihiroshima, Hiroshima 739-8530, Japan
[1]*International Center for Materials Nanoarchitectonics (MANA), National Institute for Materials Science (NIMS),*
Tsukuba, Ibaraki 305-0044, Japan
[2]*PRESTO, Japan Science and Technology Agency, Kawaguchi, Saitama 332-0012, Japan*

We study electronic states of semi-infinite graphene with a corner edge, focusing on the stability of edge localized states at zero energy. The 60, 90, 120, and 150° corner edges are examined. The 60 and 120° corner edges consist of two zigzag edges, while 90 and 150° corner edges consist of one zigzag edge and one armchair edge. We numerically obtain the local density of states (LDOS) on the basis of a nearest-neighbor tight-binding model by using Haydock's recursion method. We show that edge localized states appear along a zigzag edge of each corner edge structure except for the 120° case. To provide insight into this behavior, we analyze electronic states at zero energy within the framework of an effective mass equation. The result of this analysis is consistent with the behavior of the LDOS.

KEYWORDS: graphene corner edge, localized state, zigzag edge, armchair edge, tunneling spectroscopy

1. Introduction

The realization of a monolayer graphene sheet[1,2] has triggered extensive studies on its unusual electronic properties arising from the two-dimensional honeycomb structure of carbon atoms.[3] Since the unit cell of the honeycomb lattice contains two nonequivalent sites which form two sublattices A and B, the low-energy electronic states of graphene near the Fermi energy are described by a 2×2 matrix form which is equivalent to the massless Dirac equation.[4] Thus, electrons in graphene are called massless Dirac fermions. The band structure of massless Dirac fermions has a unique character, since they have linear energy dispersion in the vicinity of two nonequivalent symmetric points, called K^+ and K^- points, in the Brillouin zone, where the conduction and valence bands conically touch.[5] This structure is called Dirac cone. We hereafter set the electron energy at the band touching point as $\varepsilon = 0$. The unique energy band structure provide a number of intriguing physical properties such as the half-integer quantum Hall effect,[2,6] the absence of backward scattering associated with the Berry's phase by π[7] and Klein tunneling.[8]

The presence of edges makes an strong impact on the Dirac fermions in graphene near the Fermi energy. As stressed by Fujita *et al.*, the electronic states near the graphene edge strongly depends on its edge orientation.[9] Typical straight edges of graphene are classified into two structures: one is zigzag (zz) edge and the other is armchair (ac) edge. Fujita *et al.* analyzed electronic states in graphene with an infinitely long straight edge on the basis of a nearest-neighbor tight-binding model, and showed that highly degenerate edge localized states appear at $\varepsilon = 0$ along a zz edge.[9] These states at $\varepsilon = 0$ result in a sharp zero-energy peak structure in the local density of states (LDOS) near a straight zz edge of graphene. The edge localized states have a characteristic feature that their probability amplitude is finite only on one sublattice including edge sites and completely vanishes on the other sublattice. No such localized states appear along an ac edge. The presence of
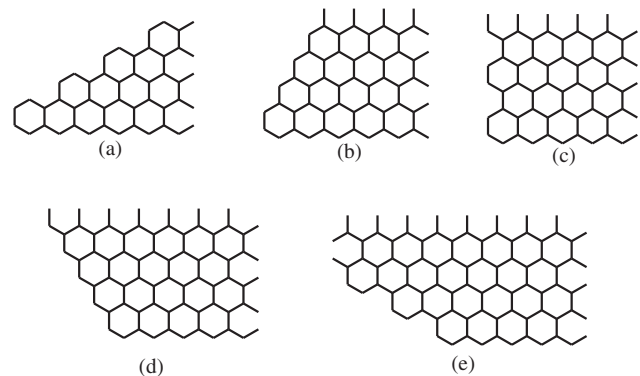

Fig. 1. Typical corner edge structures with corner angles of (a) 30, (b) 60, (c) 90, (d) 120, and (e) 150°.

edge localized states along a zz edge has been confirmed by using scanning tunneling microscopy and scanning tunneling spectroscopy.[10,11]

Theoretically, the presence or absence of zero-energy localized states has been well understood for infinitely long straight edges. However, actual edges of graphene samples are never straight nor infinitely long, and are much more complex than ideal ones. An actual edge line consists of several zz and/or ac segments, and a corner edge inevitably appears at the boundary of two adjacent segments. Typical corner edge structures are shown in Fig. 1. Hereafter each corner edge is referred to according to its corner angle. The 30, 90, and 150° corner edges consist of one zz edge and one ac edge, while the 60 and 120° corner edges consist of two zz edges. There arises a natural question: Do edge localized states exist at $\varepsilon = 0$ along a bent edge of these corner edge structures? In this paper we study electronic states in the corner edge structures to answer this question. We adopt a nearest-neighbor tight-binding model and numerically obtain the LDOS by using Haydock's recursion method. We find that edge localized states appear along a zz edge of

each corner edge structure with an exception of the 120° corner edge. In the 120° case, edge localized states locally disappear near the corner but emerge with increasing the distance from the corner. To provide insight into these unexpected behaviors, we analyze electronic states at $\varepsilon = 0$ within the framework of an effective mass equation. The result of this analysis is consistent with the behavior of the LDOS.

2. Formulations for Numerical Analysis

2.1 Model of graphene corner edges

We describe π electrons in graphene with a corner edge structure by using a tight-binding model on a honeycomb lattice. The Hamiltonian of this model is represented as

$$H = -t \sum_{\langle i,j \rangle} |i\rangle\langle j| + \sum_i w_i |i\rangle\langle i|, \qquad (1)$$

where t is the nearest neighbor hopping integral and w_i is a site-dependent potential. If $w_i = 0$ for any i, this model corresponds to a bulk graphene sheet. The site-dependent potential w_i is introduced for a technical reason. For practical application of our numerical approach, it is convenient to treat a lattice system being infinite in both the longitudinal and transverse directions. However, such a system contains lattice sites which are irrelevant for a corner edge structure. To model a corner edge on this infinite system, we put a large on-site potential on each irrelevant site to prevent electrons arriving on it. Therefore, we set $w_i = w$ with a sufficiently large w if the ith site is irrelevent for a corner edge structure while $w_i = 0$ otherwise. We consider four corner edges having corner angles differ from each other. The angles are 60, 90, 120, and 150°. We particularly focus on corner edges including one or two zz edges.

2.2 Haydock's recursion method

The LDOS can be calculated with Haydock's recursion method[12–15] which is applicable to systems having no translational symmetry such as graphene with a corner edge. By applying this method, we can obtain the LDOS at an arbitrary site.

We outline the method to obtain the LDOS at an ith site. To start with, we transform our model to a one-dimensional chain model. We first introduce the coefficient a_0 given by

$$a_0 = \langle l_0|H|l_0\rangle \qquad (2)$$

with $|l_0\rangle \equiv |i\rangle$, and define $|l_1\rangle$ and b_1 in terms of

$$b_1|l_1\rangle = (H - a_0)|l_0\rangle \qquad (3)$$

with $\langle l_1|l_1\rangle \equiv 1$. The coefficient b_1 is obtained as

$$b_1 = \sqrt{\langle l_0|(H - a_0)(H - a_0)|l_0\rangle}. \qquad (4)$$

We next introduce a_1 given by

$$a_1 = \langle l_1|H|l_1\rangle, \qquad (5)$$

and define $|l_2\rangle$ and b_2 in terms of

$$b_2|l_2\rangle = (H - a_1)|l_1\rangle - b_1|l_0\rangle \qquad (6)$$

with $\langle l_2|l_2\rangle \equiv 1$. The coefficient b_2 is obtained as

$$b_2 = \sqrt{\{\langle l_1|(H - a_1) - \langle l_0|b_1\}\{(H - a_1)|l_1\rangle - b_1|l_0\rangle\}}. \qquad (7)$$

Repeating this n times, we obtain

$$b_{n+1}|l_{n+1}\rangle = (H - a_n)|l_n\rangle - b_n|l_{n-1}\rangle, \qquad (8)$$

with

$$a_n = \langle l_n|H|l_n\rangle, \qquad (9)$$

$$b_{n+1}$$
$$= \sqrt{\{\langle l_n|(H - a_n) - \langle l_{n-1}|b_n\}\{(H - a_n)|l_n\rangle - b_n|l_{n-1}\rangle\}}. \qquad (10)$$

This manipulation with the reccurence equation, eq. (8), is equivalent to a transformation of the original electron system to a one-dimensional chain model. $\{|l_0\rangle, |l_1\rangle, |l_2\rangle, \ldots\}$ stands for the orthonormal basis set of the chain model. Here, $|l_n\rangle$ involves neighboring sites of $|i\rangle$ up to the nth nearest neighbors. On this basis, H can be rewritten with real coefficients $\{a_0, a_1, \ldots\}$ and $\{b_1, b_2, \ldots\}$ as a tridiagonal matrix

$$H = \begin{pmatrix} a_0 & b_1 & & & \\ b_1 & a_1 & b_2 & & \\ & b_2 & a_2 & b_3 & \\ & & b_3 & a_3 & \\ & & & & \ddots \end{pmatrix}. \qquad (11)$$

With the coefficients $\{a_0, a_1, \ldots\}$ and $\{b_1, b_2, \ldots\}$, the Green's function $G_i(E)$ for the ith site can be represented as a continued fraction,

$$G_i(E) = \cfrac{1}{E - a_0 - \cfrac{b_1^2}{E - a_1 - \cfrac{b_2^2}{\cdots}}}. \qquad (12)$$

Practically, we need to terminate this continued fraction at a sufficiently large n. If it is terminated at $n = N$, we obtain the approximate expression of $G_i(E)$ as

$$G_i(E) = \cfrac{1}{E - a_0 - \cfrac{b_1^2}{E - a_1 - \cfrac{b_2^2}{\cfrac{\cdots}{E - a_N - t(E)}}}}, \qquad (13)$$

where

$$t(E) = \frac{E - a_N}{2b_N^2}\left\{1 - \left[1 - \frac{4b_N^2}{(E - a_N)^2}\right]^{1/2}\right\}. \qquad (14)$$

$G_i(E)$ gives the LDOS at the ith site in terms of the relation

$$N_i(E) = \frac{1}{\pi} \text{Im}\, G_i(E - i\delta), \qquad (15)$$

where δ is a positive infinitesimal. In actual numerical calculations, we treat δ as a sufficiently small but finite constant.

3. The LDOS

3.1 The LDOS in the presence of a single edge

To confirm the validity of our approach using the recursion method, we calculate the LDOS in the presence of an ideal single zz or ac edge. We set $N = 1000$, $w/t = 300$, and $\delta/t = 0.01$ throughout this paper. We first consider the case with a single zz edge. The site indices in the unit cell are given in Fig. 2(a). We display the LDOS at the sites 1, 2, 3, and 4 in Figs. 2(b)–2(e). A peak at $\varepsilon = 0$ exists at the
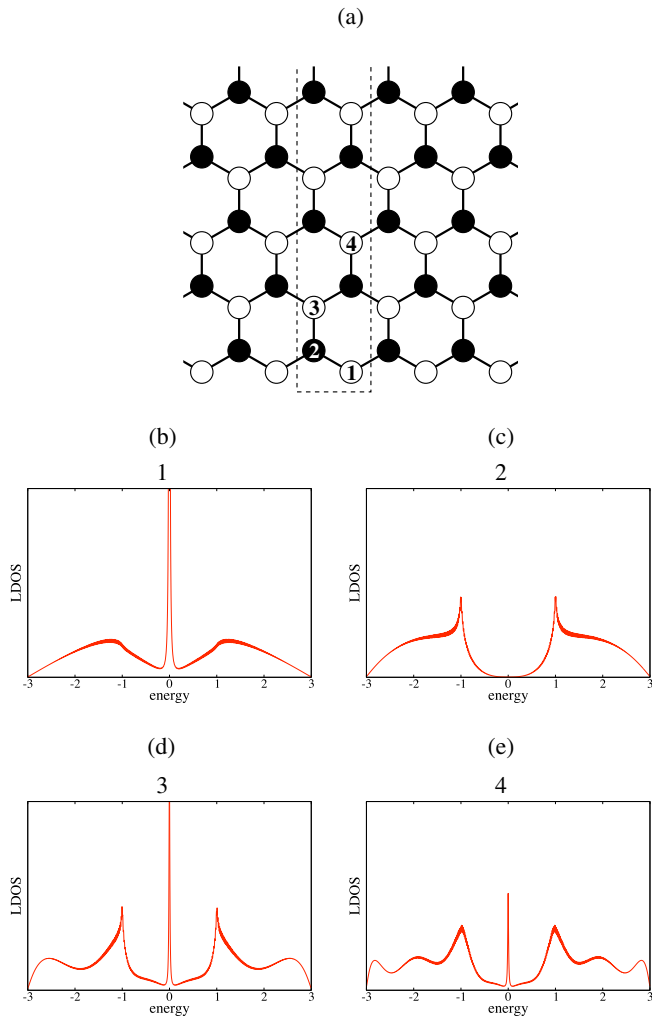
Fig. 2. (Color online) (a) The strcture of a single zz edge. A broken line represents a unit cell. (b), (c), (d), and (e) display the LDOS at the site 1, site 2, site 3, and site 4, respectively. The number indicated above each graph represents the site number defined in (a).

Fig. 3. (Color online) (a) The strcture of a single ac edge. A broken line represents a unit cell. (b) and (c) display the LDOS at the site 5 and site 6, respectively. The number indicated above each graph represents the site number defined in (a).

site 1 on the zz edge. The LDOS also possesses a zero-energy peak at sites on the sublattice which includes the site 1. We see that the peak decays with increasing the distance from the edge. At the sites belonging to the other sublattice, such as the site 2, a peak does not appear at $\varepsilon = 0$. These results are consistent with the presence of edge states at $\varepsilon = 0$. The decay of the zero-energy peak reflects the fact that an edge state has a finite penetration depth.

We next consider the case with a single ac edge. Figure 3 shows the LDOS in the presence of a single ac edge. We do not observe a peak of the LDOS at $\varepsilon = 0$. This is consistent with the absence of edge states in the single ac edge case.

3.2 The LDOS in the presence of a corner edge
3.2.1 60° corner edge

Figure 4 shows the LDOS at several sites in the presence of the 60° corner edge consisting of two zz edges. From this figure, we can see the appearance of edge states at $\varepsilon = 0$. As shown in Figs. 4(b) and 4(e), a zero-energy peak exists at the sites 7 and 10 belonging to a same sublattice. Let us compare the LDOS at the site 10 [Fig. 4(e)] with that at the site 4 in the single zz edge case [Fig. 2(e)]. Note that the distance
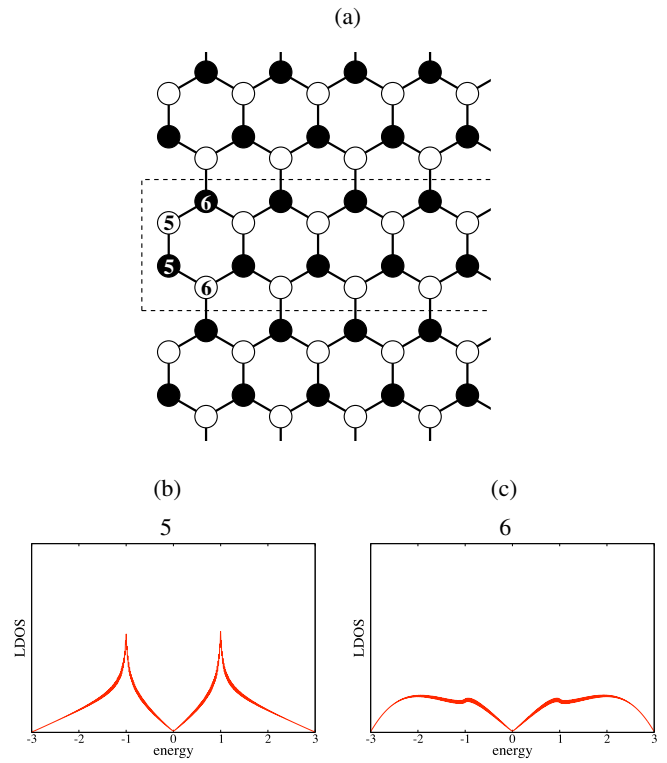
from the zz edge to the site of our interest is equivalent in both the cases. We observe that the peak of the LDOS at the site 10 is higher than that at the site 4 in the single zz edge case. We consider that this enhancement of the zero-energy peak at the site 10 is caused by a superposition of edge states at one zz edge and those at the other edge, i.e., constructive interference between two edge states.

3.2.2 90° corner edge

Figure 5 shows the LDOS at several sites in the presence of the 90° corner edge. From this figure, we see that edge states appear at $\varepsilon = 0$. As shown in Figs. 5(b), 5(d), and 5(e), a zero-energy peak exists at the sites 11, 13, and 14 belonging to a same sublattice. Thus, the LDOS near the corner possesses both the character of the LDOS in the single zz edge case and that in the single ac edge case. Let us focus on the LDOS at the site 13 for example. The site 13 corresponds to the site 3 in the zz edge case [Fig. 2(d)] and the site 5 in the single ac edge case [Fig. 3(b)]. Roughly speaking, we can regard that the LDOS at the site 13 [Fig. 5(d)] is a mixture of the LDOS at the site 3 [Fig. 2(d)] and the site 5 [Fig. 3(b)]. The nature similar to this is also observed at other sites. There is no enhancement of the zero-energy peak of LDOS in contrast to the 60° case.

3.2.3 120° corner edge

Figure 6 shows the LDOS at several sites in the presence of the 120° corner consisting of two zz edges. In this case, peculiar features arise. The LDOS at the site 15 [Fig. 6(b)] is quite different from that of the site 1 in the single zz edge
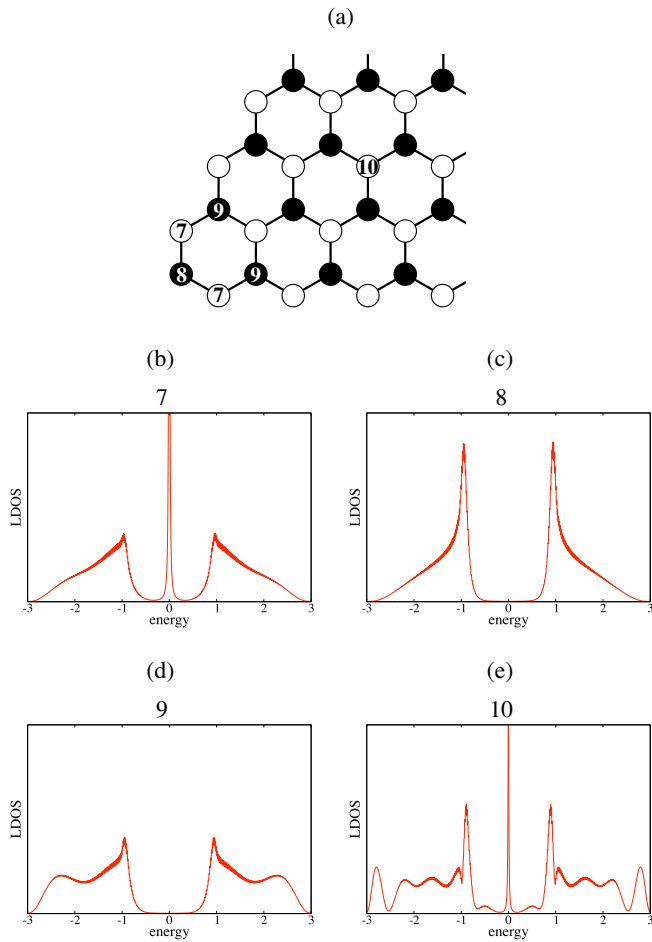

Fig. 4. (Color online) (a) The strcture of the 60° corner edge. (b), (c), (d), and (e) display the LDOS at the site 7, site 8, site 9, and site 10, respectively. The number indicated above each graph represents the site number defined in (a).

Fig. 5. (Color online) (a) The strcture of the 90° corner edge. (b), (c), (d), and (e) display the LDOS at the site 11, site 12, site 13, and site 14, respectively. The number indicated above each graph represents the site number defined in (a).

case [Fig. 2(b)]. As seen from Figs. 6(b), 6(c), and 6(g), there is no zero-energy peak at the sites near the corner and hence edge states locally disappear. However, edge states appear at the sites away from the corner. Indeed we observe a broad peak at the site 17 [Fig. 6(d)], and the LDOS at the site 18 [Fig. 6(e)] shows a sharp peak.

3.2.4 150° corner edge

Figure 7 shows the LDOS at several sites in the presence of the 150° corner edge. As shown in Figs. 7(b), 7(d), and 7(e), a zero-energy peak exists at the sites 21, 23, and 24 belonging to a same sublattice. This indicates the existence of edge states. As in the 90° case, the LDOS near the corner possesses both the character of the LDOS in the single zz edge case and that in the single ac edge case. For example, we can regard that the LDOS at the site 24 [Fig. 7(e)] is a mixture of the LDOS at the site 4 on the single zz edge [Fig. 2(e)] and that at the site 6 on the single ac edge [Fig. 3(c)]. The peculiarity of the 150° case is that the zero-energy peak of the site 21 is quite smaller than that at the site 1 on the single zz edge [Fig. 2(b)].

Figure 8 represents the spatial dependance of the LDOS at ε = 0 in the presence of the (a) 60, (b) 90, and (c) 150° corner edges. A radius of each open circle indicates the magnitude of the LDOS. In these figures, the LDOS has a
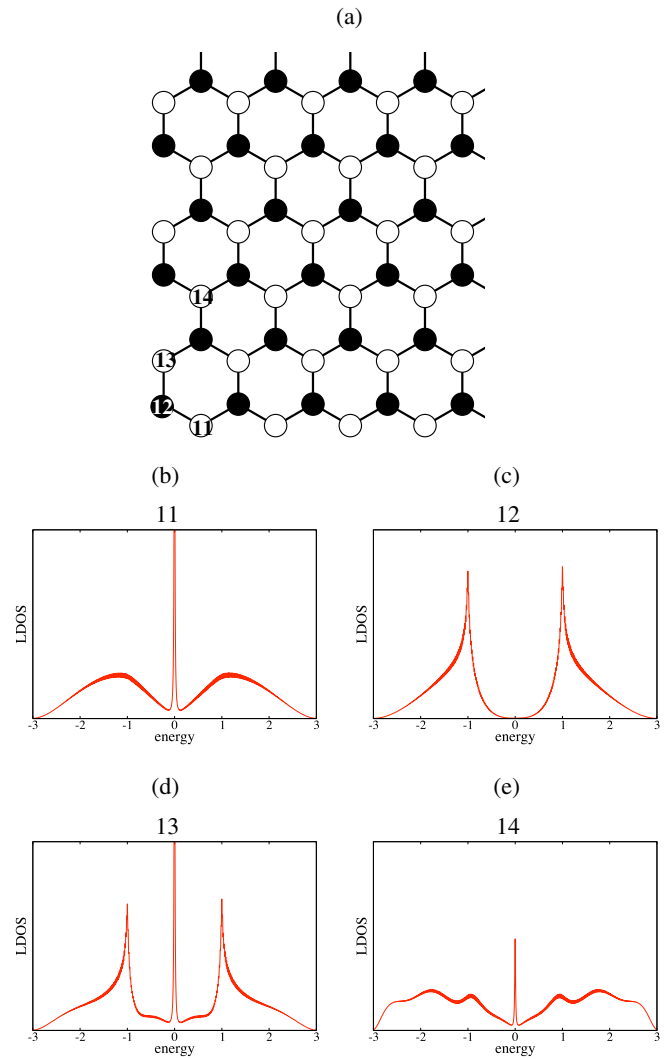
finite value only on the sublattice involving zz edge sites but vanishes on the other sublattice. We observe that the LDOS localizes near zz edges, indicating the presence of edge localized states. However, special emphasis is placed on the case of the 60° corner edge, where the magnitude of the LDOS at inner sites is larger than that in the other two cases. This reflects the fact that edge localized states are present at both the two zz edges. The overlap of these edge localized states enhances the magnitude of the LDOS, i.e., constructive interference. The other corner edge structures with the angle 90 or 150° consist of one zz edge and one ac edge. Note the LDOS in the single ac edge system vanishes at ε = 0 on any sites. In these corner edge structures, the LDOS becomes finite even at ε = 0 due to the presence of a zz edge. Even at sites on the ac edge, the LDOS can have a finite value.

Figure 9 represents the spatial dependance of the LDOS at ε = 0 in the presence of the 120° corner edge. In this figure, we observe that the LDOS vanishes at the sites near the corner, indicating local disappearance of edge states, i.e. destructive interference. In spite of the fact that the 120°
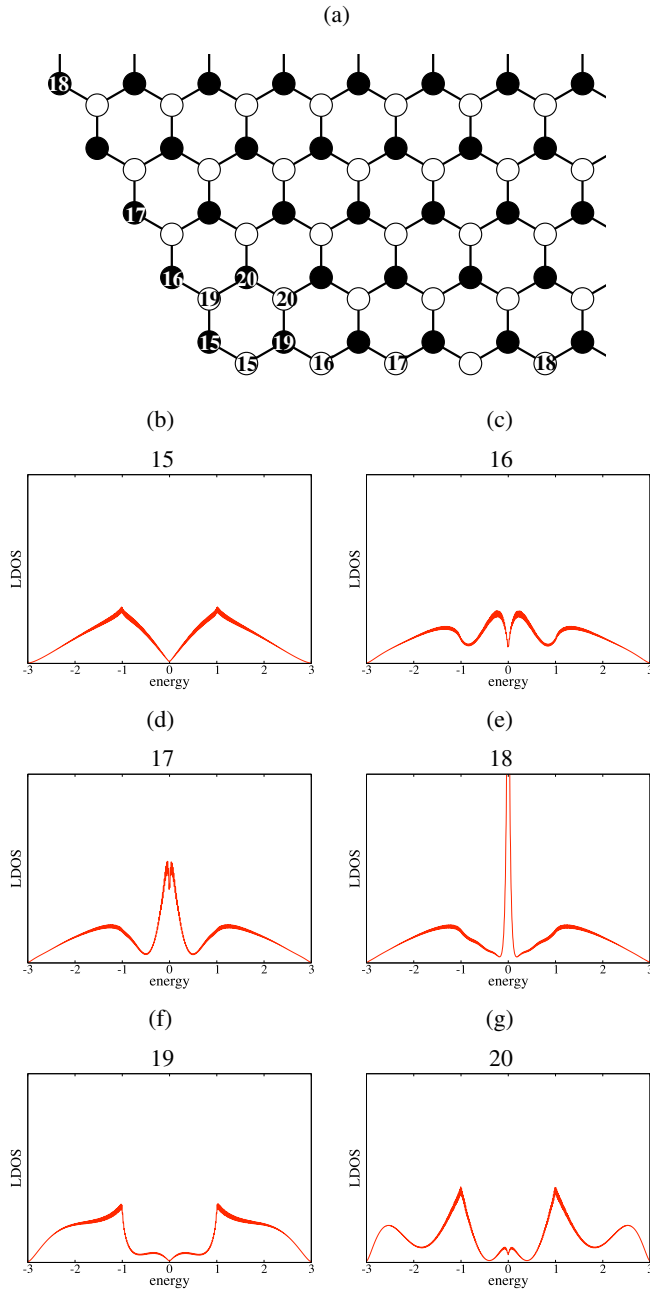
(a)

(b)
15

(c)
16

(d)
17

(e)
18

(f)
19

(g)
20

Fig. 6. (Color online) (a) The strcture of the 120° corner edge. (b), (c), (d), (e), (f), and (g) display the LDOS at the site 15, site 16, site 17, site 18, site 19, and site 20, respectively. The number indicated above each graph represents the site number defined in (a).

(a)

(b)
21

(c)
22

(d)
23

(e)
24

Fig. 7. (Color online) (a) The strcture of the 150° corner edge. (b), (c), (d), and (e) display the LDOS at the site 21, site 22, site 23, and site 24, respectively. The number indicated above each graph represents the site number defined in (a).

corner edge consists of two zz edges, the edge states are not fully stabilized in contrast to the case of the 60° corner edge. Note that in the 120° case, edge sites on one zz edge and those on the other zz edge belong to different sublattices, while all edge sites in the 60° case belong to a same sublattice. As we discuss in the next section, this is the reason for the qualitative difference between the two cases.

4. Analytical Treatment

Our study on the LDOS reveals that edge localized states are stabilized in corner edge structures except for the 120° case. To provide insight into this behavior, we analyze edge localized states in corner edge structures by using an effective mass description, which is applicable to low-energy states in
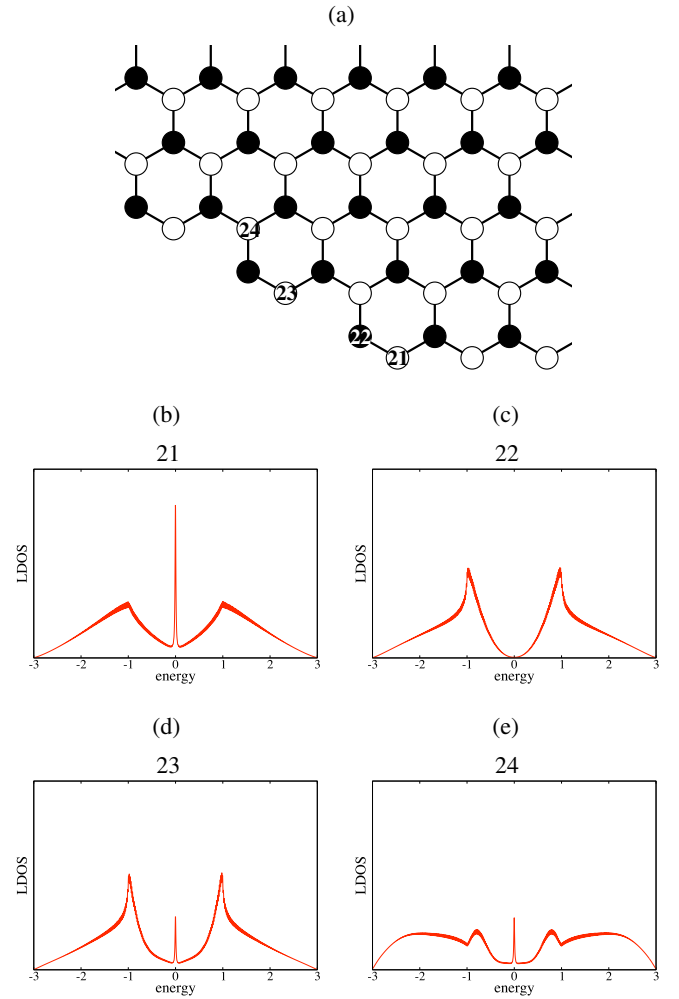
the vicinity of the $K^{\pm}$ point. The K^{+} and K^{-} points are characterized by $\boldsymbol{K}^{+} = (-4\pi/3a, 0)$ and $\boldsymbol{K}^{-} = (4\pi/3a, 0)$, respectively. Here, a is lattice constant. As shown in Fig. 10(a), the unit cell of graphene has two non-equivalent carbon atoms A and B which form A sublattice and B sublattice, respectively. We represent the wave function $\psi_{\mathrm{A}}(\boldsymbol{r})$ for A sublattice and the wave function $\psi_{\mathrm{B}}(\boldsymbol{r})$ for B sublattice as

$$\psi_{\mathrm{A}}(\boldsymbol{r}) = \mathrm{e}^{\mathrm{i}\boldsymbol{K}^{+}\cdot\boldsymbol{r}}F_{\mathrm{A}}^{+}(\boldsymbol{r}) + \mathrm{e}^{\mathrm{i}\boldsymbol{K}^{-}\cdot\boldsymbol{r}}F_{\mathrm{A}}^{-}(\boldsymbol{r}), \quad (16)$$

$$\psi_{\mathrm{B}}(\boldsymbol{r}) = \mathrm{e}^{\mathrm{i}\boldsymbol{K}^{+}\cdot\boldsymbol{r}}F_{\mathrm{B}}^{+}(\boldsymbol{r}) - \mathrm{e}^{\mathrm{i}\boldsymbol{K}^{-}\cdot\boldsymbol{r}}F_{\mathrm{B}}^{-}(\boldsymbol{r}), \quad (17)$$

where $F^{\pm}$ are envelope functions near the $K^{\pm}$ point. The envelope functions at energy ε satisfy

$$\gamma \begin{pmatrix} 0 & \hat{k}_x - \mathrm{i}\hat{k}_y & 0 & 0 \\ \hat{k}_x + \mathrm{i}\hat{k}_y & 0 & 0 & 0 \\ 0 & 0 & 0 & \hat{k}_x + \mathrm{i}\hat{k}_y \\ 0 & 0 & \hat{k}_x - \mathrm{i}\hat{k}_y & 0 \end{pmatrix} \begin{pmatrix} F_{\mathrm{A}}^{+}(\boldsymbol{r}) \\ F_{\mathrm{B}}^{+}(\boldsymbol{r}) \\ F_{\mathrm{A}}^{-}(\boldsymbol{r}) \\ F_{\mathrm{B}}^{-}(\boldsymbol{r}) \end{pmatrix}$$

$$= \varepsilon \begin{pmatrix} F_{\mathrm{A}}^{+}(\boldsymbol{r}) \\ F_{\mathrm{B}}^{+}(\boldsymbol{r}) \\ F_{\mathrm{A}}^{-}(\boldsymbol{r}) \\ F_{\mathrm{B}}^{-}(\boldsymbol{r}) \end{pmatrix}, \quad (18)$$
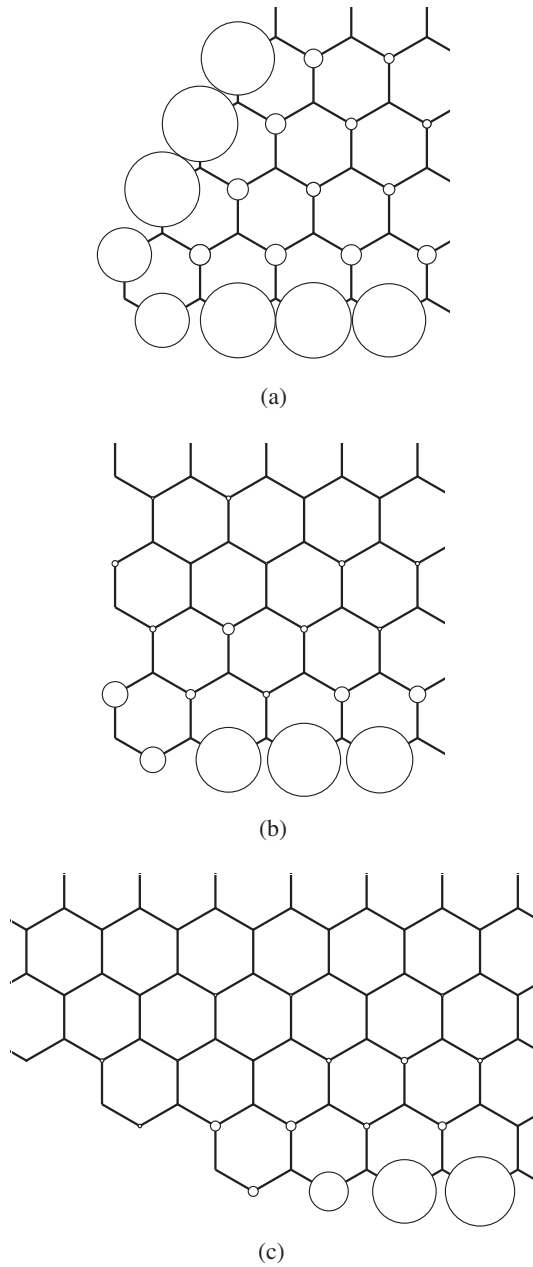
(a)

(b)

Fig. 8. The LDOS in the presence of the (a) 60, (b) 90, and (c) 150° corner edges at $\varepsilon = 0$. The radius of open circles indicates the magnitude of the LDOS.
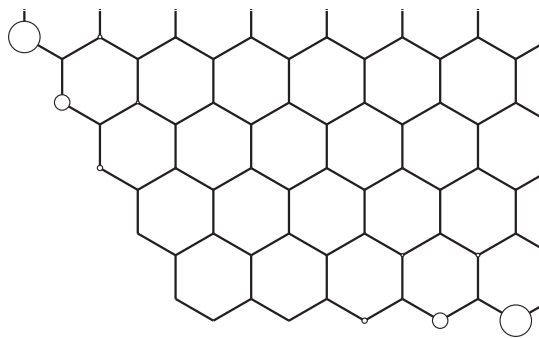

Fig. 9. The LDOS in the presence of the 120° corner edge at $\varepsilon = 0$. The radius of open circles indicates the magnitude of the LDOS.
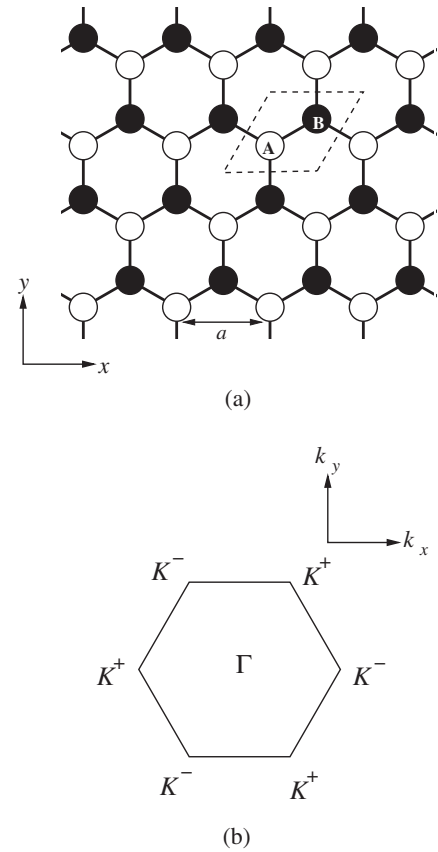

(a)

(b)

Fig. 10. (a) Honeycomb structure of graphene. The region enclosed in a broken line is a unit cell. A and B are non-equivalent sites which form sublattices. (b) The first Brillouin zone of graphene, where K^+, K^-, and Γ are symmetric points. The K^+ point is located at $(-4\pi/3a, 0)$ and $(2\pi/3a, \pm 2\pi/\sqrt{3}a)$ while the K^- point is located at $(4\pi/3a, 0)$ and $(-2\pi/3a, \pm 2\pi/\sqrt{3}a)$.

where γ is a band parameter, $\hat{k}_x = -i\partial/\partial x$, and $\hat{k}_y = -i\partial/\partial y$. This is called $\boldsymbol{k} \cdot \boldsymbol{p}$ equation,[4,16] which is an effective mass equation for graphene systems.

For later convenience, we present the envelope functions for edge states at $\varepsilon = 0$.[17] Let us consider a semi-infinite graphene which occupies the region of $y > 0$, and has a zigzag edge at $y = 0$. Assuming that edge sites belong to A sublattice, we adopt the boundary condition of $F_{\mathrm{B}}^{\pm}(\boldsymbol{r})|_{y=0} = 0$. The envelope functions for edge states are given as

$$\begin{pmatrix} F_{\mathrm{A}}^{\pm}(\boldsymbol{r}) \\ F_{\mathrm{B}}^{\pm}(\boldsymbol{r}) \end{pmatrix} = C\begin{pmatrix} \mathrm{e}^{\pm i k_x x} \mathrm{e}^{-k_x y} \\ 0 \end{pmatrix}, \qquad (19)$$

where C is a normalization constant. The absolute value of $F_{\mathrm{A}}^{\pm}$ in eq. (19) has a maximum value at $y = 0$ and exponentially decays with increasing y. This represents edge states localized along the zz edge. We construct zero-energy wave functions which satisfy the boundary condition of corner edges by using eq. (19).

4.1 60° corner edge

We first consider wave functions in the presence of the 60° corner edge as shown in Fig. 11. We attempt to construct wave functions near the K^+ point in terms of two edge localized wave functions. One is the wave function for the 0° zz edge
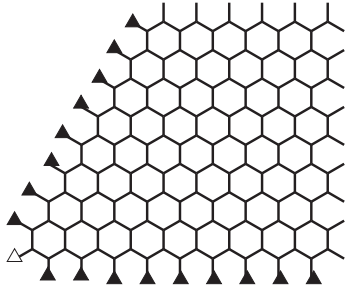
Fig. 11. The boundary condition for the 60° corner edge requires that wave functions vanish at sites marked with a triangle. A site marked with an open triangle belongs to A sublattice, and sites marked with a filled triangle belong to B sublattice.

Fig. 12. The boundary condition for 90° corner edge requires that wave functions vanish at sites marked with a triangle. Sites marked with an open triangle belong to A sublattice, and sites marked with a filled triangle belong to B sublattice.

$$C\begin{pmatrix} e^{-iKx}e^{ik_x(x+iy)} \\ 0 \end{pmatrix}, \tag{20}$$

and the other is the wave function for the 60° zz edge

$$C\begin{pmatrix} e^{-iKx}e^{ik_x(x+iy)e^{i(2/3)\pi}} \\ 0 \end{pmatrix}, \tag{21}$$

where $K \equiv 4\pi/3a$. Here and hereafter we refer to zz edge intersecting the x axis with angle θ degree as $\theta°$ zz edge. We adopt their linear combination

$$\begin{pmatrix} \psi_A(r) \\ \psi_B(r) \end{pmatrix} = \begin{pmatrix} e^{-iKx}(C_1 e^{ik_x(x+iy)} + C_2 e^{ik_x(x+iy)e^{i(2/3)\pi}}) \\ 0 \end{pmatrix} \tag{22}$$

as a trial wave function in the presence of the 60° corner edge. The boundary condition requires that the wave function vanishes at sites marked with triangles in Fig. 11. Because $\psi_B(r) = 0$, we need to consider only the boundary condition for $\psi_A(r)$. Only the site at the corner with an open triangle belongs to A sulattice. We define this site as the origin of the coordinate. Hence, the boundary condition for $\psi_A(r)$ is simply given by

$$\psi_A(0,0) = 0, \tag{23}$$

yielding $C_2 = -C_1$. We obtain the wave function in the presence of the 60° corner edge as

$$\begin{pmatrix} \psi_A(r) \\ \psi_B(r) \end{pmatrix} = C\begin{pmatrix} e^{-iKx}(e^{ik_x(x+iy)} - e^{ik_x(x+iy)e^{i(2/3)\pi}}) \\ 0 \end{pmatrix}. \tag{24}$$

This indicates the existence of edge states in the 60° corner edge.[18]

4.2 90° corner edge

Secondly we consider the 90° corner edge as shown in Fig. 12. In this case, states near K^+ and K^- points are mixed due to the presence of an ac edge. We construct zero-energy wave functions by using edge localized wave function near the K^+ point,

$$C\begin{pmatrix} e^{-iKx}e^{ik_x(x+iy)} \\ 0 \end{pmatrix}, \tag{25}$$

and that near the K^- point,

$$C\begin{pmatrix} e^{iKx}e^{-ik_x(x-iy)} \\ 0 \end{pmatrix}. \tag{26}$$
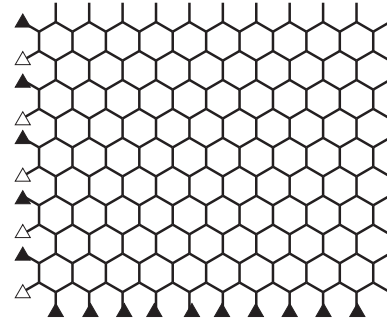
We adopt their linear combination

Fig. 13. The boundary condition for the 150° corner edge requires that wave functions vanish at sites marked with a triangle. Sites marked with an open triangle belong to A sublattice, and sites marked with a filled triangle belong to B sublattice.
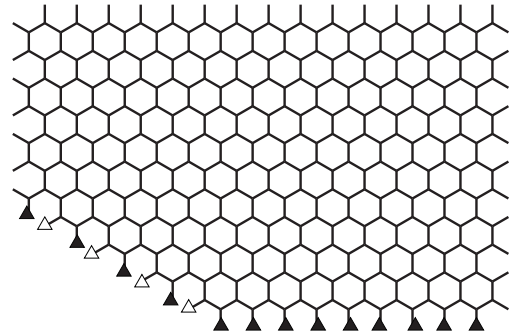
$$\begin{pmatrix} \psi_A(r) \\ \psi_B(r) \end{pmatrix} = \begin{pmatrix} C_3 e^{-iKx}e^{ik_x(x+iy)} + C_4 e^{iKx}e^{-ik_x(x-iy)} \\ 0 \end{pmatrix} \tag{27}$$

as a trial wave function. This must vanishes at sites marked with triangles in Fig. 12. Because $\psi_B(r) = 0$, we need to consider only the boundary condition for $\psi_A(r)$. The sites marked with open triangles belong to A sulattice. We define the site at the corner with an open triangle as the origin. The coordinates of the open triangles are $(x, y) = (0, \sqrt{3}a \times m)$ with $m = 0, 1, 2, \ldots$. Hence, the boundary condition for $\psi_A(r)$ reads

$$\psi_A(0, \sqrt{3}a \times m) = 0 \quad (m = 0, 1, 2, \ldots). \tag{28}$$

Imposing this condition to ψ_A in eq. (27), we obtain $C_4 = -C_3$. We obtain the wave function for the 90° corner edge as

$$\begin{pmatrix} \psi_A(r) \\ \psi_B(r) \end{pmatrix} = C\begin{pmatrix} e^{-iKx}e^{ik_x(x+iy)} - e^{iKx}e^{-ik_x(x-iy)} \\ 0 \end{pmatrix}. \tag{29}$$

This indicates the existence of edge states in the 90° corner edge.

4.3 150° corner edge

Thirdly we consider the 150° corner edge as shown in Fig. 13. We obtain zero-energy wave functions using a conformal mapping technique.[19] In terms of the complex variable $z \equiv x + iy$, eq. (19) is rewritten as
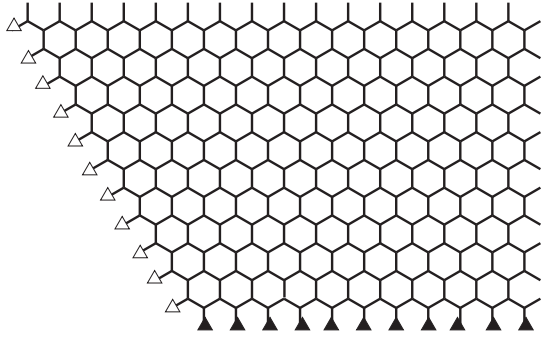
Fig. 14. The boundary condition for the 120° corner edge requires that wave functions vanish at sites marked with a triangle. Sites marked with an open triangle belong to A sublattice, and sites marked with a filled triangle belong to B sublattice.

$$\begin{pmatrix} F_A^+(z) \\ F_B^+(z) \\ F_A^-(z) \\ F_B^-(z) \end{pmatrix} = \begin{pmatrix} Ce^{ik_xz} \\ 0 \\ C'e^{-ik_xz^*} \\ 0 \end{pmatrix}, \tag{30}$$

where z^* is the complex conjugate of z. Here we introduce the transformation of $w = z^{3/5}$. This transformation maps a 150° corner on z plane to a 90° corner on w plane and *vice versa*. Thus, the wave function for the 90° corner edge on w plane

$$\begin{pmatrix} \psi_A(w) \\ \psi_B(w) \end{pmatrix} = C \begin{pmatrix} e^{-iKx}e^{ik_xw} - e^{iKx}e^{-ikw^*} \\ 0 \end{pmatrix} \tag{31}$$

is mapped to

$$\begin{pmatrix} \psi_A(\boldsymbol{r}) \\ \psi_B(\boldsymbol{r}) \end{pmatrix} = C \begin{pmatrix} e^{-iKx}e^{ik_xz^{3/5}} - e^{iKx}e^{-ik_xz^{*3/5}} \\ 0 \end{pmatrix} \tag{32}$$

$$= C \begin{pmatrix} e^{-iKx}e^{ik_x(x+iy)^{3/5}} - e^{iKx}e^{-ik_x(x-iy)^{3/5}} \\ 0 \end{pmatrix} \tag{33}$$

on z plane. The boundary condition requires that the wave function vanishes at sites marked with triangles in Fig. 13. Again, we need to consider only the boundary condition for $\psi_A(\boldsymbol{r})$. The sites marked with open triangles belong to A sulattice. We define the site at the corner with an open triangle as the origin. The coordinates of the open triangles are $(x, y) = (-(3/2)a \times m, (\sqrt{3}/2)a \times m)$ with $m = 0, 1, 2, \ldots$. Hence, the boundary condition for $\psi_A(\boldsymbol{r})$ is given by

$$\psi_A\left(-\frac{3}{2}a \times m, \frac{\sqrt{3}}{2}a \times m\right) = 0 \quad (m = 0, 1, 2, \ldots). \tag{34}$$

The wave function ψ_A in eq. (33) satisfies this condition. Therefore eq. (33) can be considered as a wave function in the presence of the 150° corner edge. This indicates the existence of edge states. The envelope functions $e^{ik_x(x+iy)^{3/5}}$ and $e^{-ik_x(x-iy)^{3/5}}$ are different from ordinary envelope functions given in eq. (19), but both satisfy the $\boldsymbol{k} \cdot \boldsymbol{p}$ equation given in eq. (18).

4.4 120° corner edge

Lastly we consider the 120° corner edge as shown in Fig. 14. The boundary condition requires that $\psi_B(\boldsymbol{r})$ vanishes at sites marked with a filled triangle and $\psi_A(\boldsymbol{r})$ vanishes at sites marked with an open triangle. Therefore, both $\psi_A(\boldsymbol{r})$ and $\psi_B(\boldsymbol{r})$ are subjected to the boundary condition, in

contrast to the 60° case where one component is free from the boundary condition. This crucially affects zero-energy states in the 120° case as we see below. Similar to the treatment for the 60° case, we first adopt a linear combination of the wave function for the 0° zz edge and that for the 120° zz edge as a trial wave function. The wave function for the 0° zz edge near the K^+ point is

$$C \begin{pmatrix} e^{-iKx}e^{ik_x(x+iy)} \\ 0 \end{pmatrix} \tag{35}$$

and the wave function for the 120° zz edge near the K^+ point is

$$C \begin{pmatrix} 0 \\ e^{-iKx}e^{-ik_x(x-iy)e^{-i(\pi/3)}} \end{pmatrix}. \tag{36}$$

The former has only the A-sublattice component, while the latter has only the B-sublattice component. Obviously, their linear combination does not satisfy the boundary condition for both the A- and B-sulattice components. We next consider a linear combination of the 0° edge wave functions near the K^+ and K^- points,

$$\begin{pmatrix} \psi_A(\boldsymbol{r}) \\ \psi_B(\boldsymbol{r}) \end{pmatrix} = \begin{pmatrix} C_5 e^{-iKx}e^{ik_x(x+iy)} + C_6 e^{iKx}e^{-ik_x(x-iy)} \\ 0 \end{pmatrix}. \tag{37}$$

This is equivalent to eq. (27). Though ψ_B of eq. (37) satisfies the boundary condition, ψ_A cannot satisfy the boundary condition for arbitrary C_5 and C_6. Finally, we consider a linear combination of the 0° zz edge wave function and an arbitrary evanescent wave function near the $K^\pm$ point given by

$$C \begin{pmatrix} e^{\mp iKx}e^{\pm ip(x\pm iy)e^{\pm i\theta}} \\ 0 \end{pmatrix}. \tag{38}$$

This wave function, reducing to the 0° zz edge wave function when $\theta \to 0$, satisfies eq. (18) and is bounded for $0 \leq \theta \leq \frac{\pi}{3}$ in the 120° case. Their linear combination

$$\begin{pmatrix} \psi_A(\boldsymbol{r}) \\ \psi_B(\boldsymbol{r}) \end{pmatrix} = \begin{pmatrix} C_7 e^{-iKx}e^{ik_x(x+iy)} + C_8 e^{\mp iKx}e^{\pm ip(x\pm iy)e^{\pm i\theta}} \\ 0 \end{pmatrix}. \tag{39}$$

does not satisfy the A-sublattice boundary condition for arbitrary C_7, C_8, p, and θ as long as p is sufficiently small.

We failed to construct zero-energy wave functions in the 120° case in the form of a linear combination of the edge states, in striking contrast to the 60° case. It is considered that this corresponds to the disappearance of the LDOS peak at $\varepsilon = 0$ near the corner observed in the numerical result. We suppose that correct zero-energy states consist of zz edge states and complex scattered waves. We point out that the sublattice configuration of two zz edges plays a crucial role in the qualitative difference between the 60 and 120° cases.

In the remaining of this section we briefly consider the behavior of the LDOS shown in Fig. 8, on the basis of the wave functions obtained above. Figure 8 shows the spatial dependence of the LDOS at $\varepsilon = 0$ in the 60, 90, and 150° cases. We observe that the LDOS on a zz edge is slightly suppressed in the close vicinity of a corner. This should be distinguished from the strong suppression of the LDOS observed near a 120° corner, and is simply accounted for on the basis of the wave functions for zero-energy edge localized states presented in eqs. (24), (29), and (33). We see

that due to destructive interference, the amplitude of these wave functions is suppressed in the close vicinity of a corner located at $(x, y) = (0, 0)$ for a sufficiently small k_x. This accounts for the slight suppression of the LDOS.

5. Summary

We have studied electronic states in semi-infinite graphene with a corner edge, focusing on the stability of edge localized states. The 60, 90, 120, and 150° corner edges are examined. The 90 and 150° corner edges consist of one zz edge and one ac edge, while the 60 and 120° corner edges consist of two zz edges. We have numerically obtained the local density of states on the basis of a nearest-neighbor tight-binding model by using Haydock's recursion method. We have shown that edge localized states appear along a zz edge of each corner edge structure except for the 120° case. In the 120° case, we have also shown that edge localized states locally disappear near the corner but emerge with increasing the distance from the corner along each zz edge. To provide insight into these behaviors, we have analyzed electronic states at $\varepsilon = 0$ within the framework of an effective mass equation. Except for the 120° case, we have succeeded to obtain eigenstates of the effective mass equation by forming a superposition of pair of edge localized wave functions for an infinitely long straight zz edge. This indicates the existence of edge localized states, and is consistent with the behavior of the local density of states. Contrastingly, no eigenstate has been obtained in such a simple form in the 120° case. This suggests a possibility that the local disappearance of edge localized states in the 120° case is beyond the effective mass description. Note that although both the 60 and 120° corner edges consist of two zz edges, zero-energy eigenstates of the effective mass equation are obtained only in the former case. We have pointed out that this reflects the fact that two zz edges belong to a same sublattice in the former case while they belong to different sublattices in the latter case.

1) K. S. Novoselov, A. K. Geim, S. V. Morozov, D. Jiang, Y. Zhang, S. V. Dubons, I. V. Grigoriva, and A. A. Firsov: Science **306** (2004) 666.
2) K. S. Novoselov, A. K. Geim, S. V. Morozov, D. Jiang, M. I. Katsnelson, I. V. Grigorieva, S. V. Dubonos, and A. A. Firsov: Nature **438** (2005) 197.
3) See, for a review, A. H. Castro Neto, F. Guinea, N. M. R. Peres, K. S. Novoselov, and A. K. Geim: Rev. Mod. Phys. **81** (2009) 109.
4) J. W. McClure: Phys. Rev. **104** (1956) 666.
5) P. R. Wallace: Phys. Rev. **71** (1947) 622.
6) Y. Zhang, Y.-W. Tan, H. L. Stormer, and P. Kim: Nature **438** (2005) 201.
7) T. Ando, T. Nakanishi, and R. Saito: J. Phys. Soc. Jpn. **67** (1998) 2857.
8) M. I. Katsnelson, K. S. Novoselov, and A. K. Geim: Nat. Phys. **2** (2006) 620.
9) M. Fujita, K. Wakabayashi, K. Nakada, and K. Kusakabe: J. Phys. Soc. Jpn. **65** (1996) 1920.
10) Y. Kobayashi, K. Fukui, T. Enoki, K. Kusakabe, and Y. Kaburagi: Phys. Rev. B **71** (2005) 193406.
11) Y. Niimi, T. Matsui, H. Kambara, K. Tagami, M. Tsukada, and H. Fukuyama: Phys. Rev. B **73** (2006) 085421.
12) R. Haydock: in *Solid State Physics*, ed. H. Ehrenreich, F. Seitz, and D. Turnbull (Academic, New York, 1980) Vol. 35, p. 216.
13) M. J. Kelly: in *Solid State Physics*, ed. H. Ehrenreich, F. Seitz, and D. Turnbull (Academic, New York, 1980) Vol. 35, p. 296.
14) L. C. Davis: Phys. Rev. B **28** (1983) 6961.
15) S. Wu, L. Jing, Q. Li, Q. W. Shi, J. Chen, H. Su, X. Wang, and J. Yang: Phys. Rev. B **77** (2008) 195411.
16) J. C. Slonczewski and P. R. Weiss: Phys. Rev. **109** (1958) 272.
17) K. Wakabayashi: Ph. D. Thesis, University of Tsukuba (2000).
18) M. Ezawa: Phys. Rev. B **81** (2010) 201402(R).
19) C. Iniotakis, S. Graser, T. Dahm, and N. Schopohl: Phys. Rev. B **71** (2005) 214508.

World Scientific
www.worldscientific.com

ELECTRONIC STATES AND LOCAL DENSITY OF STATES NEAR GRAPHENE CORNER EDGE

YUJI SHIMOMURA

Department of Quantum Matter, AdSM, Hiroshima University,
Higashi-Hiroshima, Hiroshima, 739-8530, Japan
shimomura25@hiroshima-u.ac.jp

YOSITAKE TAKANE

Department of Quantum Matter, AdSM, Hiroshima University,
Higashi-Hiroshima, Hiroshima, 739-8530, Japan

KATSUNORI WAKABAYASHI

International Center for Materials Nanoarchitectonics (WPI-MANA),
National Institute for Materials Science (NIMS),
Namiki 1-1, Tsukuba 305-0044, Japan

We study that stability of edge localized states in semi-infinite graphene with a corner edge of the angles 60°, 90°, 120° and 150°. We adopt a nearest-neighbor tight-binding model to calculate the local density of states (LDOS) near each corner edge using Haydock's recursion method. The results of the LDOS indicate that the edge localized states stably exist near the 60°, 90°, and 150° corner, but locally disappear near the 120° corner. By constructing wave functions for a graphene ribbon with three 120° corners, we show that the local disappearance of the LDOS is caused by destructive interference of edge states and evanescent waves.

Keywords: Graphene corner edge; zigzag; edge localized.

PACS numbers: 81.05.ue, 73.22.Pr, 73.20.-r

1. Introduction

Graphene is the first true two-dimensional material composed of carbon atoms.[1] Since it contains non-equivalent two carbon atoms in the unit cell due to the nature of honeycomb lattice, the low-energy electronic properties of graphene are well described by the massless Dirac equation, where the valence and conduction bands conically touch at the Fermi energy.

The presence of edges in graphene makes strong implications for electronic states near the Fermi energy. There are two representative edges structures in graphene, called zigzag (zz) and armchair (ac). Zigzag edge provides highly degenerated edge

localized state (edge state) at the Fermi energy,[2] but armchair edge does not show such localized state. Recently the atomic structures of graphene edges were studied using scanning tunneling microscope and successively the presence of edge states is confirmed using scanning tunneling spectroscopy.[3,4] Although in these experiments the relatively long armchair edges are observed, zigzag edges preferably appear to form corner edges.[3]

In our previous publication,[5] we have shown that electronic states of graphene with a corner edge crucially depend on the corner angle. Corners with the angles $60°$, $90°$ and $150°$ can stably possess the edge states, where the wave functions can be analytically obtained as a simple linear combination of edge states.[5,6] In the $120°$ case, however, the edge states locally disappear, and an appropriate wave function cannot be obtained in a similar manner. In this paper, we will numerically demonstrate that the wave functions of $120°$ corner edge can be described as the destructive interference between the edge states and evanescent waves.

2. LDOS on Corner Edges

We assume that π electronic states in graphene are described by a tight-binding model on a honeycomb lattice. The Hamiltonian is $H = -t \sum_{\langle i,j \rangle} |i\rangle\langle j|$, where $\langle i,j \rangle$ is a pair of the nearest-neighbor sites, and t is a hopping integral. For a given energy E, we calculate the LDOS at an arbitrary site using Haydock's recursion method.[5,7–10] Throughout this paper, the origin of energy is set to the Fermi energy of graphene. To calculate the LDOS at the ith size, we transform our tight-binding model to a one-dimensional chain model with a tridiagonal Hamiltonian[a]:

$$\mathcal{H} = \begin{pmatrix} a_0 & b_1 & & \\ b_1 & a_1 & b_2 & \\ & b_2 & a_2 & \\ & & & \ddots \end{pmatrix}. \tag{1}$$

The Green's function $G_i(E)$ for the ith site is approximately expressed as

$$G_i(E) = \cfrac{1}{E - a_0 - \cfrac{b_1^2}{E - a_1 - \cfrac{b_2^2}{E - a_N - t(E)}}}, \tag{2}$$

where

$$t(E) = \frac{E - a_N}{2b_N^2} \left[1 - \left\{ 1 - \frac{4b_N^2}{(E - a_N)^2} \right\}^{\frac{1}{2}} \right]. \tag{3}$$

Eq. (2) exactly takes account of the effects of all carbon sites up to the Nth neighbor sites from ith site. The effects of other carbon sites beyond this distance are

---

[a]The normalized bases of $\mathcal{H}$ are determined in terms of the recursion relation $b_{n+1}|n+1\rangle = (H - a_n)|n\rangle - b_n|n-1\rangle$ with $a_n = \langle n|H|n\rangle$ and the initial state $|0\rangle \equiv |i\rangle$. See, Ref. 5 for details.
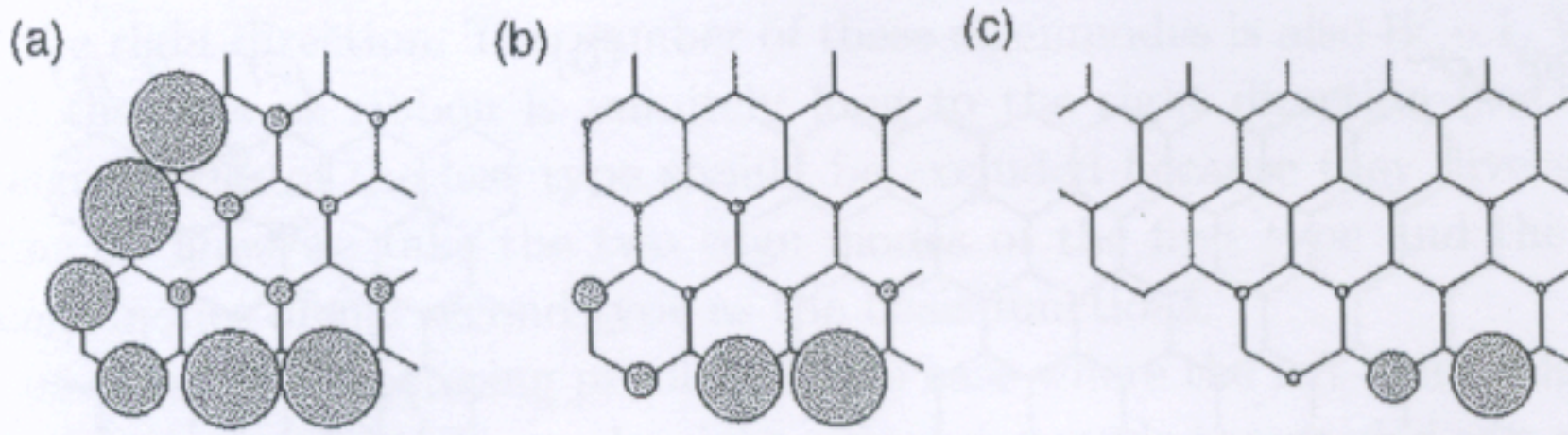
Fig. 1.   The LDOS at $E = 0$ of semi-infinite graphene with a corner edge with angles of (a) 60°, (b) 90°, and (c) 150°. The radius of circles denotes the magnitudes of LDOS.
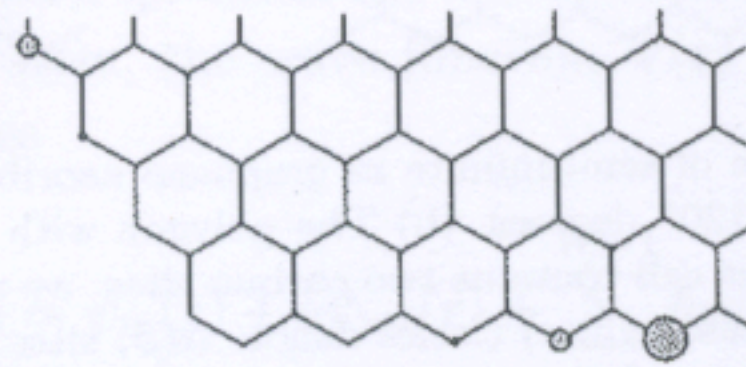

Fig. 2.   The LDOS at $E = 0$ for semi-infinite graphene with a corner edge of the 120°.

approximately taken into account through $t(E)$. $G_i(E)$ gives the LDOS at the ith site in terms of the relation

$$n_i(E) = \frac{1}{\pi} \mathrm{Im} G_i(E - i\delta), \tag{4}$$

where δ is a positive infinitesimal. We calculate the LDOS in the case of 60°, 90°, 120° and 150° corner edges by setting $N = 1000$.

Figure 1 shows the LDOS for the corner edges with 60°, 90° and 150°, while Fig. 2 shows the LDOS for the corner edge with 120°. Here the energy is fixed at the Fermi energy of graphene, i.e. $E = 0$. In the cases of 60°, 90° and 150°, we observe the characteristic feature of the edge states that the LDOS have the finite amplitudes only on one of two sub-lattices. In contrast, in the case of 120°, the LDOS at zero energy almost disappears near the corner edge, but its value on the zz edge increases with being distant from the corner.

3. Wave Functions for 120° Corner

It is interesting to consider wave functions that can account for the behavior of the LDOS observed in the previous section. In the 60°, 90° and 150° cases, such wave functions can be analytically obtained as a simple linear combination of edge states.[5,6] In the 120° case, however, an appropriate wave function cannot be obtained in a similar manner. This implies that not only the edge modes but also locally induced evanescent waves play a role.

To numerically construct wave functions for 120° corner, we propose to treat a semi-infinite zz ribbon having three 120° corner edges as shown in Fig. 3(a). Since we are interested in the local disappearance of edge states near 120° corner, our
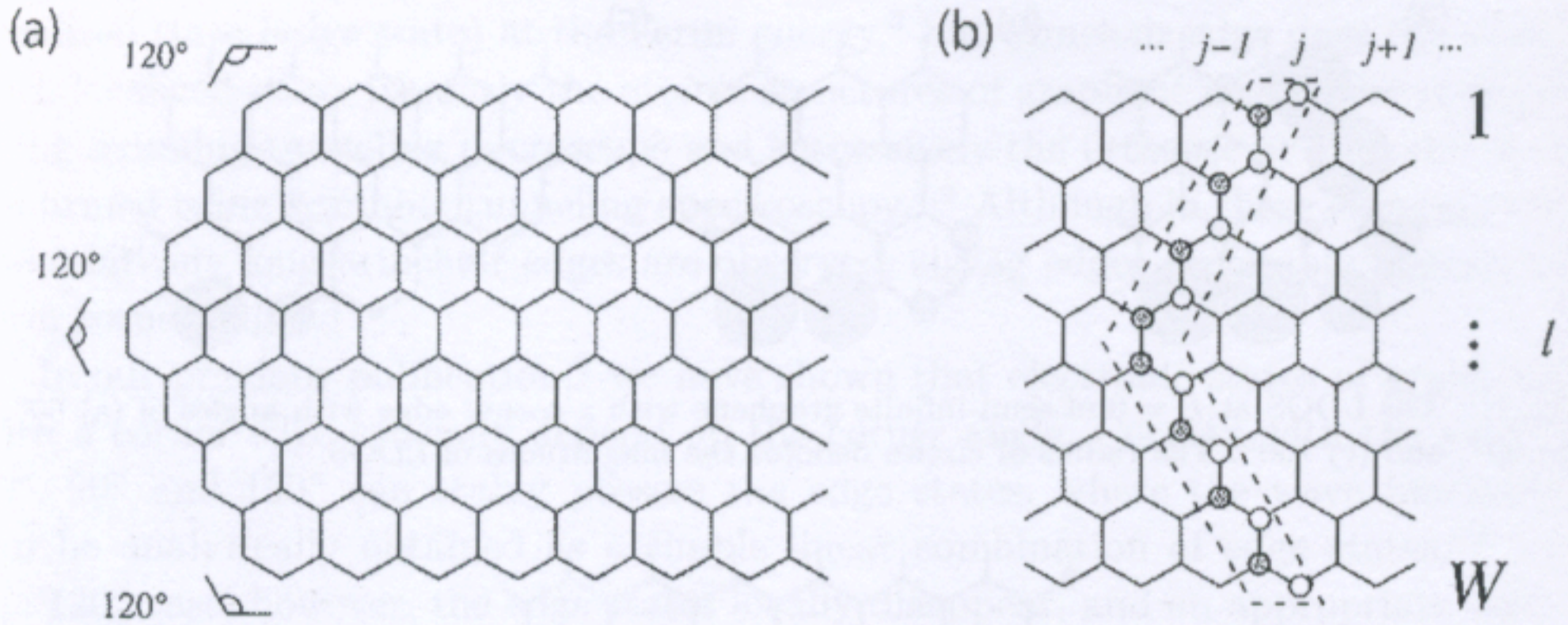
(a)

(b)

Fig. 3.　(a) Schematic structure of semi-infinite zz graphene naoribbon, where left-side is terminated by three corner edges of 120° degrees. (b) The polygon with dashed lines defines the unit cell. Since each zz line in the unit cell contains two carbon sites, we refer to the left (right) site on the lth zz line as $l\alpha(l\beta)$. The black (white) circles denote $\alpha(\beta)$ sites.

attention is focused on low-energy states with $E \cong 0$. We take the unit cell of the zz ribbon as shown in Fig. 3(b). Each unit cell has $2W$ sites, where W is the number of zz lines. The jth unit cell contains two sites of each zz line. We refer to the left (right) site on the lth zz line as $l\alpha(l\beta)$. We define $\mathbf{C}_j^\alpha(\mathbf{C}_j^\beta)$ as the column vector consisting of the wave coefficients at $l\alpha(l\beta)(l = 1, 2, \ldots, W)$. The column vectors $\mathbf{C}_j^\alpha$ and $\mathbf{C}_j^\beta$ satisfy the relations

$$\mathbf{H}_1\mathbf{C}_j^\alpha + \mathbf{H}_2\mathbf{C}_j^\beta + \mathbf{H}_2\mathbf{C}_{j-1}^\beta = E\mathbf{C}_j^\alpha, \tag{5}$$

$$\mathbf{H}_2^\dagger\mathbf{C}_j^\alpha + \mathbf{H}_3\mathbf{C}_{j+1}^\alpha = E\mathbf{C}_j^\beta, \tag{6}$$

where $\mathbf{H}_1$ ($\mathbf{H}_2$) represents the intra-cell transfer between nearest neighbor α (α and β) sites in jth unit cell, and $\mathbf{H}_3$ represents the inter-cell transfer between nearest neighbor α and β sites, respectively. Eliminating terms with the column vectors for β sites from (5) and (6), we obtain

$$\mathbf{C}_{j+1}^\alpha + \mathbf{u}\mathbf{C}_{j-1}^\alpha + \mathbf{v}\mathbf{C}_j^\alpha = 0, \tag{7}$$

where $\mathbf{u}$ and $\mathbf{v}$ are matrices which are constructed in terms of $\mathbf{H}_1$, $\mathbf{H}_2$, $\mathbf{H}_3$ and E. Here, we assume that the column vector satisfies $\mathbf{C}_{j+1}^\alpha = \lambda\mathbf{C}_j^\alpha$. From (7), the eigenvalue equation

$$\begin{pmatrix} -\mathbf{v} & -\mathbf{u} \\ 1 & 0 \end{pmatrix}\begin{pmatrix} \mathbf{C}_j^\alpha \\ \mathbf{C}_{j-1}^\alpha \end{pmatrix} = \lambda\begin{pmatrix} \mathbf{C}_j^\alpha \\ \mathbf{C}_{j-1}^\alpha \end{pmatrix} \tag{8}$$

is derived. Solving (8), we obtain $2W$ eigenmodes. They can be classified into three types according to the absolute value of an eigenvalue λ. The first type is the eigenmodes with $|\lambda| = 1$. At $E \cong 0$, we obtain two such eigenmodes representing edge states. One is the right-going mode, and the other is the left-going mode. The second type is the evanescent modes with $|\lambda| < 1$, and the number of these modes is $W - 1$. The last type is the modes with $|\lambda| > 1$ which exponentially increase

toward the right direction. The number of these eigenmodes is also $W - 1$. We have assumed that the zz ribbon is infinitely long to the right direction (see Fig. 3), so the eigenmodes of the last type should be excluded because they diverges with increasing j. Thus we take the two edge modes of the first type and the $W - 1$ evanescent modes of the second type as the basis functions.

Let us consider a scattering problem in the case where the left-going edge mode is incident from the right. Then, the right-going edge mode is regarded as a reflected wave, and $W - 1$ evanescent modes play a role of scattered waves. Let us express the two edge modes as $\psi_{in}(\mathbf{r})$ and $\psi_{ref}(\mathbf{r})$, and the $W - 1$ evanescent modes as $\psi_1(\mathbf{r}), \ldots, \psi_{W-1}(\mathbf{r})$, where $\mathbf{r}$ represents the site specified by j, l and η with $\eta = \alpha$ or β. In the zz ribbon system, the wave function $\Psi(\mathbf{r})$ is represented as a linear combination of these waves

$$\Psi(\mathbf{r}) = \psi_{in}(\mathbf{r}) + a\psi_{ref}(\mathbf{r}) + \sum_{k=1}^{W-1} b_k \psi_k(\mathbf{r}), \tag{9}$$

where a and $\{b_k\}$ are unknown coefficients to be determined. We consider the boundary condition at the left boundary consisting of three $120°$ corner edges. Note that this boundary can be created from an infinitely long zz ribbon by removing W sites, each of which is the nearest neighbor of a boundary site. We require that the wave function vanishes at these removed sites, i.e., $\Psi(\mathbf{r}_1) = \Psi(\mathbf{r}_2) = \cdots = \Psi(\mathbf{r}_W) = 0$, where $\mathbf{r}_1, \ldots, \mathbf{r}_W$ are positions of the removed sites. Imposing this boundary condition to (9), we numerically determine the unknown coefficients. Actual calculation is performed for the case of $W = 30$.
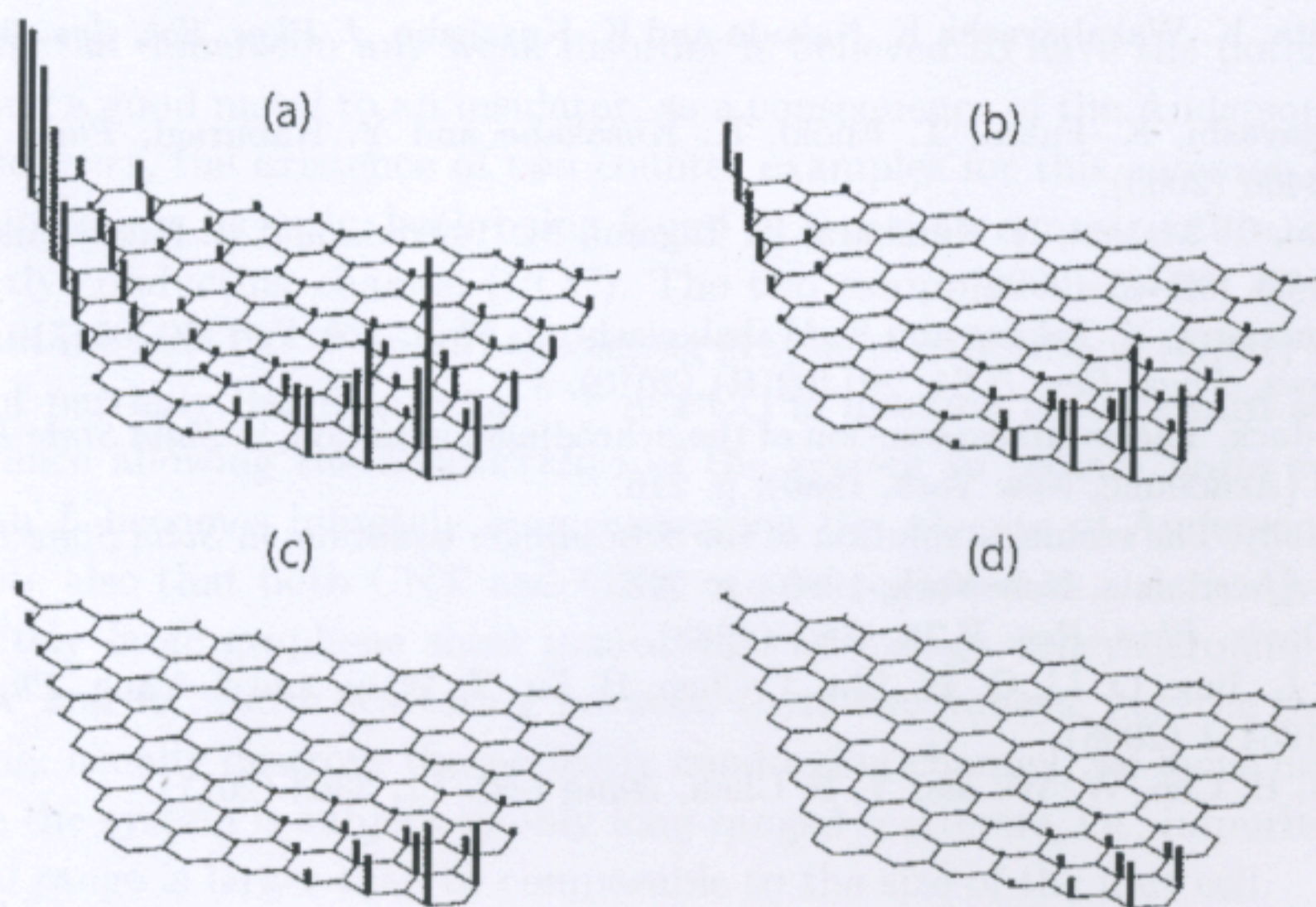

Fig. 4. The absolute value of the wave function $\Psi(\mathbf{r})$ at $E/l =$ (a) 10^{-3}, (b) 10^{-4}, (c) 10^{-5}, and (d) 10^{-6} near one of the $120°$ corner edges. The length of bars indicates $|\Psi(\mathbf{r})|$.

In Fig. 4, we show the absolute value of the wave function $|\Psi(\mathbf{r})|$ at $E/t =$ (a) 10^{-3}, (b) 10^{-4}, (c) 10^{-5} and (d) 10^{-6} near the 120° corner edge. The figures show an extracted area from the entire zz ribbon. We observe that $|\psi(\mathbf{r})|$ almost disappears near the corner, but its amplitude on the zz edge increases with being distant from the corner edge. These features are consistent with the behavior of LDOS.

4. Summary

We have studied electronic states of semi-infinite graphene with a corner edge, focusing on the stability of edge localized states. We have calculated the local density of states (LDOS) of each case based on the nearest-neighbor tight-binding model using Haydock's recursion method. The edge localized states stably exist near the 60°, 90° and 150° corners, but locally disappear near the 120° corner. By constructing wave functions for a graphene ribbon with three 120° corners, we found that the local disappearance of the LDOS is caused by destructive interference of edge states and evanescent waves. Recent experiments has reported that zigzag edges with many ~120° turns had been observed on the graphene grains synthesized on Cu foils by chemical vapor deposition.[11] The local disappearance of edge localized states for 120° corner edge might be related to the above experiment, because the local disappearance of edge localized states energetically stabilizes the formation of corner edges with such angle. Further theoretical details will be published elsewhere.

References

1. A. K. Geim and K. S. Novoselov, *Nature Mat.* **6**, 183 (2007).
2. M. Fujita, K. Wakabayashi, K. Nakada and K. Kusakabe, *J. Phys. Soc. Jpn.* **65**, 1920 (1996).
3. Y. Kobayashi, K. Fukui, T. Enoki, K. Kusakabe and Y. Kaburagi, *Phys. Rev. B* **71**, 193406 (2005).
4. Y. Niimi, T. Matsui, H. Kambara, K. Tagami, M. Tsukada and H. Fukuyama, *Phys. Rev. B* **73**, 085421 (2006).
5. Y. Shimomura, Y. Takane and K. Wakabayashi, *J. Phys. Soc. Jpn.* **80**, 054710 (2011).
6. M. Ezawa, *Phys. Rev. B* **81**, 201402(R) (2010).
7. R. Haydock, The recursive solution of the Schrödinger equation, in *Solid State Physics*, Vol. 35 (Academic, New York, 1980), p. 216.
8. M. J. Kelly, The recursive solution of the Schrödinger equation, in *Solid State Physics*, Vol. 35 (Academic, New York, 1980), p. 296.
9. L. C. Davis, *Phys. Rev. B* **28**, 6961 (1983).
10. S. Wu, L. Jing, Q. Li, Q. W. Shi, J. Chen, H. Su, X. Wang and J. Yang, *Phys. Rev. B* **77**, 195411 (2008).
11. J. Tian, H. Cao, W. Wu and Y. P. Chen, *Nano Lett.* **11**, 3363 (2011).